Utrecht University

MSc Thesis

Quantitative Analysis of Shear Zone Structures at Cap de Creus (NE Spain) – Insights from High Resolution, Remote Sensing Mapping Techniques

Author:
M. Sibbel

Supervisors:
Dr. Ernst Willingshofer
Prof. Dr. Martyn Drury

A thesis submitted in fulfillment of the requirements for the degree of Master of Science

In the

Structural Geology
Department of Earth Sciences

October 1th, 2023

Utrecht University

Abstract

Faculty of Geosciences
Department of Earth Sciences

Master of Science

Quantitative Analysis of Shear Zone Structures at Cap de Creus (NE Spain) Based on High Resolution, Remote Sensing Mapping Techniques

by M. Sibbel

Recent advances in Unmanned Aerial Systems (UAS) and Computer based Structure From Motion (SFM) enable the digitization, reconstruction, archiving, and quantitative analysis of Geologic outcrops in a digital environment. Reconstructed models represent a snapshot in time of an outcrop. Digital Orthophotos, 3D models, Surface Maps, 2D Vector files, and 3D Polygon maps are created by the geometrical alignment and reconstruction of thousands of high-resolution aerial and ground photographs. In this research, a Photogrammetry-based workflow is evaluated in multiple case studies on Shear Zones, Pegmatites, Aplite Dykes, and Diorite Enclaves within the Cap de Creus Peninsula in NE, Spain. The scope of this research is to assess the potential of these techniques to further our understanding of the deformation history of the study area and, in the process, develop valuable strategies and workflows to extract quantitative strain measurements. While the structural deformation history of the Cap de Creus area has been studied in detail, deformation on a mesoscale until today has not been possible due to technological constraints. Deformation markers and finite strain are extracted from the reconstructed models (XYZ) and orthophotos (XY) by applying specialized software that compiles the obtained data into a readable format, rose diagrams, stereonets, heat maps, and polar plots. These calculated datasets are calibrated and compared to field measurements to constrain the deformation conditions. Quantitative datasets are combined with high-resolution UAS surface maps to reconstruct and model the progressive deformation phases present at Cap de Creus. The resulting 2D maps and 3D numerical models represent a Geologist's best interpretation of the subsurface evolution of the late Variscan mountain-building phase in NE Iberia.

This thesis demonstrates how UAS-SFM workflows can deliver high-quality results that compare and, more importantly, enhance traditional methods, enabling (i) the acquisition of larger datasets faster and more efficiently over a much larger area, (ii) Post-fieldwork quality control on field measurements, (iii) remove random human and equipment error, (iv) save valuable time during fieldwork by enabling base maps acquired in the field to be enhanced with digital measurements, enabling the Geologist to work more efficiently. The different case studies explored in Cap de Creus exemplify how powerful reconstructed field outcrops scaled to accurate world dimensions are and how they enable enhanced data acquisition in a digital environment and the ability to make and test new observations indefinitely. Digital maps of the Late Variscan Roses Granodiorite are compiled into 2D and 3D models with a Ground Sampling Distance (GSD) of 3.31mm/pix, enabling the acquisition of 1017 diorite enclaves and hundreds of intruded aplite dykes in just a few hours for quantitative strain analysis. This thesis also demonstrates the importance of using a concise and targeted approach to UAS-based mapping. Albeit mapping vast areas is possible, the resources required for reconstruction, the amount of data generated, and the negative impact on resolution constrain its usefulness in Geologic quantitative analysis. It is preferable instead to focus UAS mapping on a specific outcrop where visual markers are easily identifiable and can be used to quantify deformation. Quantitative analysis of the Late Variscan Roses Granodiorite provides new strain estimates for the mafic enclave deformation using the Rf - Φ method, 40% shortening under a close to three-dimensional homogeneous flattening and 50% shear strain of the retrograde greenschists shear zones which are in accordance with traditional and manual techniques for measuring strain. The ability to digitally measure a large population of stain markers furthers the precision and constraints on deformation.

Abbreviations & Symbols

LP-HT	Low pressure-high temperature
L_m	Mylonitic stretching lineation
S_1, S_2	Foliations related to D_1 and D_2
P-T	Pressure temperature
S_m	Mylonitic foliation
S_S	Bedding surface
S_r	Metasedimentary penetrative foliation
D_1, D_2	Sequential deformation events
X, Y, Z axes	Principal axes of strain

Minerals

PL	Plagioclase
Qtz	Quartz
Ms	Muscovite

biotite-hornblende granodiorite consists of quartz oligoclase-andesine, K-feldspar, biotite and hornblende.

Remote Sensing Terminology

GCP	Ground Control Point
NADIR	Direction pointing directly below a location
RTK	Real-Time Kinematic Positioning
GNSS	Global Navigation Satellite System (GPS, Galileo, Beidou)

Acknowledgments

This report was written as part of my MSc thesis, conducted at Utrecht University (Earth simulations Lab, ESL). The research was supervised by Dr. Ernst Willingshofer & Prof. Martyn Drury. I want to express my gratitude to them both for their invaluable input, guidance, and mentorship during fieldwork and the compilation of this manuscript. I also thank Dr. Richard Wessels and Dr. Oliver Plümper for sharing their surface mapping and GIS knowledge and ideas. Lastly, my most profound gratitude goes out to all my fellow students and Geoscience staff whom I had the pleasure of knowing and learning from during my journey at the University.

Table of Contents

List of Figures

List of Tables

1. Introduction

Geologic Fieldwork to interpret, constrain, and quantify deformation is a key element in understanding large-scale geologic processes. Without the insight from strain markers, their shape changes and orientation it is impossible to accurately backtrack and gain insight into Earth's Geodynamic history (Gleizes, Gerard et al., 1998; Karabinos and Warren, 2010; Fonseca et al., 2015; Gardner et al., 2015). In that context, the ability to obtain quantitative strain measurements in combination with qualitative observations has been instrumental in geology, for example, in determining the tectonic evolution of continental collision and extension settings.

The Cap de Creus peninsula (NE Spain), located at the easternmost end of the Pyrenean Axial Zone (Zwart, 1986), is a remarkable geologic site due to its well-exposed outcrops that reveal a myriad of complex tectonic (Carreras, J. and Druguet, 1994; Carreras, Jordi et al., 2004; Vissers, Reinoud LM et al., 2017), metamorphic (Reche et al., 1998; Ibarguchi, 1999; Fernández-Suárez et al., 2007), and magmatic structures (Carreras, Jordi and Losantos, 1982; Simpson, C. and Sistach, 1982; Fonseca et al., 2015) mostly related to the Variscan Orogeny (Celma, 1982; Corbella and Melgarejo, 1993; Carreras, J. and Druguet, 1994; Druguet, E., 2001; Vissers, Reinoud LM et al., 2020). Cap de Creus is considered an important proxy's into Earth's evolution during the Variscan Orogeny in Europe and the formation of the supercontinent Pangea as a result of continental collision. The structures visible in Cap de Creus define the deep-seated late Variscan deformation of NE Iberia, where metamorphic, magmatic, and structural domains are present on a relatively small scale. Traditional In-field quantitative measurements, sampling, and qualitative observations are done manually either on the surface by rock samples or measurements or slightly above it by visual observations at eye level. These analogue measurements are precise on the scale that they are measured and normally require a multitude of measurements at different locations to be able to arrive at a regional quantitative interpretation of the history of the area. Although these techniques are the backbone of Geology, they can be very time-consuming and may require frequent fieldwork trips until the desired results are obtained.

Recent advances in Unmanned Aerial Systems (UAS), Computer based Structure from Motion (SFM), and LiDAR techniques enable the digitization, reconstruction, and archival of Geologic outcrops in the form of 3D point clouds and geometric meshes (Koenderink and Van Doorn, 1991; Vitek et al., 1996; Eisenbeiß, 2009; Javernick et al., 2014; Agüera-Vega et al., 2018). Georeferencing digital surface models enables the extraction of accurate quantitative measurements of Geologic outcrops in a Digital Environment (Helmke et al., 2007; Vollgger and Cruden, 2016; Jordan, 2015; Mayer et al., 2018). Moreover, digital models of outcrops can be combined with analog quantitative measurements to constrain the deformation mechanism.

In this study, remote sensing Unmanned Aerial System mapping techniques will be used and evaluated in the form of a case study on the Cap de Creus peninsula. Workflows, extraction techniques, and quantitative measurements will be compiled and compared to data obtained from analytical in-field measurements for reference and calibration.

The case study presented in this master thesis manuscript aims to answer the following questions: (i) what are the structural and metamorphic characteristics of co-genetic shear zones, and can this information be used to firstly map different generations of shear zones and secondly, establish their relation to igneous activity in the region, (ii) can strain and shear zone displacement be measured quantitatively together with shear zone geometries to infer the deformation regime, (iii) is it possible to reconstruct the geometry of the shear zones through the interpretation of digital models, and what are the related uncertainties.

2. Geological Setting of the Alpine Orogeny

In North – Eastern Iberia, Alpine tectonics gave rise to the Pyrenees due to the collision between Iberia and the European plate (Roure et al., 1989; Choukroune et al., 1990; Muñoz, 1992). The Pyrenees is a chain of Paleogene age that is part of a larger structure that extends westward from the Alps to the northwestern corner of the Iberia peninsula. The collision between Iberia and Europe involved crustal shortening of the Mesozoic and Tertiary sedimentary cover of the Variscan basement (Planells and Druguet, 2013). The Pyrenean structures consist of large fold and thrust belts developed under low-grade metamorphic conditions without penetrative cleavages (Muñoz et al., 1986). Although most deformation occurred in the brittle regime, abundant veining related to the brittle-to-ductile transition is present. The orogeny is marked by large-scale heterogeneous non-coaxial shortening with an N – S shortening direction. Compiling a cross-section from N – S (ECORS), (Vergés et al., 2002; Casas et al., 2019), the following WNW – ESE trending structures can be distinguished;

1. *Foreland Aquitania basin (Esteban et al., 2011)*.
2. *North Pyrenean zone (NPZ)*. This structure is thrust north towards the foreland Aquitania basin. The NPZ, bound by the 'North Pyrenean Fault (NPF),' is a sinistral strike-slip fault developed during the Cretaceous associated with the clockwise rotation of Iberia towards Europe (Ribeiro et al., 2019).
3. *Axial Zone*. The Axial Zone comprises Variscan orogenic Precambrian and Paleozoic basement rocks that make up the Pyrenean chain's highest elevations. The axial zone belongs to the south-facing domain (Vergés et al., 2002).
4. *Southern Pyrenean zone*. This structure is the symmetrical equivalent of the NPZ, comprising of south vergent fold and thrust belts involving cover and basement rocks.
5. *Foreland Ebro basin*.

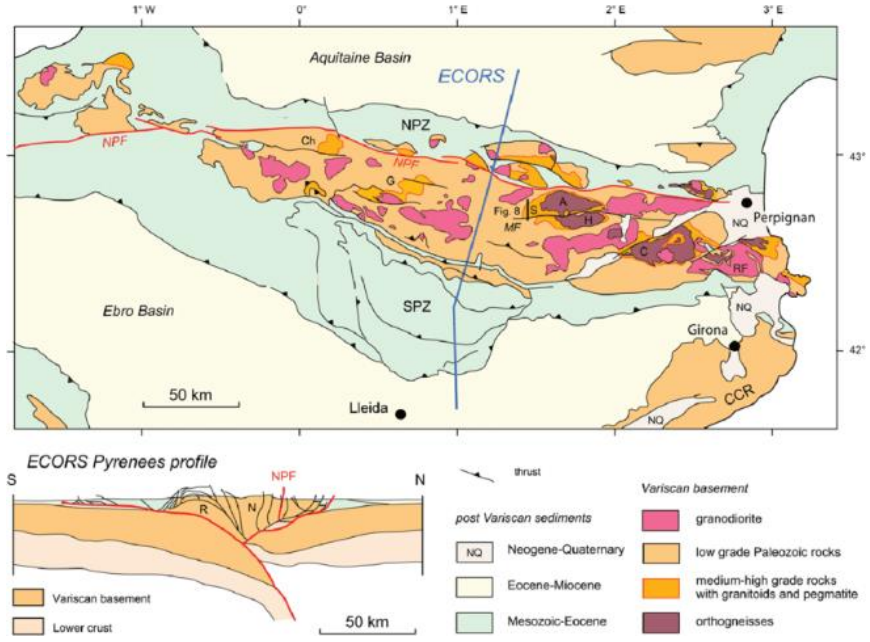

Figure 2.1 Structural sketch showing the Pyrenean orogenic belt and its structural units. The Axial Zone and North Pyrenean zones are bordered South and North by two Neogene basins. Modified after (Vissers, Reinoud LM et al., 2017).

The Pyrenees display an asymmetric fan-like geometry bound by the northern and the more well-developed southern antithetic fault zones. There is a broad acceptance that the magmatic and metamorphic signature of the basement rock pertains to the Variscan orogeny. Therefore, understanding Alpine tectonics is paramount for reconstructing and interpreting the earlier Variscan orogeny. The effect of the Alpine orogeny on the Variscan basement has shown to be primarily (Carreras, Jordi and Druguet, 2014): (i) Horizontal translation and rotation of Iberia relative to the stable Western European plate during the ***Neogene*** rifting event; (ii) collision of Iberia with the Eurasian plate during the ***Paleogene*** accompanied by tilting and thrusting of Paleozoic units; (iii) rotation of Iberia relatively to the stable Eurasian plate and the development of brittle sinistral fault zones affecting the cover and Variscan basement during the ***Cretaceous***. *Neogene extension tectonics* related to post-kinematic collapse is responsible for the development foreland extension basins, The Aquitanian basin in the North, Ebro Basin in the south, the Cerdanya graben in the Eastern Pyrenees and the Vallès-Penedès graben in the Catalan Coastal Ranges forming predominantly NE-SW trending normal and strike-slip faults (Vergés et al., 2002). These grabens are predominately filled with mid-ocean carbonates & volcaniclastic sediments. Neogene extension is predominately responsible for rigid body kinematics of the Variscan basement without significant internal deformation.

Moreover, Neogene extensional tectonics is the primary drive responsible for the segmentation of Variscan domains in the foreland while Paleogene shortening related to fold-and-thrust belts is responsible for the segmentation of Variscan domains in the central and eastern Pyrenees. Paleozoic rocks are involved in three Alpine basement thrust sheets, referred to as the Lower Structural units, which induced significant southward translation of Paleozoic rocks relative to their autochthon basement (Vergés et al., 2002; Munoz et al., 1992). Southward translation of the lower structural units places their original position northward from the present-day arrangement. Alpine deformation gave rise to important rotation related to antiformal stack development. In contrast, widespread metamorphism during the Alpine orogeny is absent, with only moderate internal deformation (Quesada and Oliveira, 2019). Anticlockwise rotation of Paleozoic rocks during the Cretaceous induced eastward drift and the formation of the Bay of Biscay with deformation localization along the NPF, causing the separation of Galicia from Britany. The proposed reconstruction displacement and rotation vary for different workers between 100 – 400 Km along the NPF and 20 – 40°. However, most models emphasize rotation over translation with considerable lateral crustal shortening as a mechanism to close the oceanic basin (Vissers, RLM and Meijer, 2012; Carreras, Jordi and Druguet, 2014).

3. Geologic Setting of Cap de Creus

The Cap de Creus peninsula (NE Spain), Figure 3.1 (b), located at the easternmost end of the Pyrenean Axial Zone, is a remarkable center of geology due to its well-exposed outcrops that reveal a myriad of complex tectonic, metamorphic, and magmatic structures affecting the Paleozoic basement of the Pyrenees, cutting across medium-to-high-grade schists. Cap de Creus is characterized by two WNW-ESE trending late Variscan shear belts (northern and southern) associated with significant strike-slip movement. The northern shear belt with *north-dipping* attitudes is associated with high grade metamorphic rocks and pegmatite complexes crosscut by large anastomosing shear zones (Figure 3.2). In the south, the Roses shear belt is characterized by SW – NE trending shear zones with south-dipping attitudes. Both northern and southern shear bands display similar strike-slip displacements. Kinematics has been identified through asymmetric c-axes of quartz veins (Carreras et al.,1997). A low-grade metasedimentary fold belt with minor quartz dike intrusions characterizes the central region bordering shear belts. At Cap de Creus, there is a gradual change in the tectonic style from highly crystalline rocks in the northern belt of the peninsula towards less crystalline schists in the central part (Carreras, J., 2001). The sections below describe the north and southern shear belts of Cap de Creus in more detail.

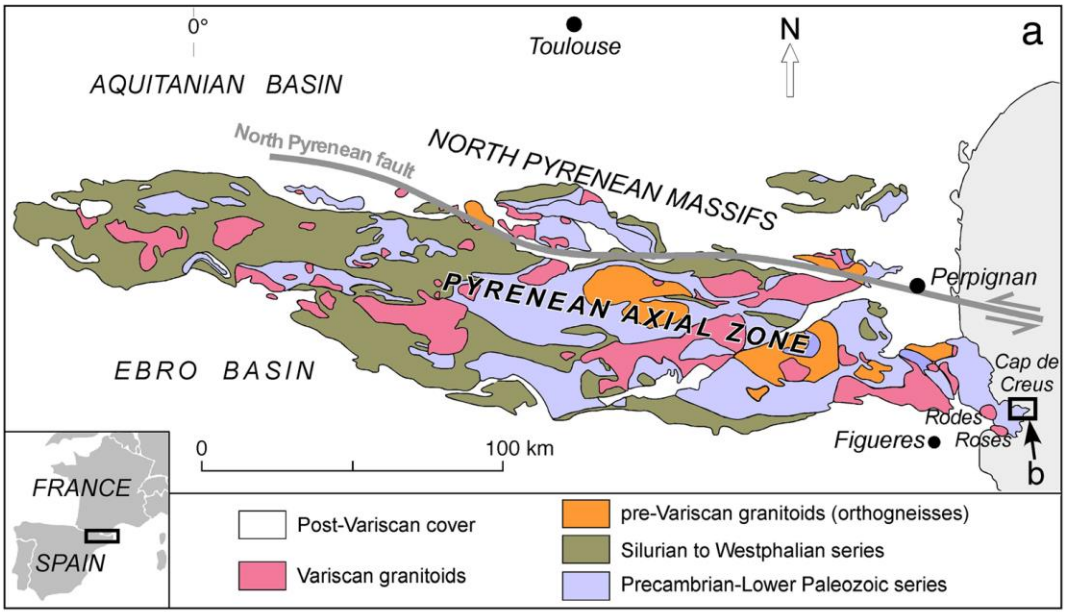

Figure 3.1 Geological map of the central and eastern Pyrenean Axial Zone. Cap de Creus is located at the most easter tip marked (b). A number of different facies can be found throughout the Pyrenean Axial Zone (modified from Druguet et al. 2014).

3.1 Tectonic Evolution of Cap de Creus

During the Variscan Orogeny, the rocks of the Cadaqués series in Cap de Creus were affected by polyphase deformation with three main episodes D_1, D_2, and D_3. $D_{1\text{-}2}$ is primarily associated with rigid body deformation, while D_3 is related to extensive shearing and buckling during retrograde conditions (Druguet, E., 2001; Van Lichtervelde et al., 2017).

3.1.1 D_1 - Early deformation

The oldest deformation in the area (D_1) led to the development of the first continuous and penetrative N-S trending bedding parallel schistosity (S_1) in the metasediments prior to the metamorphic climax (Van

Lichtervelde et al., 2017). S_1 trends N-S in the west of Cap de Creus and NE-SW in east the with a moderate to steep dip direction towards the east. D_1 is responsible for the boudinage of quartz-veins subparallel to S_1 and is thought to be associated with crustal thickening and the first metamorphic stage (Druguet, E. et al., 1997)

3.1.2 D2 - Prograde folding event

D_2 inhomogeneous deformation led to folding and shearing of S_1 with upright and steeply inclined axial surfaces trending NE – SW in the less deformed areas and E – W in more deformed regions. Parallel with the increase of metamorphic grade from South to North; the D_2 deformation intensity also increases towards the North. In the northern Culip region, E-W trending zones of high strain transpose S_1 into a steeply dipping S_1/S_2 foliation containing tight isoclinal D_2 folds (Druguet, Elena and Carreras, 2006). L2 lineations are generally steeply plunging towards the NW (Van Lichtervelde et al., 2017). D_2 structures are associated with a prograde LP-HT environment forming around peak metamorphic conditions, shown by the presence of syn-kinematic sillimanite porphyroblasts and the development of migmatites in most northern regions. D_2 is associated with a compression-dominated transpression deformation regime and the intrusion of the characteristic pegmatite bodies of Cap de Creus (Druguet, E., 2001).

3.1.3 D_3 - Late Structures: Shear zones

D_3 is associated with extensive strain localization and subsequent shearing during retrograde greenschist facies conditions developing a vast network of anastomosing shear zones and mylonitic foliation S_3 overprinting the pre-existing structures and foliation (Carreras, J., 2001). Strain localization is enabled by the shift from compression-dominated transpression (D_2) to strike-slip-dominated transpression (D_3). D_3 is penecontemporaneous with the intruded pegmatite bodies.

3.2 Shear Belts

The Cap de Creus peninsula is subdivided into three distinct belts based on their lithological and structural evolution: The northern high high-grade shear belt (Cap de Creus), the central low low-grade fold melt (Cadaqués), and the southern granodiorite intrusive shear belt (Roses), figure 3.2.

3.2.1 Cap de Creus - Northern Shear Belt

The northern WNW – ESE trending shear belt is dominated by an anastomosing network of NE-dipping dextral shear zones that cut across medium- to high-grade schists derived from sedimentary rock sequences of Cambrian or upper Precambrian age (Carreras, J., 1997). The schists underwent a polyphase tectonic history before mylonitization displaying two penetrative foliations (Carreras, J., 2001). The dominant foliation before mylonitization is predominantly layer-parallel schistosity (S_1). Metamorphism reached the *upper-amphibole* facies conditions with localized migmatite development synchronous with (S_2) (Druguet, E. and Hutton, 1998). A wide-spread intrusion of pegmatite bodies occurred around mid to late D_2 but preceded shear zone development. Shear zone development occurred during retrograde metamorphic *greenschist* conditions. Partial mylonite mineral re-equilibration due to the metamorphic conditions occurred through the growth of white mica, albite, epidote, chlorite, and extensive recrystallization of quartz. Most shear zones cut oblique across earlier schist foliations (S_1 and S_2) and mark a deflection and rotation of the schistosity towards σ_1. This three-dimensional information, coupled with extensional crenulations, asymmetric folds, and the attitude of stretching lineations, determines the shear sense and displacement direction(Carreras, J., 1997). Individual shear zones vary in size from centimeters to hundreds of meters. Larger shear zones exhibit a heterogeneous structure with splay-type geometries comprised of a network of smaller anastomosing

shear zones (Hippertt, 1999; Passchier and Williams, 1996). Shear zones are generally discontinuous, joining and dying out along strike. The geometry and metamorphic grade of the shear zones varies gradually across the area from north to south due to a lower metamorphic grade and higher mechanical anisotropy of the schists towards the south during mylonitization. Shear zones in the higher grade schists are narrower than their complex counterparts in the south, which display a rather late deformation history associated with folding and crenulations (Carreras, J. and Casas, 1987).

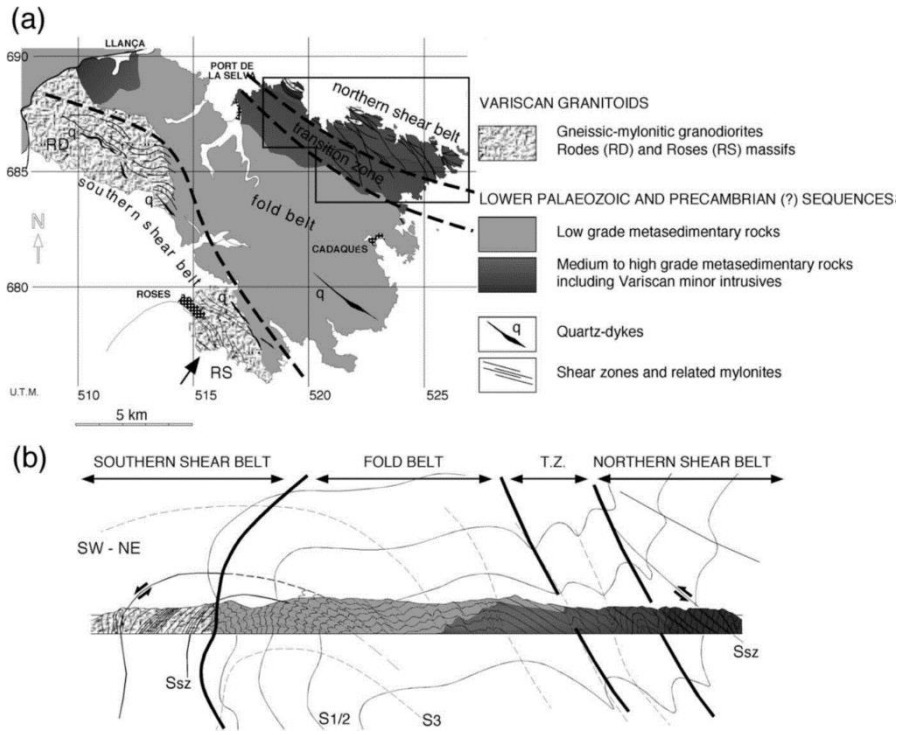

Figure 3.2 (A) Schematic map of the shear belts in the Cap de Creus peninsula displaying the two main shear belts in the north and south and the low grade fold belt in the center. (B) Schematic cross-section across the Cap de Creus Peninsula. Modified from Carreras 2001.

3.2.2 Cadaqués - Metasedimentary Central Fold Belt (Low Grade)

Shear zones pass transversely and laterally into domains of intense folding associated with total transposition of the earlier fabric, giving way to high-strain transposition bands absent of clear kinematic indicators. These structural style transitions are associated with progression into lower-grade metamorphic rocks resulting in a higher mechanical anisotropy (Carreras, J. and Casas, 1987). Rocks in this region accommodate regional strain depending on their ability to develop their mechanism of strain localization through either buckling instabilities or ductile shearing.

3.2.3 Roses – Intrusive Southern Shear Belt

The Roses section, RS in figure 3.2 (a), comprises the southern belt of the Cap de Creus Massif. Roses shear zones cut across Variscan granitoids emplaced in low-grade metasedimentary rocks (Carreras, Jordi and Losantos, 1982). Mylonite trending NW – SE shear zones in Roses display *south-dipping* attitudes with sinistral strike-slip most likely related to Alpine bulk tilting of all Variscan structures (Carreras, J., 2001; Druguet, Elena et al., 2014) along the border of the axial zone. Axial planes of

Variscan folds in the southern shear belt display this same anomalous southward tilting, causing original dextral shear zones to outcrop as sinistral. The structures in the southern belt (Simpson, C. and Sistach, 1982; Simpson, Carol, 1983) display geometries associated with isotropic rocks with XY strain plain closely related to heterogeneous simple shear (Ramsay, 1980; Ramsay and Graham, 1970).

3.3 Shear Zones

Individual shear zones in Cap de Creus are dominated by a simple shear regime characterized by a high degree of heterogeneous strain distribution. Consequently, traverse profiles display a strong longitudinal strain gradient. It is also common for shear zones to discontinue longitudinally (Carreras, J., 2001).

Shear zone boundaries display variable geometries from smooth deflection of the pre-existing foliation to sharp boundaries crosscutting pre-existing structures. Rotating the pre-existing foliation plane towards parallelism to the shear zone at slightly variable angles to the shear direction results in anastomosing networks forming at slightly different orientations. Consequently, a broad spectrum of angular relationships can be found (Carreras, J., 1997).
Foliation deflection was non-passive, as indicated by the development of minor structures such as folds, crenulations, and extensional crenulations, which rotate with increasing shear strain (Ramsay, 1980; Skjernaa, 1980). At shear zone margins, the layer's parallel foliation deflection is controlled by the most competent layers. To preserve strain compatibility at the margins, parallel flow along mica-rich planar domains occurs.

3.3.1 Anastomosing patters of shear zones

Shear zones are commonly arranged in anastomosing patterns (Corsini et al., 1996; Simpson, Carol and Schmid, 1983). The anastomosing network of shear zones is most visible in the northern shear zone of Cap de Creus. This can be attributed to the high obliquity between pre-existing and mylonitic foliation. Towards the west, the shear zones trend in close parallelism to the pre-existing foliation, making their identification more difficult (Carreras, J., 2001). Analysis done by workers such as (Carreras, J., 2001) reveals that shear zone foliation varies from W – E to NNW – SSE (predominant dextral) with a general N-to-NE dip containing a single well market stretching lineation plunging NNW. The E-W trending shear zones are more extensive and record longer and more complex kinematic patterns.

3.3.2 Shear Zone structures & microstructures

Shear zone structures are most recognizable in low-*strain domains* at the margins, while towards the interior, the high strain rate erases these structures. *Marginal folds* are most well developed in lesser crystalline, high anisotropic, and well-foliated schists. These folds initially form with axial planes and fold axis oblique to the shear plane and normal to the stretching lineation. As the strain increases, parallelism is approached due to progressive rotation. *Extensional crenulations* are also typical microstructures developed in the low-strain marginal domain. Crenulation formation occurs at a low angle (25-32°) to the pre-existing foliation parallel to the stretching lineation (Platt and Vissers, 1980). The presence of rocks with variable strengths caught in the shear zones causes the development of *pinch and swell structures*, also called drawn or necked boudins, which are a subset of boudins that retain continuity of the drawn layers but show variable thinning of the original layer thickness (Gardner et al., 2015). The asymmetry of these structures reflects the sense of shear in sections parallel to the shear direction (Carreras, J., 2001). Carreras, J., (2001) suggests that the different structures discussed

above result from instabilities formed during re-shearing of a pre-existing planar anisotropy or a newly formed foliation.

3.3.3 Shear zone development models

A two-dimensional model for the formation and evolution of Cap de Creus shear zones can be compiled (Druguet, Elena et al., 2009). The observed changes in shear-zone parallel thickness and zigzag isogons patterns indicate that pre-existing foliation was not passively sheared (Bons et al., 2004; de Creus, 2013). Instead, shearing developed from local instabilities and significant strain partitioning. Most strain partitioning occurred between the more competent Metagraywacke's and the less competent metapelites (Celma, 1982). Once instability forms within the interior of the shear zone, simple shearing takes over the way deformation is accommodated. During shearing, the pre-existing foliation does not behave passively but leads to the development of instabilities, commonly leading to the development of self-similar patterns of shear zones.

3.4 Cap de Creus - Metasedimentary Sequence

The lowermost metasedimentary sequences consist of; (i) a thick and monotonous succession of alternating metagraywackes and minor metapelites known as the Cadaqués series (Castiñeiras et al., 2008). Zircon dating of the Cadaqués series yields inherent ages of the Neoproterozoic protolith at 730 – 542 age (Castiñeiras et al., 2008; Druguet, Elena et al., 2014). (ii) Towards upper stratigraphic levels, metasediments become gradually darker and more pelitic until they form the well-distinguishable unit of black schists known as the Montjoi series. The Cadaqués and Montjoi series form the lower stratigraphic series in the Cap de Creus area. (iii) The lower series is unconformably covered by an upper series that includes calcareous, dolomite marbles, conglomerates, muscovite-rich phyllites, and amphibole-bearing feldspathic rocks of potential volcano-sedimentary origin interpreted as lower Cambrian age, which in turns is (iv) unconformably covered by a siliciclastic-carbonate series known as the Upper Norfeu Series which bounds the Roses granitoid massif (Carreras, Jordi and Losantos, 1982). The primary lithology of the Cap de Creus peninsula, schists, belongs to the Montjoi series. The schists were identified to be of *metagraywacke and metapelitic* composition rich in quartz–feldspathic and mica, forming the base composition of the Cap de Creus & Roses mylonites. Metapelites are assumed to behave as accommodation layers during shearing, undergoing a complex deformation involving flexural flow and parallel layer slip (Carreras, J., 2001). Metagraywacke's, in turn, act as competent layers due to their high crystallinity and low mica content (Hudleston et al., 1996). Quartz segregation veins and nodules are common in the Cap de Creus schists. The schistosity predominates parallel to the sedimentary bedding (S_1) with SW-NE to N-S trending foliation. As a result of heterogeneous sedimentary deposition, the metagraywackes and metapelites have variable mechanical properties and competence. *Competent schists* accommodate shearing by developing local instabilities which evolve into shear zones leading to a highly heterogeneous strain distribution. Competent schists are more susceptible to strain localization than schists with low competence (Carreras, Jordi et al., 2013). *Less competent*, medium-grade schists accommodate regional strain by developing buckling instabilities due to their high mechanical anisotropy. These schists are common in the lower-grade central region of the Cap de Creus massif. Metasediments show a metamorphic gradient from the chlorite-muscovite zones in the south to the sillimanite-K feldspar zone in the north (Van Lichtervelde et al., 2017). All metasediments display at least one penetrative foliation (S_r) developed during the Variscan orogenic event and folding during the subsequent Pyrenean event. The degree of alteration of the sedimentary

succession is variable throughout the Cap de Creus peninsula depending style of metamorphism and range in P-T conditions.

3.5 Metamorphism of the Cap de Creus Peninsula

The Cap de Creus – Roses setting is characterized by several tectonic events associated with large-scale deformation, magmatic intrusions, and metamorphism. The first metamorphic event is associated with greenschist metamorphism of Neoproterozoic - upper Ordovician sediments during the Variscan orogeny (Druguet Tantiña and Carreras, 2008; Catalán et al., 2014; Van Lichtervelde et al., 2017).

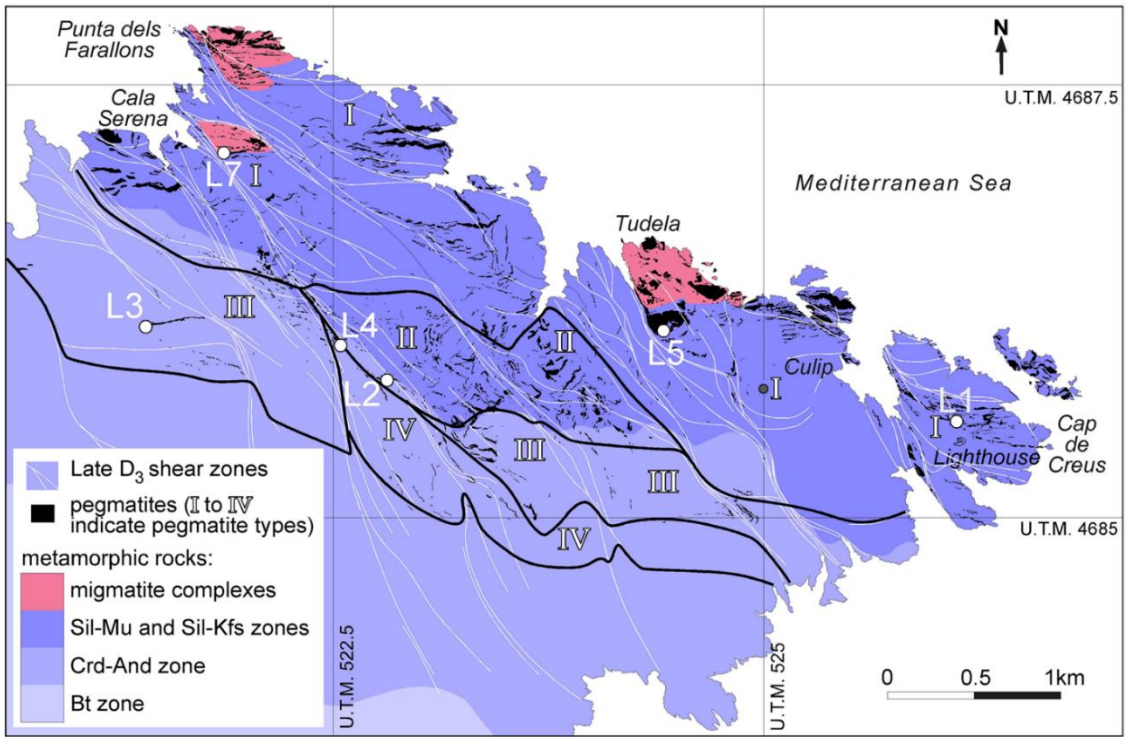

Figure 3.3 Geological map of the north Cap de Creus area, showing the distribution of the four pegmatite types (modified from Corbella and Melgarejo 1993, Druguet and Carreras (2006) and Van Lichtervelde et al., (2017)) within the three metamorphic zones (Sil-Mu: sillimanite-muscovite; Sil-Kfs: sillimanite-K-feldspar; Crd-And: cordierite-andalusite; Bt: biotite; the chlorite-muscovite zone is further to the south, out of the map). L(1-7) values are pegmatite sample locations used by Lichtervelde et al. for U – Pb dating.

Several metamorphic rocks from low to high grade can be found in the Roses – Cap de Creus setting (figure 3.3). Furthermore, several metamorphic gradients are either locally bound due to intrusions or are part of the regional metamorphic trend of increasing grade towards the north. Local metamorphism includes contact metamorphism and the development of spotted phyllites and hornfels due to the granodiorite intrusion in Roses and pegmatite intrusions in Cap de Creus. A low-grade regional metamorphic imprint marks the central zone (Cadaqués) between Cap de Creus and Roses. Granitoid batholiths and stocks are abundant in the Cap de Creus basement, generally accepted as emplaced during the main metamorphic event. The northern domains contain migmatite cores associated with minor funnel-shaped intrusions of mantle-derived magmas (Druguet 2001).

Three main metamorphic gradients can be found in Cap de Creus, increasing in grade towards the NE;

1. Bt: biotite - chlorite
2. Crd-And: Cordierite - andalusite
3. Sil-Kfs: sillimanite - K-feldspar
4. Sil-Mu: sillimanite - muscovite - Garnet
5. Migmatites

The metamorphic grade ranges from Greenschist facies to Amphibolite and Granulite facies for the Gneiss and migmatite zones. Non-linear isograds bound metamorphic zones.

3.5.1 Mylonites (Roses)

There are two main reasons for considering the mylonites in the Roses Granodiorite to be of Variscan age: firstly, they are cut by undeformed basic dykes attributed to the late Triassic-early Jurassic, and secondly, the mylonites show microstructural and mineralogical features indicative of deformation under retrograde greenschist facies conditions associated with D_3. A great variety of mylonites of the Variscan age (Carreras, Jordi and Losantos, 1982) can be found as a result of lithological heterogeneities and inconsistencies in deformation conditions that range in space and time from the (earliest) upper greenschist facies in the northern shear belt to the (later) and lower greenschist facies in the southern shear belt. Mylonites, as with schists, display penetrative foliation and compositional banding with segregated quartz nodules and veins that are alighted with the instantaneous strain axes (ISA). Banding results from mechanical stretching without chemical differentiation (Myers, 1978; Carreras, J. and Druguet, 1994). Banding and mylonite foliation are commonly folded and extended by crenulation cleavage related to the difference in competence between layers (White et al., 1980). Flow disturbance is common in shear zones that coalesce or where the shear direction changes. Thus, these internal fold structures can be considered to reflect the reactivation of already-existent mylonitic foliation. Some leucocratic quartz–feldspathic mylonites contain deformed pegmatite dykes and granitoid bodies (Carreras, J. and Druguet, 1994). Minor types are amphibole-bearing mylonites derived from amphibolites or tonalites (Carreras, J., 2001). Alignment of quartz-related mineral crystals (e.g., tourmalines) due to preferred solid crystallographic orientations exhibit defined stretching lineations (Celma, 1982; Carcia Celma, 1983).

3.6 Magmatism of the Cap de Creus Peninsula

The Cap de Creus massif is associated with the widespread emplacement of batholiths and stocks ranging between granodiorite, granites, and leucogranites. Three groups represent the Variscan Igneous activity in Cap de Creus based on the level of emplacement: (i) Roses granodiorite dated at ca. 291 Ma (Druguet, Elena et al., 2014); (ii) Pegmatite dykes swarm in the cordierite – andalusite zone dated at ca. 299 Ma and (iii) intrusion of quartz diorites and granitoids. In Cap de Creus, the felsic magmatism is predominant in late intrusions emplaced at shallow levels, while more mafic gabbros, diorites, and tonalites are older and deeper seated in higher metamorphic gradients. Field studies of the emplacement of granitoids indicate the emplacement mainly occurred during the main Variscan compression-dominated transpressive event D_2 (Gleizes, G. et al., 1997).

3.6.1 Migmatites

In the high-strain and high-grade metamorphic zone north of the Cap de Creus massif, small bodies of quartz gabbros and diorites are surrounded by migmatite complexes. The plutonic rocks emplaced into

the migmatite complexes include a calc-alkaline association from older to younger that includes quartz gabbros, quartz diorites, tonalites, granodiorites, granites, and peraluminous leucogranites and pegmatites (Druguet, Elena et al., 2014). Migmatites can be found in Cap de Creus at the northern margin of Tudela within the *sillimanite-K feldspar* metamorphic zone. Migmatite complexes are interpreted by (Druguet, Elena et al., 2014) as deep-seated structures formed during peak metamorphic conditions coeval with D_2 and intruded by a mix between mantle melts and crustal contaminants.

3.6.2 Granodiorites

The Roses intrusive body forms a small elongated body of heterogeneously foliated granodiorites of late Variscan age that constitutes the easternmost granitoid intrusion outcrop along the Pyrenean Axial Zone (Carreras, Jordi and Losantos, 1982). The granodiorite intruded the metasediments consisting of phyllites and metagraywackes at different stratigraphic levels, cutting across the regional foliation. The Roses intrusion is interpreted as a late intrusion, cutting across tectonic structures formed during earlier Variscan orogenic events. Post-emplacement deformation is accommodated as progressive ductile shearing, developing homogeneous mylonitic foliation along bands, giving rise to mylonitic granodiorites under greenschist metamorphic conditions (Carreras, Jordi et al., 2004). These bands vary in width from a few centimeters to hundreds of meters. Dating of secondary zircons places the Roses intrusion at 290.8 ± 2.9 Ma, late D2 but pre-D_3 strike-slip dominated transpression (Druguet, Elena et al., 2014).

Internal structures in the undeformed granodiorites

The Roses granodiorite is rich in micro-Qtz-diorite enclaves and magmatic schlieren that display a preferred orientation. Many younger aplite dykes cuts across the granodiorites with variable orientations (Carreras, Jordi et al., 2004). Xenoliths and metasediment inclusions are also locally observed within the granitic body. Along the margin of the intrusion, leucocratic granitoids are predominant, intruding the surrounding metasedimentary country rock in the form of granodiorite dykes. The bulk composition of the undeformed biotite-hornblende granodiorites consists of quartz oligoclase-andesine, K-feldspar, biotite, and hornblende (Carreras, Jordi and Losantos, 1982).

Internal structures in the deformed granodiorites

Late Variscan deformation and subsequent strain localization in the form of mylonitization of the granodiorites at shear zones show a strong penetrative sub-parallel foliation predominately trending NW-SE with a steep dip towards SE. It is important to note that NE dip deflection does occur occasionally. Less deformed granodiorites have narrower mylonitic zones that exhibit extensive mineral elongation parallel to the displacement direction. The mylonitic foliation displays crenulations and folding in less competent layers with the fold-axis parallel to the mineral elongation lineations. Mylonitization of the granodiorites is always concurrent with drastic grain size reduction, mineralogical changes, and overprinting, as seen in chlorite, epidote, muscovite, and albite growth. Micro-folding and crenulations in the metamorphic contact aureole between the granodiorites and metasediments appear to post-date the intrusion event as can be seen by crenulation folds wrapped around nodular porphyroblasts in the phyllites. The Roses granodiorite is considered a late intrusion of the Variscan age since it cuts across the younger regional schistosity ($S_{1\text{-}2}$) but is still affected by D_3 shearing. The post-emplacement deformation event D_3 is responsible for the heterogeneous deformation ranging from regular gneissic foliation to strong mylonitization along narrow shear zones.

3.6.3 Pegmatites

Peraluminous pegmatites in Cap de Creus occupy the apical parts of larger batholiths and represent the ultimate anatectic-granitic differentiates of magmatic fractionation. Pegmatites intruded extensively into high to medium-grade schists in the northern area of Cap de Creus.

The frequency and magnitude of each intrusion can be strongly linked with the metamorphic and temperature grade. In high-grade rocks in the north, the frequency and size of the intruded dykes are significantly more ample than in the south, where dykes are smaller and less frequent. The intruded pegmatite dykes generally run parallel with the main S_2 foliation and are locally affected by late shearing. Pegmatites that cut the S_2 foliation are locally affected by ductile folding.

Different types of pegmatites crop out in Cap de Creus, ranging from less evolved I-type to more developed IV-type following the classification by (Černý and Ercit, 2005), figure 3.3:

- I-type (pegmatite granite): K-feldspar pegmatite, least evolved (296.2 ± 2.5 Ma – 301 ± 3.8 Ma). Lighthouse area.
- II-type (beryl-columbite subtype): Transitional pegmatites with quartz cores marker minerals, including albite, beryl, and phosphates.
- III-type (beryl-columbite-phosphate subtype): This pegmatite type has larger quartz cores, well-developed muscovite units, and garnet/beryl marker minerals.
- IV-type (albeit subtype): Most evolved pegmatite containing Li – Mn phosphates, Beryl, and montebrasite as characteristic minerals.

Type I and II pegmatites occupy the high D_2 strain rocks of the migmatite and sillimanite-muscovite metamorphic zones along the northern coast. In contrast, types III and IV occupy the medium-grade rocks south of the cordierite-andalusite metamorphic zone (Van Lichtervelde et al., 2017). The size and frequency of pegmatites decrease from type I to type IV (Corbella and Melgarejo, 1993). The exact emplacement timing between pegmatites is variable, with some pegmatites intruding early to syn-D_2, subsequently undergoing S_2 parallel shearing, while other Late-to-Post-D_2 pegmatites were not subjected to significant deformation. U – Pb dating of magmatic zircons extracted from Cap de Creus pegmatites placed Type I and III intrusions at ca. 299 Ma (Van Lichtervelde et al., 2017). Although pegmatites were not all emplaced simultaneously, Van Lichtervelde et al., through their U – Pb dating, indicate that most pegmatites were emplaced synchronously with the D_2 deformation event and the associated thermal peak of metamorphism. The high standard deviations of in-situ U-Pb geochronological methods inhibit the distinction between separate pegmatite pulses.

4. Remote Sensing Approach and Methodology

The following chapter introduces the approach, methodology, and reconstruction techniques from digital imagery to three-dimensional datasets that can be used to extract quantitative structural measurements and make qualitative Geologic observations and interpretations.

4.1 Photogrammetry

Over the last decade, Photogrammetry has revolutionized the digitizing process of surface topography. Photogrammetry has proven to be an affordable alternative to 'Light detection and ranging (LiDAR)' techniques and is widely used in many different fields, including machine vision, topographic mapping with small UAVs (Lejot et al., 2007), architecture (Yilmaz et al., 2008), archeology (De Reu et al., 2014) as well as many fields in geosciences such as planetary sciences (Haruyama, 2012), paleontology (Mallison and Wings, 2014) geomorphology (Javernick et al., 2014), Physical geography and tectonics laboratory experiments (Galland et al., 2016). Contrary to LiDAR, Photogrammetry is a post-processing technique using advanced Graphical Processing Units (GPUs) to process many 2D frames into a 3D model. Done correctly, photogrammetry yields high-resolution textured models and is user-friendly, relatively fast, inexpensive, and highly scalable (e.g., Google Earth 3D).

The photogrammetry method involves taking photographs of an object from many viewing angles around the object (N-view), figures 4.1 and 4.2.

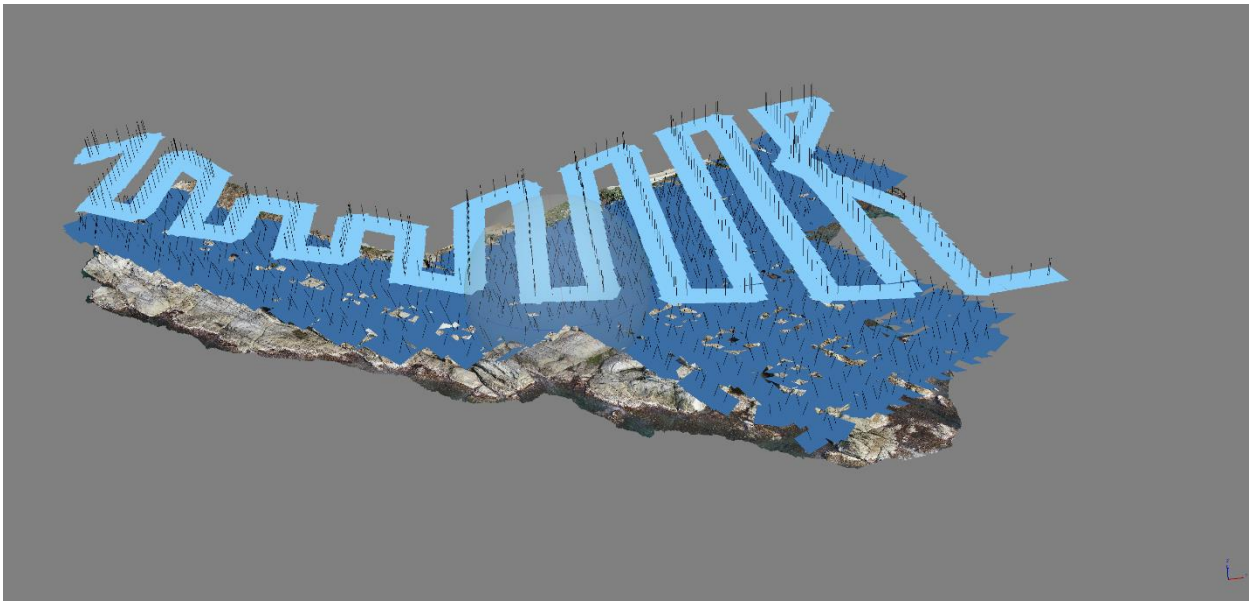

Figure 4.1 Photographs are taken from many different locations and viewing angles around the object to achieve proper image overlap for reconstruction. For this reconstruction of the Roses granodiorite, two separate flights were executed at a high altitude (light blue) and a low altitude (dark blue). Each frame is taken at a slight angle (off-nadir) to facilitate 3D reconstruction.

These photographs are used to generate a 3D model computationally by comparing known features across individual photographs. The automation of this process through what is known as *Structure from motion (SfM)* sits at the core of what made this application popular for a wide range of applications. The main concepts were laid out by (Koenderink and Van Doorn, 1991) and later shaped into a highly efficient and easy-to-use software package by (Snavely et al., 2006; Snavely et al., 2008). This study used

the photogrammetry SfM-based software package Agisoft Metashape® due to its versatility and feature-rich environment.

Generating a 3D model from photographs involves a multi-step process (figure 4.2);

i. An algorithm finds specific tie points on each image using e.g. the SIFT algorithm (Lowe, 1999; Lowe, 2004), SURF (Bay et al., 2006), or ASIFT (Lowe, 1999). A tie point is a negative or positive peak in brightness intensity. Continuous gradients or small amplitude peaks will not yield tie points (Rosu et al., 2015).
ii. The following step involves comparing the tie points from all photographs to find corresponding image parts and mathematical relations between them using, e.g., the RANSAC algorithm (Fischler and Bolles, 1987). During this step, tie points are used to compute the camera's relative positions, viewing angles, and distortion of the optics.
The output of this task is comprised of a *sparse point cloud* with 3D coordinates (XYZ).
iii. The sparse cloud can now be manually cleaned and optimized to reduce reconstruction errors by adjusting the tolerances in the following camera alignment parameters within Metashape: (i) Reprojection error, (ii) Projection accuracy, (iii) reconstruction uncertainty, and (iv) the number of cameras used to determine each point.
iv. The model can be optimized concerning relative and absolute (GPS) accuracy by adding markers known as ground control points (GCPs) in surveying applications.
v. All remaining tie points are used to construct either a depth map or a high-density point cloud which very closely represents the actual shape of the landscape.
vi. The dense cloud can be turned into a polygon mesh which consists of triangles that connect the points. The polygon mesh can be split into a tilled model for more effective rendering.
vii. Texture maps can be computed from the photographs by assigning (U, V) coordinates to each triangle vertex representing a point in the texture map. These allow for the cropping of each triangle in the texture map and subsequently project the texture onto the corresponding triangle on the mesh.
viii. Based on absolute and or relative camera positions and orientations, an orthorectified image can be produced that is geometrically corrected with regards to (i) geometry distortion, (ii) lens distortion, and (iii) camera tilt (Gwinner et al., 2016). The orthophoto can measure accurate horizontal distances if absolute camera positions are used in the reconstruction.

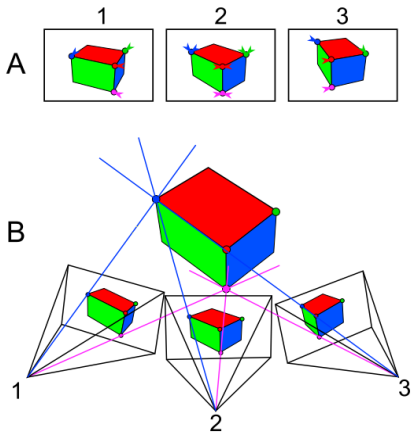

Figure 4.2 Schematic drawing of the two main image processing steps in SfM. (a) - An algorithm finds specific known points across all images from different viewpoints. (b) The algorithm compares the points obtained in step (a) from all images to find corresponding image parts and mathematical relations between them (Diagram from (Galland et al., 2016).

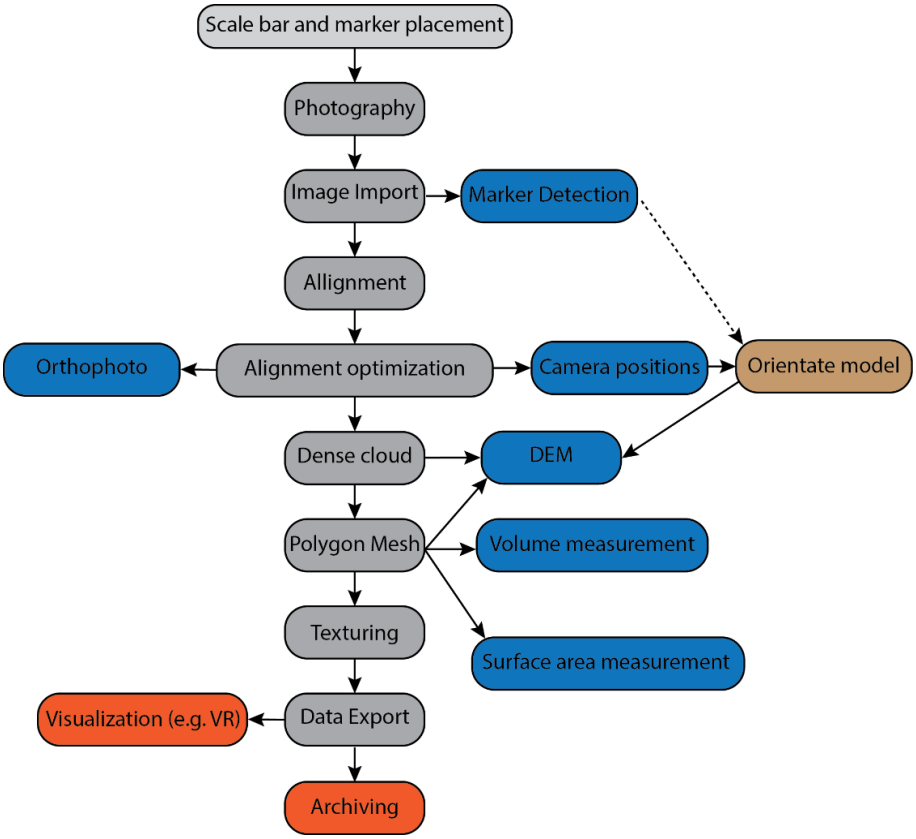

Figure 4.3 Standard photogrammetry workflow diagram from image import to export and visualization. After export, the rendered 3D models can be imported into Geoscience model interpretation software such as VRGS. Diagram from Sibbel., 2017.

The quality of the topographic reconstruction varies considerably and is dependent on many factors such as; (i) Sensor resolution, (ii) camera calibration, (iii) Angles between photographs, (iv) Overlap between photographs, (v) Quality of the images, (vi) Data processing accuracy, (vii) distance to subject and (viii) movement distortion. These parameters are elaborated in more detail in the following sections.

4.2 UAV – Unmanned Aircraft Vehicle

Unmanned aerial vehicles, also known as UAVs or drones, are remotely piloted aircraft capable of autonomous flights. UAVs are classified into fixed-wing, multi-rotor, hybrid, and blimp/airship platforms. The most commonly used platforms for aerial surveying are (i) fixed-wing, used for covering large distances but at a lower spatial resolution. (ii) Multirotors, which have a lower action radius but can lift off vertically in confined spaces, fly closer to the ground and slower, enabling Multirotors to achieve a higher spatial resolution and better image quality.

In this study, we employ a multirotor UAV (DJI phantom 4 pro), specifically a quadcopter with a total of four blades and a take-off weight below 2 kg (figure 4.4 & Table 4.1). This aircraft can be used for surveying up to several Km^2 on a single battery. A damped gimbal attached to the quadcopter automatically stabilizes the camera along three-axis and removes vibrations inherited from the motors and airframe. The gimbal allows for capturing nadir and off-nadir imagery while in motion.

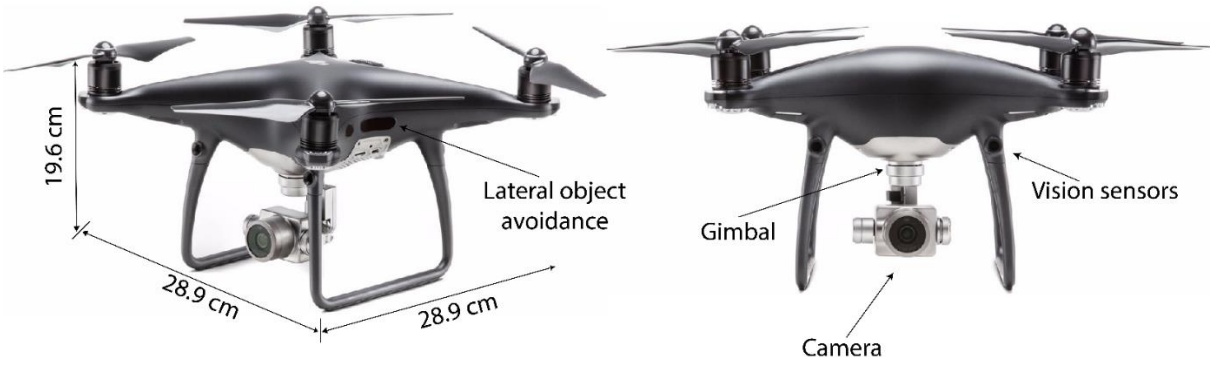

Figure 4.4 **DJI Phantom 4 Pro obsidian side and frontal view. The UAV is a perfect x-shaped quadcopter (same distance between motors).**

The table below lists the specifications for the DJI Phantom 4 Pro.

Parameter	Value
Name	DJI Phantom 4 Pro (V1)
Weight (loaded)	1388 g
Max flight time	30 min
Operating temperatures	0° to 40°C
Satellite positioning system	GPS/GLONASS

Hover Accuracy	0.1 m (vertical), 0.3 m (Horizontal)
Vision system	Backward, forward and downward
Operating frequency	2.4 and 5.8 GHz
Battery	LiPo 4S1P, 15.2V nominal, 5870 mAh
Stabilization	3-axis (pitch, roll, yaw)

Table 4.1 DJI Phantom 4 Pro technical specifications. The DJI Phantom 4 is a professional commercial UAV.

This UAV was selected due to its low barrier to entry and shallow learning curve, allowing novice pilots outside the remote sensing industry to pick up the pace quickly and focus on their research tasks without extensive training. This lower barrier to entry will make it easier for geologists worldwide to deploy their UAVs as research tools.

The main challenges of using UAVs as research tools can be attributed to three categories:

i. Natural
ii. Technological
iii. Legal

(i) The first point primarily concerns weather conditions such as rain, temperature, and high-speed winds. Most UAVs are not waterproof, making operation impossible during rain. High-speed wind can easily disturb the movement and regular operation of the vehicle. Finally, temperature impacts the onboard electrical components and battery, making surveying in extremely cold or hot environments difficult. (ii) each UAV has technical limitations, including flight time, signal range, and speed limits. These factors limit the size of the object or area that can be surveyed. Most importantly, (iii) the legality of the ability to carry out an aerial survey in the area of interest and the compliance with safety operating regulations, something that should not be taken lightly.

4.3 UAV Photogrammetry

The term UAV photogrammetry was first introduced by (Eisenbeiß, 2009) to describe the digital photogrammetric processing of images that have been acquired by a remotely controlled, semi-autonomously, or autonomously airborne platform (Vollgger and Cruden, 2016). Airborne photogrammetry allows for the computation of georeferenced and colored dense point clouds, digital elevation models, and orthophotos of topographic structures from a sequence of overlapping images obtained from different viewing angles above the ground surface (OFF-NADIR). UAV photogrammetry collects images with a camera mounted below the moving UAV. This technique bridges the gap between classical aerial surveying from a plane or satellite and terrestrial surveying. The main advantage of UAVs over the last few years is their increasing ability to systematically and inexpensively acquire high-resolution aerial imagery at low altitudes. They can obtain data in remote, difficult-to-access, or dangerous areas such as cliffs, rock falls, and mining pits. Unlike Google Maps® or regular aerial photos, structures imaged by UAVs provide greater detail at small scales (Helmke et al., 2007).

4.4 General Workflow and Points of Caution

Surveying with UAVs is a precarious and exact task due to the magnitude of systems, conditions, and parameters that must be managed and considered. These include (i) weather conditions, (ii) flight planning, (iii) Capture of (accurate) ground control points (GCPs), (iv) Hardware checks and takeoff-landing site selection, (v) Pre-flight checks, (vi) Surveying missions and in-flight monitoring, (vii) Safety and regulation compliance and (viii) image acquisition strategy and settings.

Skipping even a single step can physically damage the equipment and life or result in inaccurate reconstructions. This is why a multi-step system was constructed to lower the margin for human error. Below we elaborate on the general workflow regarding flight planning and execution.

Step 1. Weather conditions

UAVs are very sensitive to wind, rain, and extreme temperatures. The following factors should be taken into account when planning a survey mission.

1. High wind velocities will reduce the effective horizontal displacement efficiency of the aircraft and the coverable flight area per battery. Additionally, the wind will induce vibrations propagating into the captured imagery as blur.
2. Rain will damage electronics and cover the camera lens. It is recommended to fly in fair weather conditions.
3. Terrain and cloud shadows will induce different lighting conditions, which should be avoided as much as possible due to the negative impact on the photogrammetric SFM reconstruction.
4. Lastly, a suitable time of day to carry out flights should be selected to ensure the best operating lighting and temperature conditions. This will prevent the aircraft from undercooling or overheating, especially the LiPo battery, which has an operating temperature of between -10 and 40°C.

Step 2. Flight planning

Before any flights are done, the following parameters should be analyzed: (i) The target mapping surface area; (ii) the presence of any obstacles (e.g., trees, powerlines); (iii) terrain types and differences in altitude between the highest and lowest points in the area of interest; (iv) maneuverability space if trenches are present and (v) human accessibility to the area.

With these initial checks completed, a good estimation can be made regarding the number of flights to execute, the flight altitude, and the mapping strategies.

Step 3. Ground control point (GCP) placement and measurement

Physical ground control points (GCPs) in the form of markers should be placed within the mapping area and measured with a GNSS receiver to georeference the model accurately. The markers should be visible from the air and put away from vegetation. Placing the markers requires access to the area of interest.

Step 4. Hardware check and takeoff-landing site selection

An appropriate flat and obstacle-free takeoff and subsequent landing location should be selected with a minimum of 100 m^2 to account for the GPS accuracy error. The landing pad should be placed in this location to prevent any solid particles from getting blown into the camera lens and motors of the UAV. Care should be taken not to select this site on busy roads. After the landing site selection, the drone should be placed on the landing pad with the battery plugged in but turned off.

Next, inspection is carried out on the aircraft with emphasis on (i) propellers placement and orientation, (ii) smoothness of motor rotation (e.g., no grinding noise),(iii) general structural integrity of both the airframe and camera-gimbal system, (iv) battery placement and charge level.

Step 5. Pre-flight checks

A mobile device is placed on the radio transmitter (RC) with a USB going from the RC to the mobile device. The RC is powered ON. After the RC has power, the UAV can receive power (only in this order).

After initialization, some steps should be carried out:

i. Launch the DJI Go app on the mobile device and wait for the app to check the firmware and connect with the UAV.
ii. Once connected, a check should be made for any on-screen errors or inconsistencies.
iii. The aircraft should remain on the ground until it is connected to at least 12-14 satellites to update the home point (RTH).
iv. Start the motors and inspect for any irregular noises or behavior.

Step 6. Surveying missions and in-flight monitoring

In this step, the mapping missions are manually or automatically executed.

During each flight, parameters should be closely monitored;

i. *Flight distance and altitude*. These should always remain within the legal limit.
ii. *Point of no return*. Traveling further than the point of no return should be prevented at all cost, as the UAV might not be able to travel the total distance back.
iii. *Wind speed*. Excessive wind speed can cause unwanted vibrations and flight behavior and reduce the point of no return in the case of a headwind.
iv. *Battery voltage*. Even though reliable, LiPo (Lithium Polymer) batteries can fail at any moment without any warning. This phenomenon occurs in the form of large irregular voltage fluctuations. Furthermore, it is essential not to plan flights beyond the 30% battery capacity safety limit.
v. *Temperature*. High temperatures increase LiPo's combustion potential and can cause permanent danger. This is why flights in desert regions should be taken early or late in the day. Furthermore, it is vital not to ignore equipment battery models.
vi. *Fly LOS (line of sight)*. It is vital to have LOS on the aircraft and not fly behind large structures, as this can cause RC or video-link failure.
vii. *Never fly above people.* Flying above people is illegal and dangerous.
viii. *Always be ready to regain manual control of the aircraft.* If any errors were committed during automated mission planning, it is vital to regain manual control and land the UAV safely.

The following section will discuss more in-depth, quantitative, and technical explanations involving the crucial parameters for successful mapping missions.

4.5 UAV Digital Camera and Lens (Payload)

The input for structure from motion reconstruction algorithms used in photogrammetric software consists of high-quality digital imagery. An in-depth understanding of image acquisition is necessary to obtain the highest-quality dataset possible.

For this project, the DJI Phantom 4 Pro camera was used. Specifications are listed in the table below, Table 4.2. The camera is mounted on a 3-axis gimbal with a rubber dampener to avoid high-frequency vibrations from entering the camera sensor.

Parameter	Value
Sensor	CMOS
Maximum image resolution (pixels)	5472x3648
Sensor dimensions (mm)	13.2x8.8
Effective pixels	19,961,856 (20M)
Field of view (°)	84
Sensor aspect ratio multiplier	1.5
Aspect ratio for true sensor resolution	3:2
Sensor crop factor (focal length multiplier)	2.72
Focal length (mm)	8.8mm and 23.936 for 35mm format equivalent
Aperture	f/2.8-f/11
Shutter type	Mechanical

Table 4.2 Phantom 4 pro camera specifications. The camera is mounted below the UAV on a 3-axis gimbal.

The deployed sensor is very well suited for photogrammetric surveying due to its large image resolution and mechanical shutter, which prevents the 'rolling shutter effect' during the capture on a non-still airborne vehicle. The acceptable aperture allows for an excellent depth of field to maintain both the foreground and background in focus.

4.6 UAV Camera Settings

The table below, Table 4.3, lists the camera settings used for all flights.

1. ISO was set to 100 to minimize the noise in the images.
2. The image aspect ratio was set to 3:2 to achieve maximum image resolution.
3. The shutter speed was set at 1/360s to avoid motion blur.
4. The aperture was kept on automatic to accommodate the constant shutter speed.
5. Exposure was set to manual to achieve consistent results across all images.
6. Focus was kept on AF due to the significant relief gradient higher than the depth of field.

Parameter	Value
ISO	100
Image aspect ratio	3:2
Shutter speed	1/360s
Image capturing mode	Shutter priority
Aperture	Variable but above f/2.8
Exposure	Manual
Focus	AF

Table 4.3 Camera settings used during image acquisition. Settings were adjusted within the DJI Go app.

4.7 Mission planning

To achieve accurate 3D reconstruction, it is vital to (i) have a large number of viewing angles relative to the surface of the survey area and (ii) enough overlap between images. Sufficient overlap will ensure enough tie points to match specific features across all images. If the surface topography is relatively flat, nadir images can capture the surface successfully, as there are few viewing angles. However, more viewing angles are required to reconstruct larger and steeper topographic gradients accurately. For geologic mapping, the topographic gradient and the number of overhanging structures almost always

fall outside the capability of nadir imagery acquisition for accurate 3D reconstruction. That said, if only 2D XY orthophotos are required, nadir acquisition will suffice.

With an emphasis on the explanation above, this study deployed three different mapping mission strategies using pix4Dcapture®, Table 4.4. This application allows direct flight planning on a mobile device transferred through the RC controller to the UAV.

Mission plans	Value
Single grid	Single-pass
Double grid	2x passes
Circular orbits at variable heights	5m vertical spacing
Free flight	2m horizontal and vertical image trigger
Ground level photography	No fixed distance. As many as required.

Table 4.4 Image acquisition mission plans. All missions were carried out for each outcrop in no particular order.

Single grid

For each location of interest, a single nadir grid mission was carried out at an altitude between 100 and 120m to achieve a Ground Sampling Distance (GSD) between 1-3 cm. Nadir images were collected to ensure a high spatial resolution consistency throughout the survey area. The resulting images were used to reconstruct a 2D (XY) georeferenced orthophotograph and imported into QGIS for processing and map generation. The compiled maps provide an excellent alternative to google maps (10-20 cm/pix) for an initial survey of large-scale structures.

Double Grid

This mission acquires non-nadir images with a camera angle of 70°. This mission consists of overlapping two single grid missions rotated 90° from each other. Each point grid intersection will contain 4x photographs with different orientations and, thus, different viewing angles, resulting in 3D models with higher relative accuracy, figure 4.6.

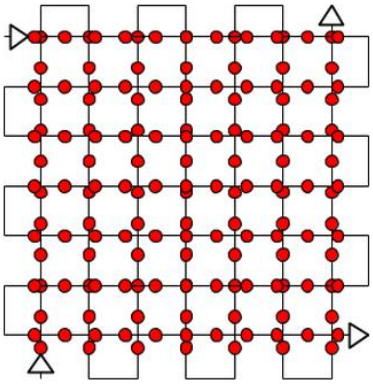

Figure 4.5 Double grid mission. Image from Pix4D support website. A dual grid mission is used for 3D reconstruction by obtaining different viewing angles of the same feature.

This mission should cover approximately 20-30% more surface area than required to avoid low-resolution model edges. If multiple flights are needed, sufficient overlap between datasets should be maintained to ensure the datasets can be stitched into a single model, figure 4.7.

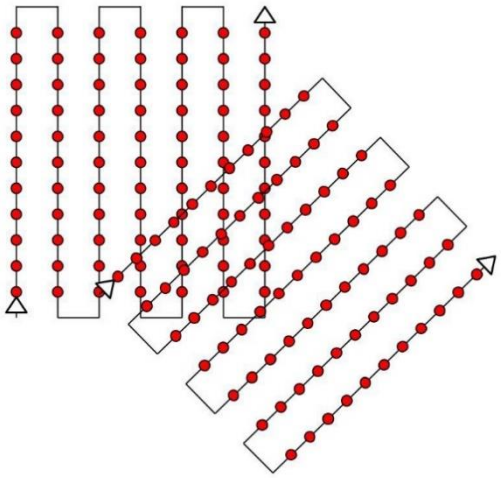

Figure 4.6 Double grid mission overlap for datasets acquired during different flights. A sufficient overlap should exist to match different datasets with each other. Image from Pix4D support website.

Circular orbits

Even though double-grid missions cover more viewing angles than nadir imagery, more extensive geologic features with overhanging zones will still lack side view coverage. Flying orbital missions with shallower camera angles as the UAV gets closer to the ground is part of the solution, figure 4.8. These orbits can be viewed as horizontal sections from a semi-sphere. This method ensures the same distance to the center of the target area is maintained, which is essential to preserve the spatial resolution of the model. The vertical spacing between orbits is approximately 5 m, with the lowest flight at 10 m altitude, which would result in three iterations for a grid mission of 25 m altitude. A picture is taken every 10° in the XY plane.

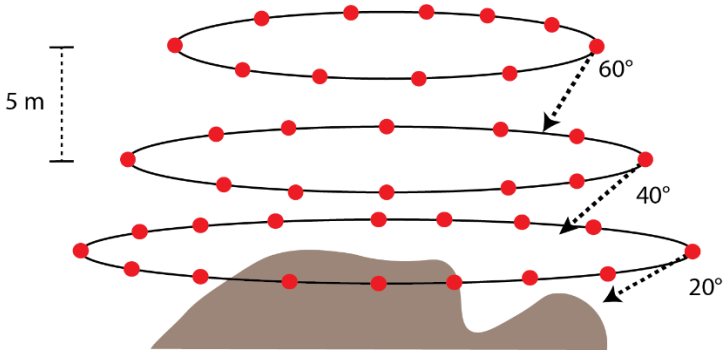

Figure 4.7 Schematic illustration of circular orbit missions around the survey area to increase viewing angles and map accuracy.

As the above figure shows, the closer the orbits get to the ground, the wider the flight radius, which is done to ensure (i) constant distance to the center of the survey area and (ii) flying further away places the foreground and background closer together and thus the depth of field is reduced.

Free flight

Even though double pass and orbital missions can capture good quality data for 3D model reconstruction, it is not sufficient if data is required to study specific small-scale features with high

resolution and accuracy, in which case, oblique and semi-oblique imagery has to be obtained. Manual flights should be carried out with automatic image triggering every few meters vertically and horizontally to ensure sufficient overlap.

Ground level

Oblique geologic features very close to the ground can be dangerous to capture with a UAV due to risks associated with flying at very low altitudes. To acquire low-altitude imagery, a DSLR (Nikon 5300) on a tripod with a remote shutter and built-in GPS can be used for photograph acquisition, Table 4.5. Care must be taken to ensure the camera settings are comparable to the UAV and enough overlap exists between the DSLR dataset and the remote aircraft to avoid heterogeneities and overall errors in the results (Mikolajczyk et al., 2005).

Parameter	Value
Sensor	DX APS-C (CMOS)
Maximum image resolution (pixels)	6000x4000
Sensor dimensions (mm)	23.5 x 15.6
Effective pixels	24.2M
Sensor aspect ratio multiplier	1.5
Sensor crop factor (focal length multiplier)	1.5
Focal length (mm)	18-105 mm and 27mm for 35mm format equivalent
Aperture	f/3.5-f/5.6
Shutter type	Mechanical
Lens	Kit
Minimum focus distance	45 cm

Table 4.5 Nikon D5300 camera specifications. The camera is mounted on a tripod and triggered with a remote shutter. A fixed focal length is used to avoid different degrees of lens distortion.

Agisoft Metashape® and Pix4D® recommend a focal length between 20 to 80 mm in 35mm film equivalent (Agisoft Metashape User Manual, Pix4D support website).

*35mm equivalent = crop factor * actual focal length* *(1)*

This implies maintaining a focal length between 23mm and 56 mm on the camera lens. Furthermore, high apertures between f/8 and f/16 are recommended to ensure maximum depth of field and subsequent sharpness of the foreground and background in the images. It should be noted, however, that for oblique photogrammetry of relatively smooth surfaces, the importance of high apertures is less relevant. Care should be taken not to go beyond f-stops of (f/16) as this will induce diffraction and lower the overall sharpness of the images.

4.8 Mapping Survey Execution

Preceding every survey mission, a free flight is carried out to explore the area and flying conditions. Emphasis is placed on (i) RC and video link signal strength throughout the area of interest, (ii) wind conditions as higher in the air it is not uncommon for the wind to be stronger than close to the ground.

All missions detailed above are executed in order of increasing complexity. This is done to safely get accustomed to flying in the area of interest. The different flights are done in the following order:

i. Single grid mission
ii. Double grid mission
iii. Circular orbits
iv. Free flights
v. Ground photography

Table 4.6 below contains essential mapping parameters used in the Cap de Creus.

Parameter	Value
Single grid mission (AGL)	100 - 120 m
Grid mission (AGL)	30 - 50 m
Single pass (GSD) - For 2D reconstruction	1-2 cm
Double pass (GSD) - For 3D reconstruction	2-5 mm
Image side overlap	>75%
Image forward overlap	>85%
Flight line spacing	Depends on altitude
Shutter interval	Depends on quadcopter speed (<5 s).
Horizontal speed	5 - 10 m/s
Circular orbits capture angle	10°
Double grid mission(s) camera angle	70-80°

Table 4.6 Cap de Creus Survey mission parameters. Missions are flown to obtain the correct Ground Sampling Distance to enable quantitative structural measurements. If GSD is too high, individual structures can't be differentiated.

It is important to note that although the Phantom 4 Pro is capable of horizontal speeds of over 20m/s, flying at this speed will increase warping in the acquired images. It was chosen to fly relatively slowly to minimize this effect. Both the flight line spacing and shutter interval depend on the altitude and type of mission. The higher the flight, the larger the line spacing due to the more surface area captured; thus, the overlap between images also increases.

4.9 Ground sampling distance (GSD) calculation

The Ground sampling distance (GSD), also known as spatial resolution, is the distance between two consecutive pixel centers measured in the field. This distance is quantitated in cm/pix. The higher the GSD, the lower the spatial resolution. This value is related to the following parameters displayed in table 4.7:

Parameters controlling the Ground sampling distance (GSD)
Sensor width (S_W), Sensor height (S_h)
Focal length (F_R)
Flight height (H)
Image width (imW) and height (imH)

Table 4.7 Parameters controlling the Ground Sampling Distance (GSD). The dynamic parameter is only the flight height. The image and sensor details are fixed and are found in the image sensor datasheet.

Increasing the flight altitude or decreasing the focal length, assuming the Field of View (FOV) remains constant, increases the GSD as the same number of pixels are captured over a larger area and thus decreases the spatial resolution. The schematic illustration in figure 4.9 below displays the parameters necessary to calculate the GSD for the width of a pixel. Because pixels projected onto the ground are not

perfectly square, the GSD should be calculated for both the width and height of the sensor. The highest value should then be taken as the GSD.

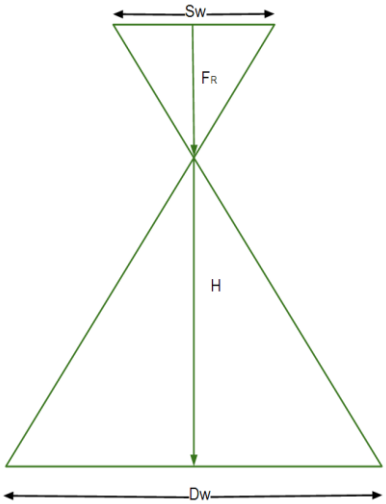

Figure 4.8 Schematic illustration of the relevant factors for calculating GSD. Dw represents the footprint width/distance covered on the ground by one image; see formula (2).

With the two formulas below, one can calculate the GSD for the width of the pixel (GSD (w)) and the height of the pixel (GSD (w)).

$$GSD(w) = \frac{H \times Sw}{imW \times Fr}, GSD(h) = \frac{H \times Sw}{imH \times Fr} \quad (1)$$

The formula below calculates the distance covered on the ground by one image (spatial resolution).

$$D(w) = \frac{GSD \times imW}{100}, D(h) = \frac{GSD \times imH}{100} \quad (2)$$

Several pre-made calculators (e.g. Pix4D) are available to facilitate the calculation of these parameters. In Table 4.8 below, some of the advantages and disadvantages are presented regarding changing the flight altitude and focal length of the camera of the UAV.

Action	Advantage	Disadvantage
Increase flight altitude or decrease focal length	1. A lower image rate is necessary to maintain overlap. 2. Shorter flight times. 3. A lower amount of processing. 4. Fewer problems with depth of field.	1. Higher GSD and thus lower spatial resolution. 2. Lower relative accuracy of geometry reconstruction.
Decrease flight altitude or Increase focal length	1. Decreases GSD and thus increases the spatial resolution. 2. Higher relative accuracy of geometry reconstruction.	1. A higher image rate is required. 2. Longer flight times and slower flight velocity. 3. Increased processing

		is required. 4. Increased problems with depth of field.

Table 4.8 List of advantages and disadvantages of increasing and decreasing the amount of ground recorded in each image. Therefore, finding the optimal balance between these two endpoints is necessary.

Although maintaining the GSD constant during each mapping mission is recommended to avoid inconsistent spatial resolution results, this is, in many cases, not possible due to the change in relief of the study area. In this case, it is recommended to carry our different flights where t*he higher GSD is twice as small compared to the lowest GSD* as per photogrammetry software package providers, including Pix4D® and Agisoft Metashape®.

$$GSD1 \leq 2 \times GSD2 \quad (3)$$

$$\frac{S(w\ or\ h) \times H1 \times 100}{Fr \times im(W\ or\ H)} < 2 \times \frac{S(w\ or\ h) \times H2 \times 100}{Fr \times im\ (W\ or\ H)} \quad (4)$$

Alternatively, it is also possible to fly at 80% of the desired GSD to compensate for changes in topography.

4.10 Shutter interval, motion blur, and image overlap

With the information presented above, it is now possible to calculate additional important flight parameters to ensure consistent results (Vollgger and Cruden, 2016).

Shutter interval

The shutter interval determines the relationship between the timestamp of two consecutive photos and the distance on the ground that is covered.

$$T_{interval} = \frac{imH \times GSD}{V_{horizontal}} \times \frac{100 \times OL_{forward}}{100} \quad (5)$$

Where $T_{interval}$ is the shutter interval in seconds, imH is the height of the digital image in pixels. $OL_{forward}$ is the percentage of desired image frontal overlap in the direction of flight (e.g., 80). $V_{horizontal}$ is the horizontal flight velocity in m/s.

The higher the shutter time interval, the fewer pictures are taken. Flying faster requires a shorter shutter interval while flying higher (increases GSD) requires a longer shutter interval.

Motion blur

As mentioned earlier, acquiring photographs during aerial motion induces motion blur into the images, which will profoundly affect the resulting quality of the 3D reconstruction. This effect can be quantified using the formula below.

$$MB = \frac{V_{horizontal} \times T_{shutter}}{GSD} \quad (6)$$

Where *MB* represents the blur in pixels and $T_{shutter}$ the shutter interval, also known as the exposure time in seconds, i*deally, the motion blur should be lower than the GSD*. If this is the case, no motion blur will be recorded as the time it takes to register the photograph is equal to or smaller than the time it takes for the aircraft to move one pixel forward.

If the following real-world scenario is taken where the horizontal velocity equates to 4 m/s, 30m flight altitude, $8.3x10^{-3}$ m GSD, and shutter time 1/320s, the resulting motion blur computes to 1.5 pix. This indicates that 0.5 pixels of effective motion blur is present in the image. This value can be lowered by reducing the exposure time or increasing the flight altitude (increasing the GSD).

Flight line spacing

Flight line and image spacing will determine the percentage of overlap between images and their direct neighbors. A higher overlap allows the SFM algorithm to identify a higher number of identical tie points across image clusters. A higher number of tie points results in more accurate 3D reconstructions. In a perfect world, overlap close to 90% would be ideal. However, this implies that a monumental amount of photograms will have to be acquired and processed, which in most scenarios is not worth the slight increase in reconstruction precision. Photogrammetry software packages recommend an image overlap of 60-85%.

$$S_{flightline} = GSD \times imW \times \frac{100 - OL_{side}}{100} \quad (7)$$

$S_{flightline}$ represents the spacing between parallel flight lines in meters, and OL_{side} is the percentage overlap between flight lines. This implies that for a GSD of $8.3x10^{-3}$ m at a flight altitude of 30m and an overlap of 80%, a line spacing is 9.1 m.

Note: This calculation holds for frontal overlap only.

4.11 Georeferencing

There are two distinct forms of accuracy in 3D structure from motion (SFM) based reconstructions: relative accuracy and absolute accuracy.

Relative accuracy

Inherently the quality of digital photogrammetry reconstruction depends on relative accuracy by how well (i) features between images can be matched and (ii) camera positions are calculated. Relative accuracy is not uniform throughout a reconstructed model. Factors such as overlap between images and the amount of detail in the images can significantly influence the magnitude of relative accuracy.

By default, most photogrammetry software packages state to achieve a relative accuracy of one to three times the GSD under ideal conditions. A flight at 30 m height and a GSD of 0.82 cm would result in a relative accuracy between 0.82 - 2.46 cm. The main question should be: what is the relative accuracy between two specific points on the reconstructed model? The impact of relative accuracy predominately depends on scale. A relative accuracy of 0.82 – 2.46 cm over a distance of 10 m has a much smaller effect than a relative accuracy over a distance of 10 cm; this implies that for quantitative geologic analysis, larger structures have a higher relative accuracy than that of smaller ones.

Absolute accuracy

Absolute accuracy is related to the real-world location of the topographic reconstruction (GPS). By default, photogrammetric models do not contain absolute accuracy and require information from either a GPS network or ground station to obtain it. Georeferencing a photogrammetric model can be done in the following two ways: (i) Geotagging photographs with GPS coordinates and (ii) matching GPS coordinates of a known feature on the ground, also known as *ground control points (GCPs)* to the same feature in the acquired imagery.

Ground control points and GNSS GPS

To extract quantitative data such as strike-dip, fault, and layer orientation from reconstructed 3D models, absolute positioning of the model on the globe is required. The reconstructed model's absolute accuracy depends on the GPS sensor's absolute accuracy, Table 4.9. The table below lists the absolute accuracy of all GPS sensors used in this study.

GPS receiver	Absolute accuracy (horizontal)
UAV	10 m
Nikon D5300	50-100 m
Trimble Catalyst (VRS, RTX)	1-4 cm
Emlid Reach RS (RTK), Correction base 30-40Km away (Rioja)	2m standalone, 30-40 cm with correction (~1 cm/Km).

Table 4.9 Absolute accuracies for all GPS sensors used in this study.

Although an accuracy of 10 m is acceptable for measuring geologic structures with dimensions in the hundreds of meters, it is not suitable for measuring smaller structures while maintaining good absolute accuracy.

It is for this reason that more accurate positioning is required. Although the exact working of GNSS GPS systems is outside this report's scope, two main GPS correction methods are available to achieve vertical and horizontal absolute accuracy within 1-5 cm. These include; (i) PPK (Post processing kinematic) and (ii) RTK (Real-time Kinematic). RTK requires a rover to receive real-time correction input from a base station with known absolute coordinates or a specialized satellite network. The distance from earthbound base stations will determine the absolute accuracy and will require significantly longer observation times if the base station is located far away. PPK allows for post-processing of the obtained data with correction data from a fixed, known base station to achieve the desired accuracy. PPK also depends on the distance from the base station; however, it does not require a long time-consuming data collection window. This study used two GNSS receivers to obtain centimeter accuracy, namely the Trimble Catalyst® and Emlid Reach RS+® as a backup.

Recording GPS coordinates from GCPs

To compile coordinates with high absolute accuracy, acquiring many GPS readings (RTK) through a fixed time window is necessary, followed by mathematically interpolating and averaging the obtained data. The final GPS measurement is very close to the actual real-world coordinates by interpolating many GPS readings. This is, however, not possible on a mobile airborne vehicle. For this reason, it was decided to use fixed ground control points (GCPs). The advantage is that ground control points are static, allowing long GPS reading intervals for maximum absolute accuracy.

GCPs are features positioned in the landscape that can be identified in the acquired UAV images. They can consist of a simple cross made with paint, a sheet with a symbol, even sharp street corners, or other characteristic native objects to the environment. The primary importance is that the feature should be identifiable to a single pixel on the image.
Although GCPs can be manually identified in the acquired images through photogrammetry packages, this is a very intensive and tedious task. Luckily, some photogrammetry packages, such as Agisoft Metashape, allow the automatic detection of specialized GCPs with computer vision algorithms.

The markers used in this study are 12-bit targets generated by Agisoft, figure 4.10. Each marker is different, which allows the software to distinguish and identify each unique marker. Each coded marker represents a number from the number one upward. The figure below displays the first marker (1) in the series.

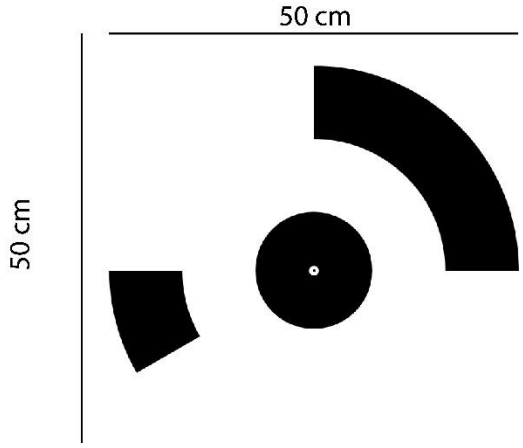

Figure 4.9 12-bit marker (GCP) generated by Agisoft Metashape. The marker is printed out onto an acrylic or metal surface and has a dimension of 50x50cm. Printing on a metal surface is beneficial to ensure the target stays stationary during windy days.

A plane must be generated with the obtained markers to orientate and georeference the reconstructed model correctly. To create a 3D plane, a minimum of three GCPs is required. Even though three markers are a minimum, adding more markers will increase the overall positioning accuracy of the model. In total 11× markers were used in this project. Agisoft automatically places the marker in the center of the 12-bit target, the black dot. If it cannot detect the black dot, it will try to average the central position of the white inner circle. However, if the GSD is larger than both of these two features, the software will not be able to detect the center of the target.
Additionally, if the GSD is too small, it won't be able to identify the center of the target; this is why the 12-bit GCPs were printed on aluminum and polycarbonate sheets with an outer dimension of 50x50 cm and a central inner circle of 1.5cm in diameter, which is twice the GCD for flights taken at 30 m altitude above the ground surface. This implies that a square matrix of 4x4 white pixels will be visible in the acquired images, allowing the computer vision algorithm to detect and place the marker in the center of this matrix.

GCP position acquisition
All GCPs are distributed evenly over the target surveying area to reduce the geolocation error margin, e.g. (Mallison and Wings, 2014). GCPs are placed at both altitude extremes in areas of high relief change. All GCPs are placed in areas without vertical or horizontal obstruction to ensure visibility across multiple images. An unobstructed view is vital because each GCP should be visible in at least three different photos to accurately place the marker within the coordinate system of the reconstructed model.

After laying out all targets on the ground, GCP GNSS acquisition is carried out. GCPs are not moved until the mapping is completed. The Trimble Catalyst antenna is mounted on a 2 m monopod with a sharp tip, attached to a mobile device, and placed vertically on the center of the target GCP. After initializing the GPS antenna, enough time is taken to ensure connectivity with a minimum of 11× satellites and an

absolute accuracy within 5 cm. A minimum of 20× measurement cycles are carried out per target to obtain a good distribution of values, which takes at least a minute or two per measured target.
All measurements are labeled by the target number and saved in Trimble's UAV ground control app. The points were then exported as a CSV file and imported into Agisoft Metashape as marker coordinates.

Coordinate Reference system
All measurements are collected in the WGS84 (EPSG::4326) coordinate system with the vertical height expressed as 'Height Above the Ellipsoid (HAE)'; see figure 4.11 below.

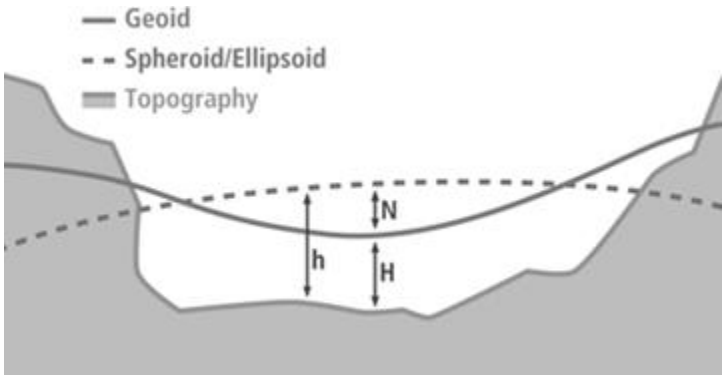

Figure 4.10 Schematic illustration of the relation between the Geoid, approximately equal to mean sea level (MSL), the topography of the surface, and the mathematical shape of the earth's surface known as the ellipsoid. Image from Arcgis documentation.

The following parameters are collected using the GNSS receiver:

1. Control point label
2. Latitude
3. Longitude
4. Height at ground (m)
5. Horizontal precision (HPrecision)
6. Vertical precision (VPrecision)

Limitations
It is important to note that although the intention is to distribute the GCPs uniformly across the survey area, it might not be possible to capture the GPS coordinates with a high enough accuracy for all GCPs due to relief obstruction preventing a good enough GPS lock with the satellites. Moreover, care must be taken to discard measurements with low accuracy.

5. Computation and Processing

Photogrammetric 3D reconstruction is a very computationally intensive task. The computational workload depends on (i) the number of images, (ii) image resolution, and (iii) the quality of the desired reconstruction. Computational workloads do not scale linearly due to image alignment, which interpolates across all identified data points. Mathematically, this leads to an exponential increase in computational power required.

For every SFM reconstruction step, different aspects of the computational resources are affected, Table 5.1.

	Image alignment	Dense cloud	Polygon Mesh	Texture	Orthophoto
Resource	CPU	GPU + VRAM	CPU + GPU + RAM	GPU	GPU
Requirement	High CPU clock speed and core count	High-end graphics card (high VRAM)	High clock speed	-	-

Table 5.1 Hardware specifications for each step of SFM reconstruction. Aligning and matching Images is primarily a CPU task where multiple images are matched across different logical cores. After alignment, bulk reconstruction is carried out across cores in the graphics card, and data is temporarily stored in VRAM within the GPU.

- Image alignment is heavily multithreaded (CPU), which results in a significant performance increase as the number of CPU threads increases.
- Dense cloud and depth map generation is very graphic processing unit (GPU) intensive and has a performance increase over CPU processing by a factor of 10×. Thus using a high-end card will result in significantly reduced processing times.
- Mesh generation impacts the CPU and GPU to approximately the same degree; having both a high-performance CPU + GPU will significantly reduce computation times. Furthermore, Mesh generation utilizes a significant amount of RAM compared to the other processing steps.
- Texture and Orthophoto generation are light tasks compared to the previous processing steps. However, they still utilize the GPU to a large degree to compile the UV maps.

Two strategies can be applied to reduce computation time: (i) A dedicated machine with very high-end hardware components. (ii) A computer cluster with multiple reasonably powerful individual processing nodes. Both cases have their advantages and disadvantages. For instance, a dedicated computation machine allows for easier processing, maintenance, and troubleshooting. The main disadvantage of this approach is that computation components become exponentially more expensive after transitioning from consumer to enterprise hardware at higher workloads.

The advantage of a network computation cluster is that multiple low-end hardware devices can be linked together to form a powerful computation cluster that can easily outpace a dedicated machine. This approach is more cost-effective because consumer-grade devices are widespread and, in many cases, already in possession of the team members carrying out the research, removing the necessity to acquire any hardware. However, the disadvantage of this approach is that it is significantly more challenging to set up due to the necessity of both networking and network data storage.

In this study, the network approach was used. To configure a network processing cluster, the following components are necessary:

- **A central server** also referred to as a controller node. This node controls all the processing (worker) nodes. It splits the main task into smaller batches and sends them to each processing node. Each node receives a unique batch. This process is executed through a terminal on the controller node.
- The p**rocessing nodes** run the computation tasks and only require a command line executable that runs in the background.

- The **router** links all devices into one LAN, allowing for rapid communication over TCP between each of the system's individual components.
- **Network-attached** storage is required so that each computer attached to the cluster has live read and write access to the model in reconstruction.
- A **client machine** connects to the server through TCP to manage the project through the standard Graphical User Interface (GUI) interface;

Figure 5.1 below illustrates a schematic blueprint of such a computation cluster.

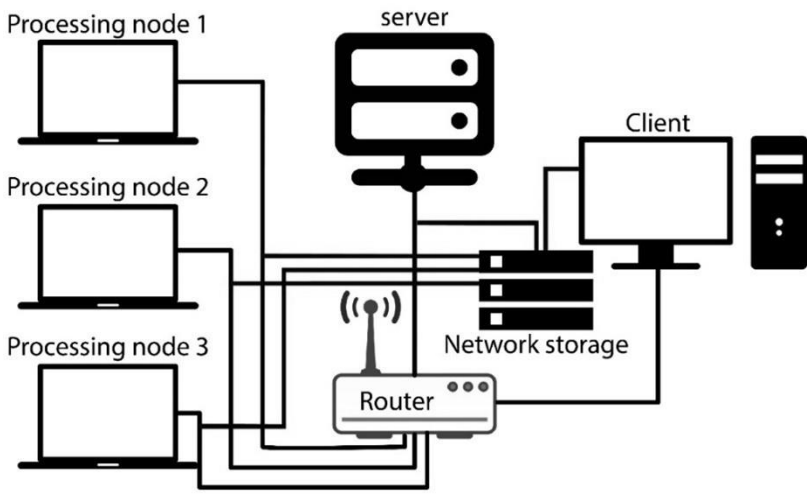

Figure 5.1 Schematic diagram of the computation cluster used for photogrammetric reconstruction. The system consists of 4x different components: (1) Server, (2) processing nodes, (3) network link (e.g., router), and (4) client.

The following computing units are used in this study, Table 5.2:

Device type	CPU	GPU	RAM
DELL XPS 15 (compute)	i7-770HQ (8 threads)	GeForce® GTX 1080 Mini ITX (8GB VRAM) – eGPU Intel HD graphics 630 GeForce® GTX 1050 (2GB VRAM)	32GB
Custom desktop (compute)	i7-6700K (8 threads)	GeForce® GTX 1080 (6GB)	32GB
Toshiba Satellite (server)	i3 3110M	Intel HD graphics 4000 (1GB VRAM)	8GB

Table 5.2 The table illustrates the different computing units used in this study. The compute units are nodes with higher available resources, while the server node solely orchestrates the cluster, requiring fewer resources.

As can be observed in the table above, the most powerful machines are used as computing units, while the less powerful machine is used as a server as it does not carry out any reconstructive tasks. The client computer running the GUI can be a separate machine or the server acting as both the distributor of workloads and entry point to the cluster. Out-of-core processing and model tilling were enabled to reduce RAM load and facilitate model visualization and post-SfM handling in VRGS.
Combined, the two compute nodes have 64GB of RAM and 16 threads boosting up to 3.80GHz, which is

a significantly higher clock speed compared to an Intel Xeon at the comparable core count. Furthermore, this setup contains 4× GPUs with a combined VRAM of 15GB and 5248 CUDA cores. These specs are equivalent to a very high-end dedicated computing unit. Cluster processing is highly scalable to tens of nodes.

5.1 Data Sources and Processing

Several data sources can be combined to create a coherent mapping strategy that blends traditional techniques, field data, and observations with modern remote sensing techniques such as UAV imagery, figure 5.2. Combining digital and analog measurements can serve as a valuable data anchor to calibrate the geologic survey.

Analog compass measurements of known target areas can also serve as a good calibration tool for digital strike-dip measurements, including the ability to calculate read-world accuracy error margins. Detailed field photographs and measurements are used to calculate and calibrate digital model scales to real-world dimensions.

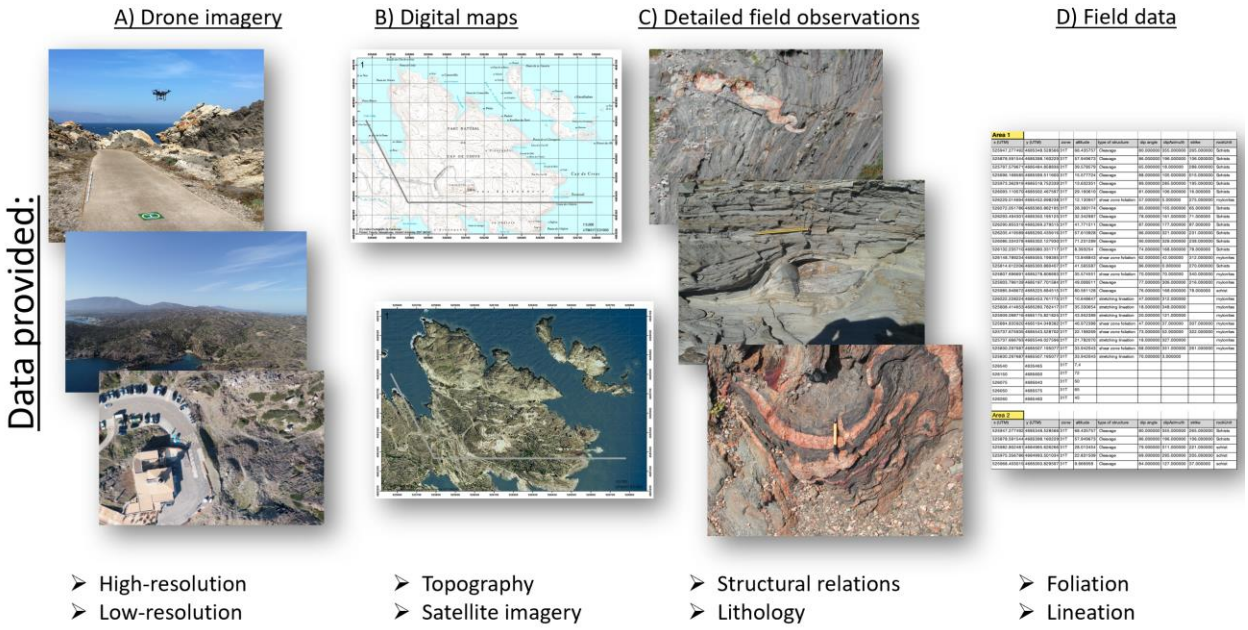

Figure 5.2 Different data sources ranging from analog field observations, measurements, and modern techniques, including drone imagery and digital 3D maps, can be combined to create a state-of-the-art data collection catalog for accurate Geologic fieldwork. Diagram compiled by Dr. Richard Wessels, Utrecht University.

The output data from digital reconstructions include; (i) Orthophotos (Detailed and Overview), (ii) detailed digital elevation model (DEM), and (iii) tiled high-resolution 3D models, figure 5.3. The data is exported from Metashape® and organized in their respective folder structures. Each digital dataset is reviewed after export for the correct GNSS reference frame, scale, and absolute accuracy before proceeding to qualitative and quantitative analysis. 3D tiled models are imported into VRGS for structural strike-dip and other displacement data measurements. 2D orthophotos and DEMs are imported into QGIS for 2D – XY strain and displacement analysis. QGIS is also used for qualitative digital field observations, which are compared to analog field observations and photographs to obtain a better

structural sense of the geologic outcrops. Finally, the orthophotos of relevant granodiorite outcrops are imported into GeoShear 2.0(*) for R-f 2D strain analysis.

(*) *Geoshear is a desktop application to aid structural geology research and teaching. It models shearing deformations, providing both an interactive visual interface and exportable quantitative data. Geoshear is coded in Java. It is a collaborative project between Professor Paul Karabinos of the Geology department and Chris Warren, Senior Academic Application Developer in OIT, created as a part of NSF grant 0942313 – "Visualizing Strain in Rocks with Interactive Computer Programs", Williams College.*

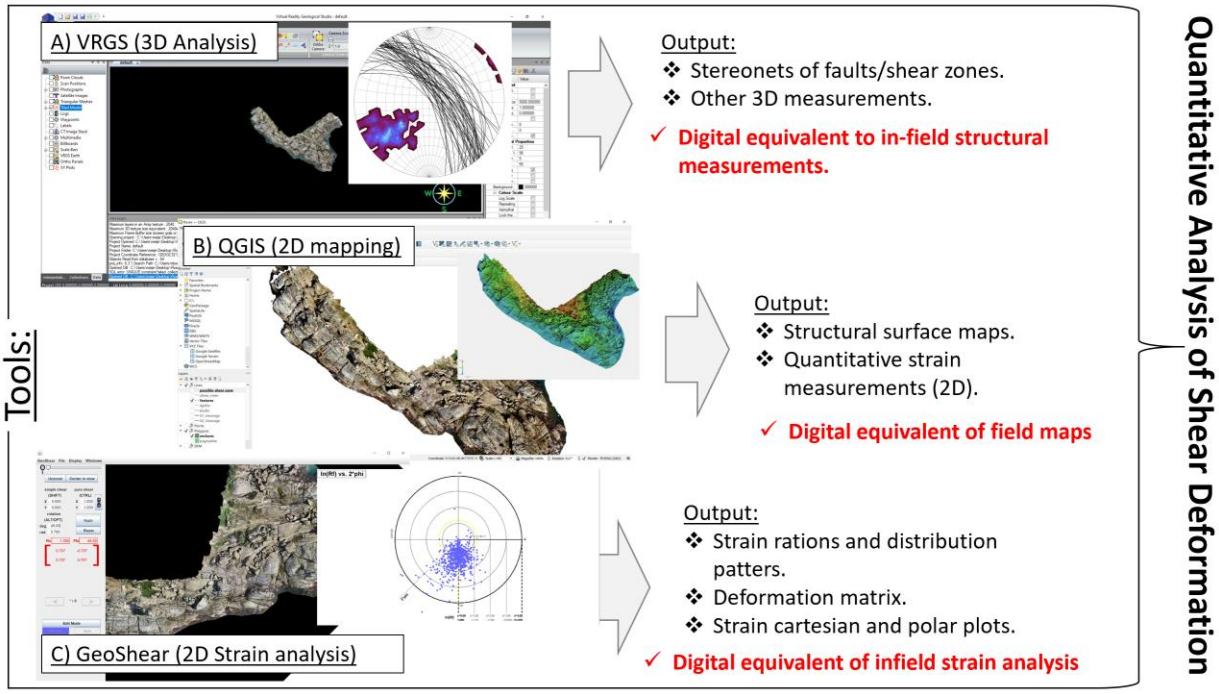

Figure 5.3 Overview of the deployed toolsets for quantitative data analysis. A) VRGS for 3D structural strike-dip measurements. B) QGIS for 2D geospatial measurements and observations. C) GeoShear for 2D strain analysis using the Rf-Phi method. Diagram compiled by Dr. Richard Wessels, Utrecht University.

Each toolset exports different types of data, (i) VRGS exports accurate strike-dip measurements, including the ability to export structural Stereonets with structural poles. Additionally, VRGS can export 3D polygon maps of structural features, including layers, foliation, and faults. (ii) QGIS enables the export of shapefiles that include many linear features and measurements: shear zone and intrusion displacement, cleavage, and fold strike orientations. QGIS enables structural features to be mapped and overlaid on top of a base orthophoto, (iii) GeoShear exports strain analysis metrics, including strain ratio matrix, cartesian and polar plots. The above outputs can be combined to generate an accurate quantitative picture of the study area.

6. Quantitative Analysis of the Late Variscan Roses Granodiorite

In the following sections, the results are presented for the Roses Granodiorite case study covering the use of remote sensing for quantitative analysis of deformation. The Roses Granodiorite Study area is located to the SW of the Cap de Creus peninsula (figure 6.1).

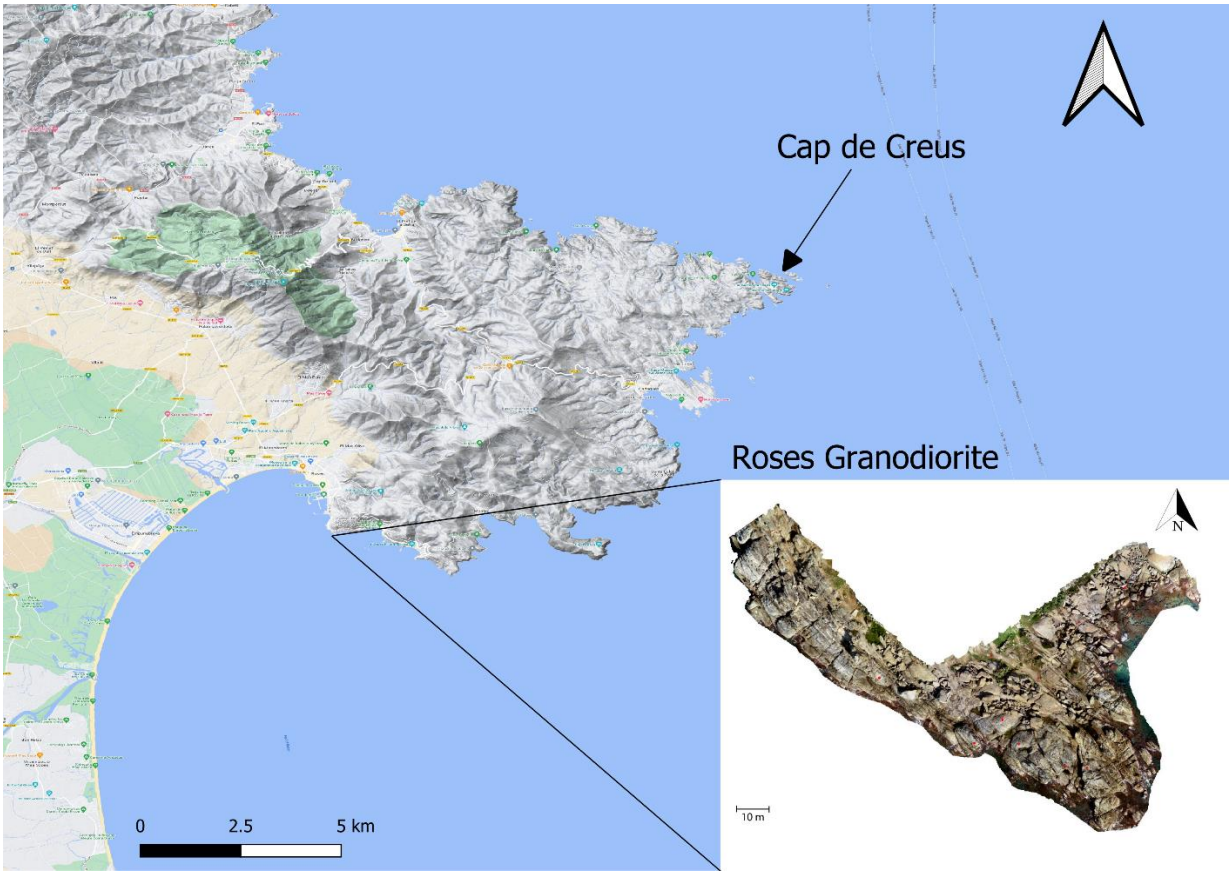

Figure 6.1 Large Scale map indicating the Roses study area in relation to Cap de Creus in the North. See large scale Aerial Panorama in figure 6.2 below.

Figure 6.2 Aerial panorama of the late Variscan Roses granodiorite intrusion 13 km South of Cap de Creus. The area covered is approximately 0.716 Ha. The red dots represent the location of the GPS GCPs used to georeferenced the digital model. Multiple flights were executed at low altitudes and speeds to obtain the highest-resolution imagery possible.

6.1 Data Collection and Processing

Before the aerial survey, a total of 10 GCPs were placed uniformly across the Roses granodiorite outcrop. After placement of the control points, their GPS positions are recorded within reasonable horizontal and vertical absolute error margins (see table below). A 5 m scalebar is placed in the center of the scene to scale the model in post-processing to real-world dimensions. A total of 4 flights are carried out, of which 3 are 3D flights (off-nadir) at 10 m altitude, and 1 is a 2D (nadir) overview flight at 20m, figure 6.3.

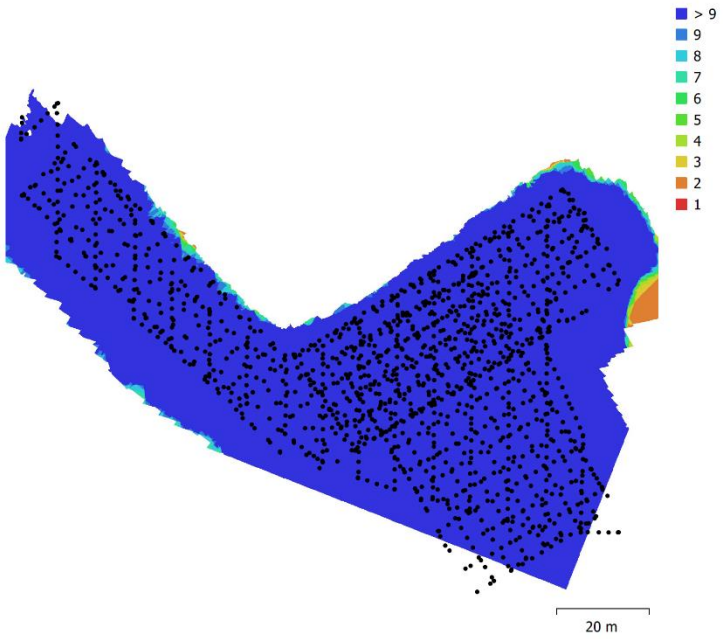

Figure 6.3 Projection illustrating camera locations and overlap. Enough overlap between flights is maintained to produce a consistent coverage pattern. Each physical point on the outcrop records at least nine different images. Only the edges have a lower overlap, which are clipped during model generation.

Agisoft Metashape® is used to produce a high-resolution orthophoto (3.31 mm/pix), DEM (8.34 mm/pix), and tiled 3D model (7 levels, 3.31 mm/pix), Table 6.1. The overview 2D flight is excluded from processing for orthophoto reconstruction to retain a uniform ground sampling distance. The geometrically corrected orthophoto and DEM are exported and processed in QGIS and GeoShear for Rf-Phi analyses. The tiled 3D model is exported and processed in VRGS®.

Number of Aerial Images	1,597
Flight Altitude (3D)	12.7 m
Flight Altitude (2D)	20.0 m
Ground Sampling Distance (GSD)	3.31 mm/pix
Coverage Area	7.16e+03 m²
Tie Points	588,365
Projections	3,397,252
Reprojection Error	0.436 pix
Total GPS Error	23.1013 cm
Scalebar Error	7.48e-04 m

Table 6.1 Data processing parameters and errors.

6.2 Roses Granodiorite Geologic Setting

The Roses granodiorite, located on the southern belt of the Cap de Creus peninsula, forms the easternmost outcrop of the Paleozoic basement in the Pyrenean Axil Zone. Structures in the Southern belt display geometries associated with isotropic rocks with XY strain planes closely related to heterogeneous simple shear (Ramsay and Graham, 1970; Ramsay, 1980; Simpson, C. and Sistach, 1982; Simpson, Carol, 1983). The intrusion, elongated in an NW – SE direction, is interpreted to be a relic of a complex polyphase tectonic deformation history subjected to progressive deformation during retrograde conditions associated with D_3, encapsulating both the Variscan and potentially Alpine orogeny's (Druguet, Elena et al., 2014).

The granitoid pluton was emplaced relatively late in the Variscan history, intruding during regional D_2 and further deforming during the late Variscan retrograde shearing event D_3. The pluton intruded into the shallow upper sequence composed of low-grade Cambro – Ordovician metasedimentary rocks, developing narrow contact aureole of spotted phyllites and hornfelses (Carreras, Jordi and Losantos, 1982). The distinct structures, metasediment folds, and shear zones observed in the pluton possibly reflect how lithological units with different rheological properties respond differently to deformation (Carreras, Jordi et al., 2004). In the last few decades, various detailed studies have been carried out of the Roses granodiorites to reconstruct its deformation history, timing, and significance in the larger Variscan cycle. Whereas all previous studies are based on analog field measurements, this study is carried out with the help of digital remote sensing and geographic information systems (GIS) to complement existing field observations and measurements and potentially provide additional constraints and insight into the emplacement of the Roses granodiorite. The abundance of micro-quartz-dioritic enclaves permits shape analysis to characterize the high-temperature solid-state fabrics and superimposed effect of later mylonitization under retrograde greenschist facies. Additionally, rotation, folding, and thinning of aplite dykes by shearing and related offset enables shear strain determination across the shear zone (Carreras, Jordi et al., 2004).

6.2.1 Granodiorite composition

The composition of the intruded body is of relatively homogeneous calc-alkaline affinity that varies between granodiorite and tonalite. The calc-alkaline composition suggests a mantle-crust mixed source with different degrees of additional crustal contamination closely associated with continental arc magmatism (Pereira et al., 2014). Moreover, local interactions between the intrusive magmas and partial melting of the schist country rock at the body's boundary induced migmatization and emplacement of shallow xenoliths.

6.2.2 Mafic fabric and diorite enclaves

The granodiorite is locally rich in elongated micro-quartz mafic (dioritic) enclaves, which, together with metasedimentary xenoliths and the preferred orientation of plagioclase and other mafic minerals, define the high-temperature homogeneous and syn-magmatic deformation fabric developed during D_2 and prior to D_3, figure 6.4 (Carreras, Jordi et al., 2004; Druguet, Elena et al., 2014).

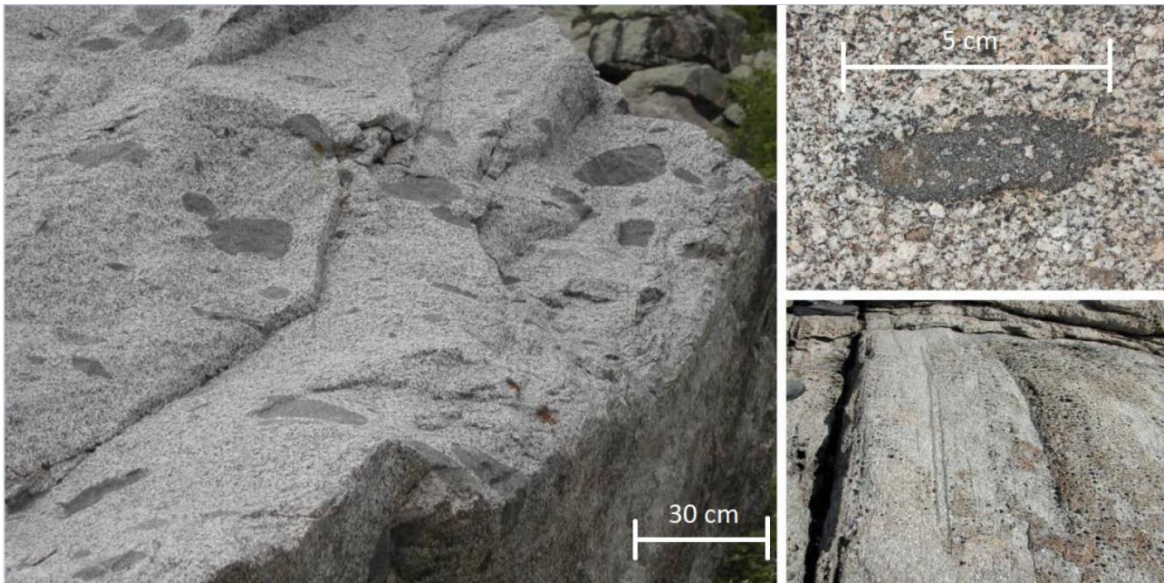

Figure 6.4 Field photographs of the Roses granodiorite mafic enclaves. The enclaves have variable shapes and orientations. Outside high-strain zones, enclaves have a slightly convex profile. In contrast, enclaves in shear zones are stretched out and flattened, indicating that deformation took place under a ductile regime.

The Granodiorite Mylonitic foliation trends E – W to NW – SE in a curved disposition and postdates the regional foliation in the enclosing metasediments. The Mylonitic foliation developed during D_2 represents the oldest fabric of the Roses pluton (Carreras, Jordi et al., 2004). Enclave distribution is inhomogeneous; most enclaves are predominately flattened with a preferred orientation sub-parallel to the magmatic foliation (Carreras, Jordi et al., 2004).

6.3 Diorite Enclaves - Digital Strain Quantification

Quantitative strain analysis is performed using the Rf/Φ technique (Lisle, 1985) for the enclave populations visible in the obtained orthorectified aerial imagery by measuring the shape ratios and orientation with a Java computer program named GeoShear 2.0 (Williams College, 2010) (Karabinos and Warren, 2010) for enclave populations across the entire outcrop. By measuring the shape ratio and orientation of the enclaves, one can infer information regarding the finite strain and constrain the deformation history (figure 6.5). To reliably carry out the Rf/Φ technique, it assumed that; (i) enough markers are used, (ii) strain is homogeneous, (iii) markers are passive, (iv) their initial shape and orientations are known or assumed which can be approximated by an ellipsoid (Wheeler, 1986). The extent to which enclaves are reliable as strain markers remains uncertain due to the existence of variables that can be related to deformation and magmatic processes (Paterson et al., 2004). Among these variables, the most critical include: (i) Adjacent enclaves may form at different times and have been initially non-spherical, potentially reflecting different snapshots within a continuous deformation regime; (ii) the final shape and orientations of enclaves are a function of the initial shape and viscosity/rheology contrast evolution within the magma; (iii) the deformation path may include rigid rotation and internal strain caused by magma flow; (iv) the earliest deformation during its magmatic history under non-solid-state conditions might not have been recorded. It is therefore advisable to couple enclave analysis with other data, including igneous layering, dyke mineral fabrics, and alignment thereof. Although further study and micro-analysis of enclaves and the surrounding fabric are required to infer the effect of magmatic processing on enclave evolution, many enclaves are used to characterize

the population of markers statistically. We must thus interpret the obtained results with caution. In summary, the predominant uncertainties of using mafic enclaves for quantifying finite strain are twofold: (i) uncertainty regarding the timing of emplacement and the viscosity ratio between the host magma and the enclave; (ii) whether enclave deformation can be attributed to magmatic or tectonic processes and to which degree the present-day shape of the enclaves records these.

Metasedimentary xenoliths, dismembered or otherwise unusual shapes of enclaves to the main distribution, have been excluded from the analysis to avoid erroneous results.

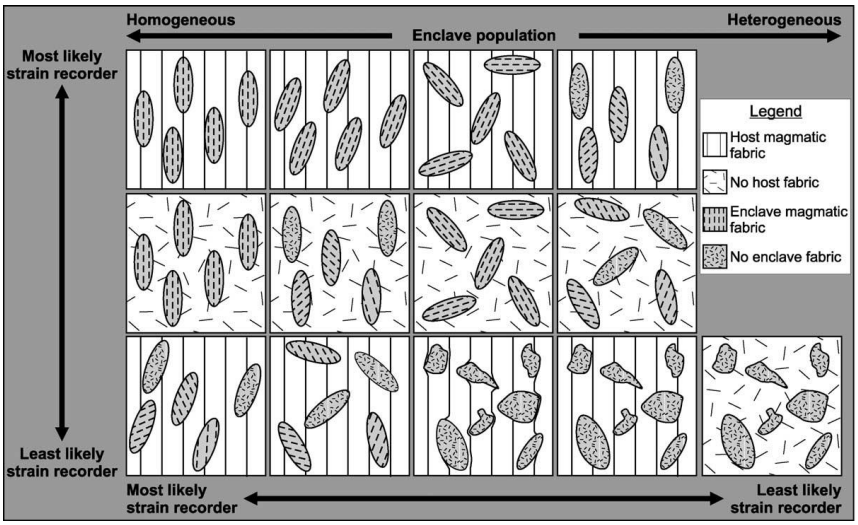

Figure 6.5. Cartoon showing the range of possible relationships between enclave shapes, internal magmatic mineral fabrics, and magmatic mineral fabrics in the host granite. The closer the enclave fabric is to the host magmatic fabric, the higher the probability that the enclaves are passive markers and strain recorders (Paterson et al., 2004).

6.4 Results: Rf/Φ Method

In total, 1017 enclaves are measured using the Rf/Φ technique with GeoShear 2.0 (Williams College, 2010), figure 6.6, and formulas 8/9 below. Only symmetrical, sub-horizontal, and enclaves with consistent shapes and orientations are used to avoid erroneous results (Carreras, Jordi et al., 2004). The markers are measured in 2D across the XZ plane. Measurements are done across the entire surface area of the Roses Granodiorite including within shear zones, figure 6.8. The most common shapes of enclaves encountered are recorded and plotted in figure 6.7. As can be seen in the figure, although enclaves act as passive strain markers in most cases, this is not always the case.

Figure 6.6. The georeferenced orthophoto is loaded into GeoShear 2.0 where enclaves are manually projected on top of the observed enclaves on the orthophoto. This process is repeated over the entire Roses granodiorite outcrop. Scalebar color sections are 1m.

Moreover, enclaves are cross-cut by aplite intrusions and small-scale faults. Non-coaxial deformation of enclaves occurs predominately near small-scale shear zones.

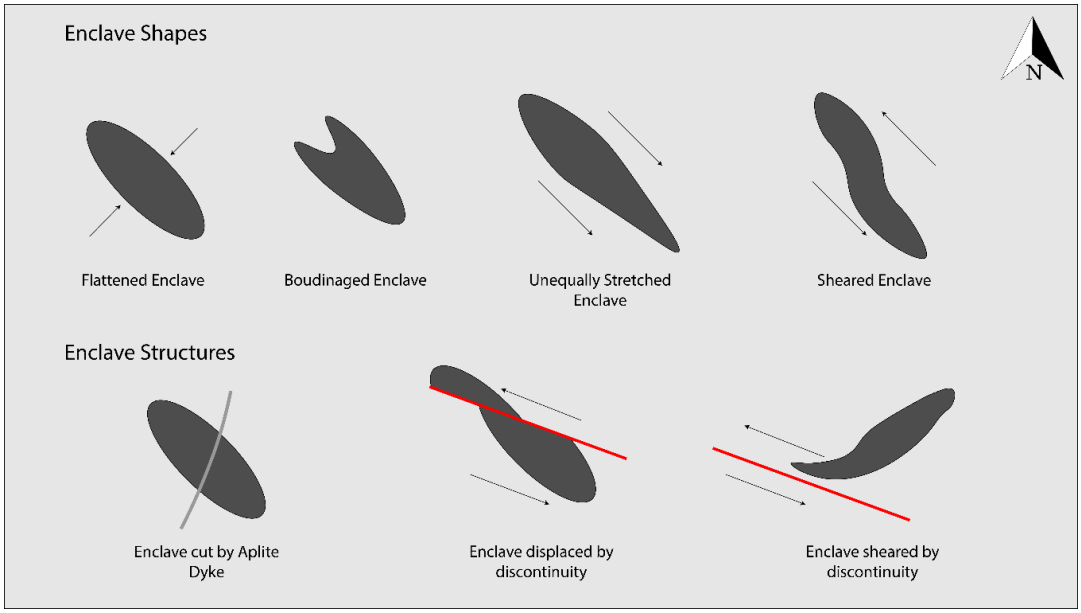

Figure 6.7 Most common enclave shapes encountered during the enclave analysis of the Roses granodiorite. As seen from the different forms, not all enclaves act as passive strain markers, resulting in various shape changes. Enclaves are subsequently cross-cut and deformed by later structures such as aplite dykes and shear zones.

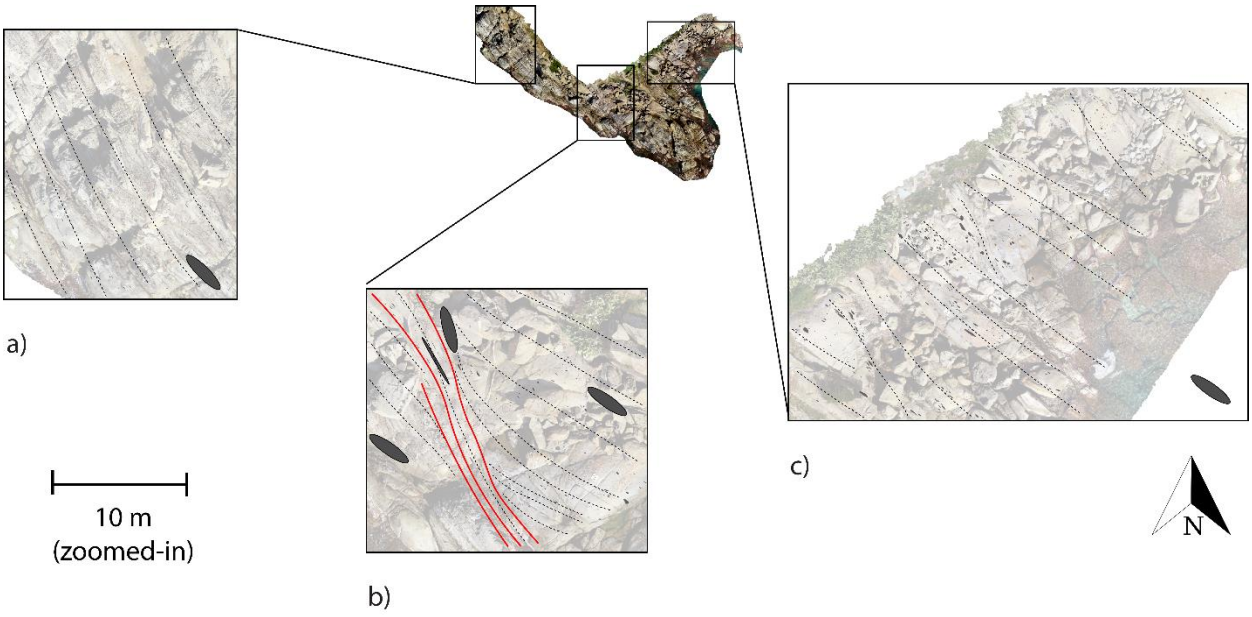

Figure 6.8 Map overview of diorite enclaves on the granodiorite's western, central and eastern flanks. (a) and (c) have similar enclave orientations, whereas enclaves in (b) rotate towards the late shear zones. The mean strain axial ratio (RS) is shown with an ellipse showing the mean orientation and shape of the strain ellipse.

Pre-dyke finite strains obtained from two-dimensional analysis of enclaves in sections close to the XZ plane are obtained (figure 6.9). The ellipticity (R_f) is shown with an ellipse showing the mean orientation (Φ) and shape of the strain ellipse, figure 6.8 (e.g. (Carreras, Jordi et al., 2004).

6.4.1 Cumulative results (Pre & Post Dyke)

The analysis displayed in figure 6.9 illustrates that the bulk of the axial ratios from the data dispersion ranges from R_f = 1.5 to 5.8, with an average of R_f = 3.4 outside of shear zone strain boundaries (vertical yellow line in figure 6.9) and increases to R_f = 10 to 50 within shear zones as illustrated in the data points to the right of the plot that increases $R_{f\,max}$ while maintaining $R_{f\,min}$ and thus increases the axial ratio. The orientation Φ is consistent across most enclaves at -30° to -60° with an average value of -45° (NW - SE) indicated by the yellow horizontal line in figure 6.9, b. Enclaves with the highest Φ fluctuation and axial ratios can be found leading up towards and within shear zones and plot outside of the main data distribution, figure 6.9, a. Markers close to these discontinuities display deflection and rotation towards the shear zone principal plane of stress, which can also be observed through the convergence of 2* Φ values left and right of ln (Rf) = 1 (figure 6.9, a). The initial enclave ratio R_i was estimated at between 1.5 to 1.9, and the strain ratio after deformation R_s at 2.9 to 3.3, yellow vertical line in Figure 6.9, b.

$$R_s = \sqrt{R_{f\,max} * R_{f\,min}} \quad (8)$$

$$R_i = \sqrt{\frac{R_{f\,max}}{R_{f\,min}}} \quad (9)$$

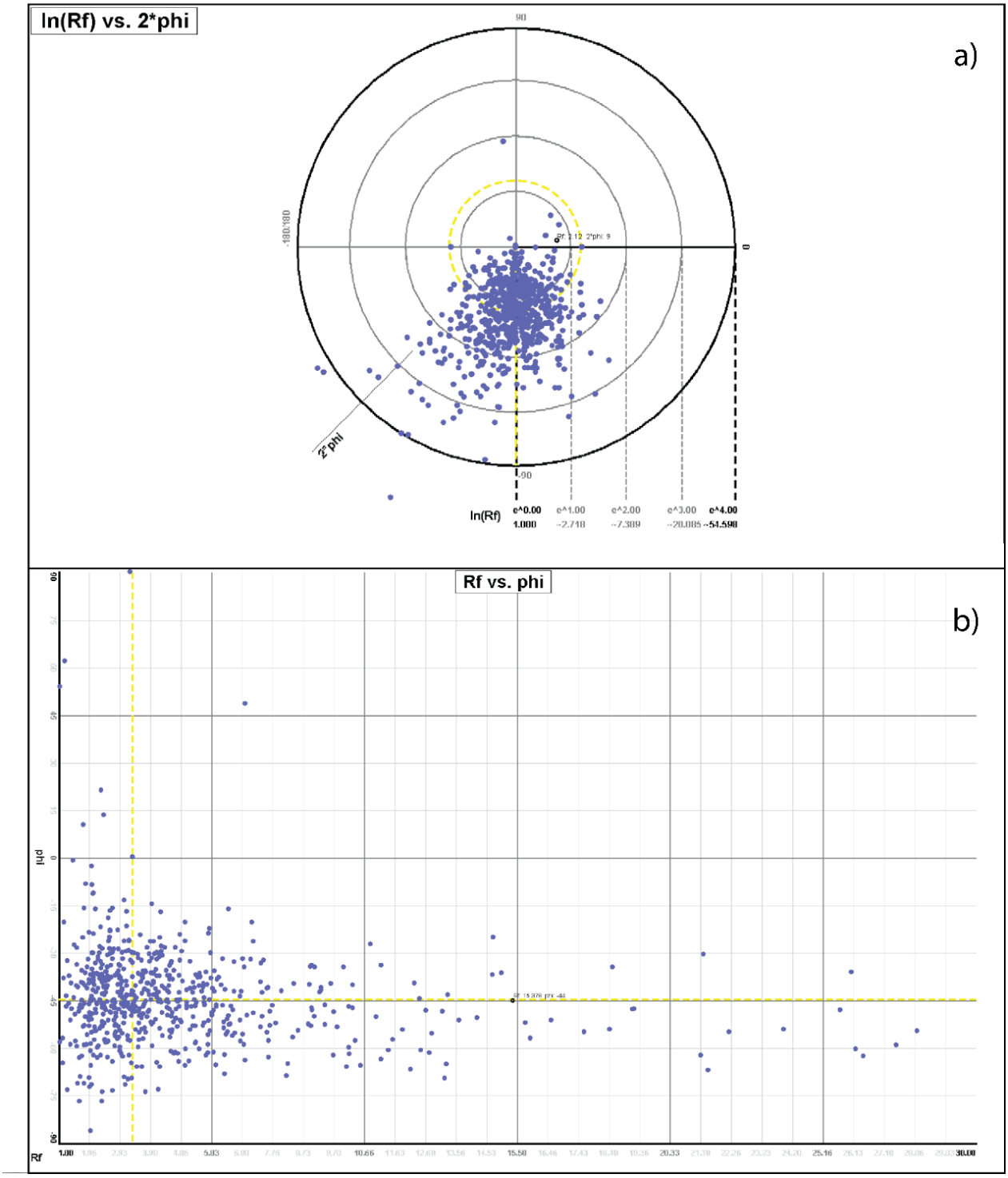

Figure 6.9 (a) Polar plot ln(Rf) – 2* Φ and (b) Cartesian Rf – Φ analysis of 1017 enclaves of the Roses granodiorite. Only the most symmetrical enclaves were used for this analysis. Average Φ and Rf values are indicated with the yellow lines. Data is scaled horizontally for adequate visualization.

Undeforming the enclaves in GeoShear provides the following deformation matrix listed below, figure 6.10. The matrix represents a general shear deformation style dominated by pure shear and a minor inhomogeneous simple shear component.

$$\begin{bmatrix} 0.449 & -0.427 \\ 1.140 & 1.140 \end{bmatrix}$$

Diagonal deformation matrix of the Roses granodiorite diorite enclaves.

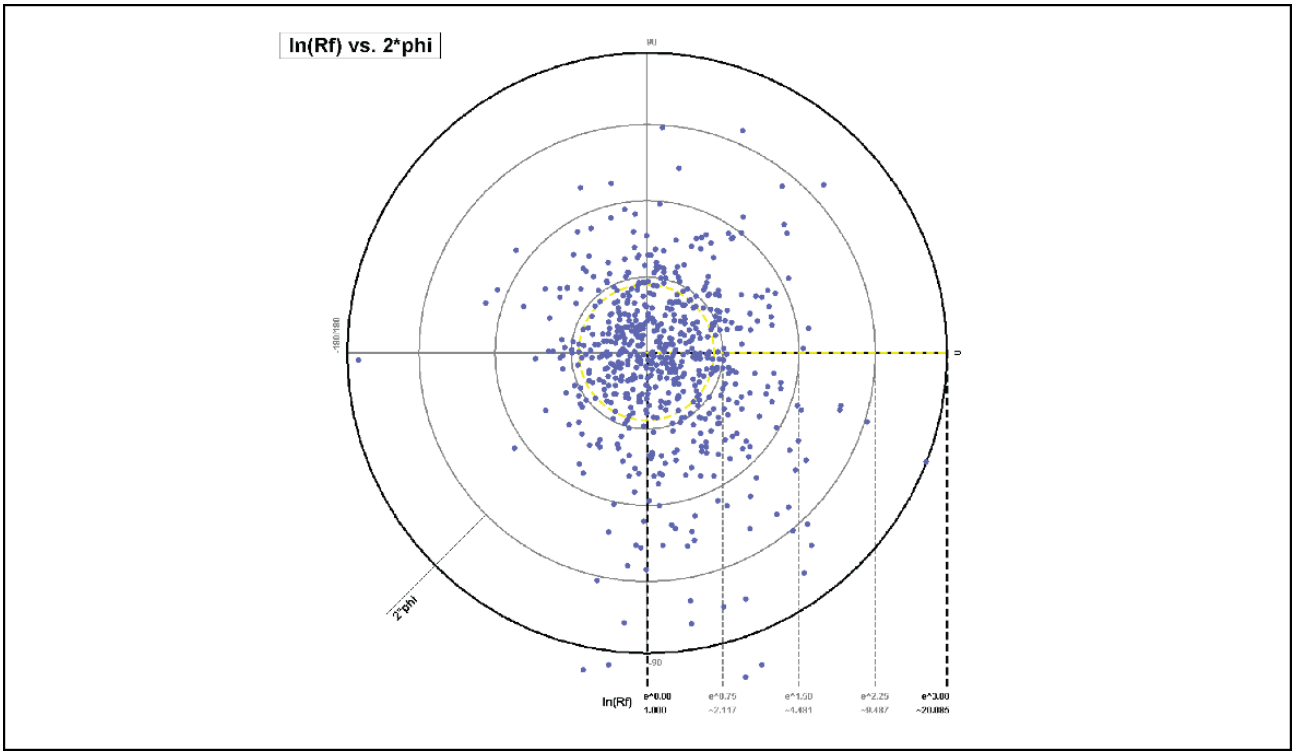

Figure 6.10 Back-rotated polar ln(Rf) – 2*Φ plot of undeformed enclaves of the Roses granodiorite. The data clearly illustrates a consistent trend in long-axis orientation and distribution in the undeformed samples.

A quick examination of the undeformed enclaves shows that the values of R_i are widely distributed. Bulk quantitative results from different localities and visual inspection of enclaves indicated a slight Inhomogeneous strain component of low intensity across the entire stock. Examples of this are the sheared enclaves which demonstrate a σ-porphyroblast type structure. Strain localization in a cooling magma under compression-dominated transpression is not uncommon. It is, however, still uncertain if these features are attributed to magmatic flow or regional deformation stresses. Notwithstanding these limitations, the strain measurements using enclave shapes provide a marker to estimate finite strain gradients undergone by the granodiorite intrusion.

6.4.2 Pre-dyke results

In order to constrain deformation to the pre-dyke phase a filter was applied to only select enclaves where undeformed dykes provide evidence for the absence of post-dyke strains (Carreras, Jordi et al., 2004). The visual strain method was applied from (Karabinos and Warren, 2010) to determine the inverse strain ellipse by first rotating Φ to 0° followed by pure shear to orientate the points on the polar plots to create a radial distribution of points centered at the origin to simulate an initially random

distribution of long axis orientations. The axial ratios of the strain ellipse are estimated at RS = 1.4 for the pre-dyke deformation phase through pure shear deformation.

6.5 Aplite Dykes – Digital Strain Quantification

Aplitic (leucogranite) dykes and veins are abundant in the Roses intrusive body and represent the last differentiation of the pluton, figure 6.11. Emplaced as over-pressured residual leucogranite melts during the final cooling stages of late D_2, prior to the final D_3 phase. The emplacement characterizes a change in rheology from strictly ductile to ductile-brittle conditions where fracturing becomes possible (Druguet, Elena et al., 2014). The Aplite dykes are present in swarms variable in size from a few millimeters to tens of centimeters in width and tens of meters in length.

Figure 6.11 The Roses Aplite Dykes intrude into the granodiorite and cross-cut the existing foliation and the pre-existing aplite dykes. Some dykes are folded into tight asymmetrical folds.

Aplite's cross-cut the internal granodiorite magmatic foliation and elongated enclaves at a high angle (70-90°) while being locally subsequently folded with axial planes parallel to the magmatic fabric, suggesting solid-state deformation with a similar orientation before and after dyke emplacement (Stout et al., 1986). Dykes are presumed to intrude along tension fractures related to the same progressive and rotating stress field that produced the magmatic foliation (Carreras, Jordi et al., 2004).

6.6 Results: Digital Strain Quantification of Aplite Dykes

The compiled georeferenced aerial orthophoto from Metashape® was used In QGIS to manually trace the aplite dyke intrusions and the recognizable shear zones (figure 6.14 & 6.15). Figure 6.14 illustrates that most aplite dykes trend either NW – SE with some rotation throughout the outcrop and oblique conjugate sets present. The width of dykes is highly variable, with the widest intrusions located on the edge of the western flank. Dioritic enclaves associated with D_2 and Aplite dykes are rotated, deformed, and displaced by younger D_3 NW – SE oriented anastomosing and steeply dipping shear zones developing a mylonitic foliation (S_3), figures 6.11, 6.13 and 6.14. Grain size reduction in the mylonitic shear zones is apparent compared to the less deformed areas of the granodiorite (figure 6.11). Aplites are deformed by both sinistral and dextral shear zones.

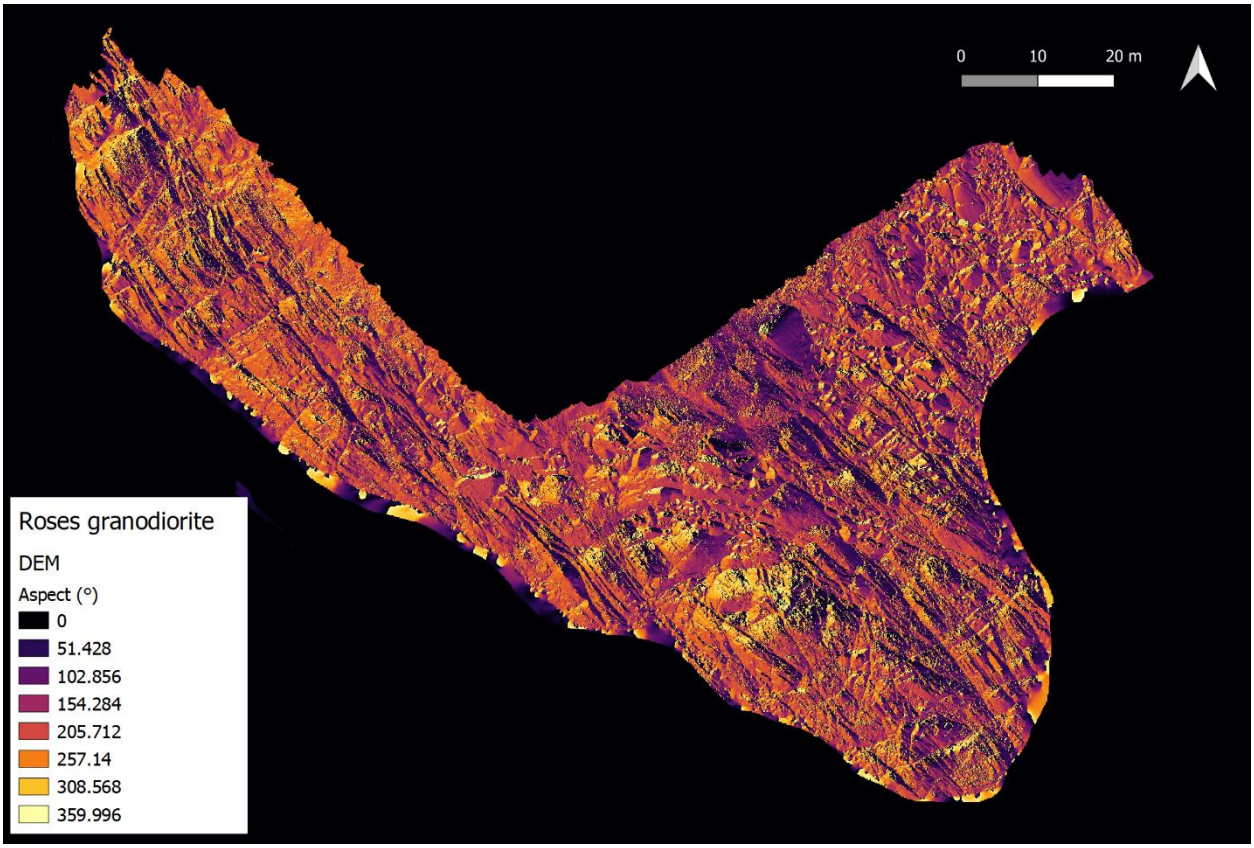

Figure 6.12 Aspect DEM (dip direction) rendered with QGIS illustrating the dip direction of planes within the Roses Granodiorite outcrop. As can be observed most steep dipping planes have an orientation of between 20 and 67 degrees (NE).

Figure 6.13 Roses granodiorite photographs illustrating small-scale shear zones and their respective displacement of Aplite dykes (left) and mylonite formation (right). Grain size reduction can be observed at the shear zone boundaries.

Although shear zones cut most aplites at a high angle (figure 6.15), some aplites run parallel to the younger shear zones.

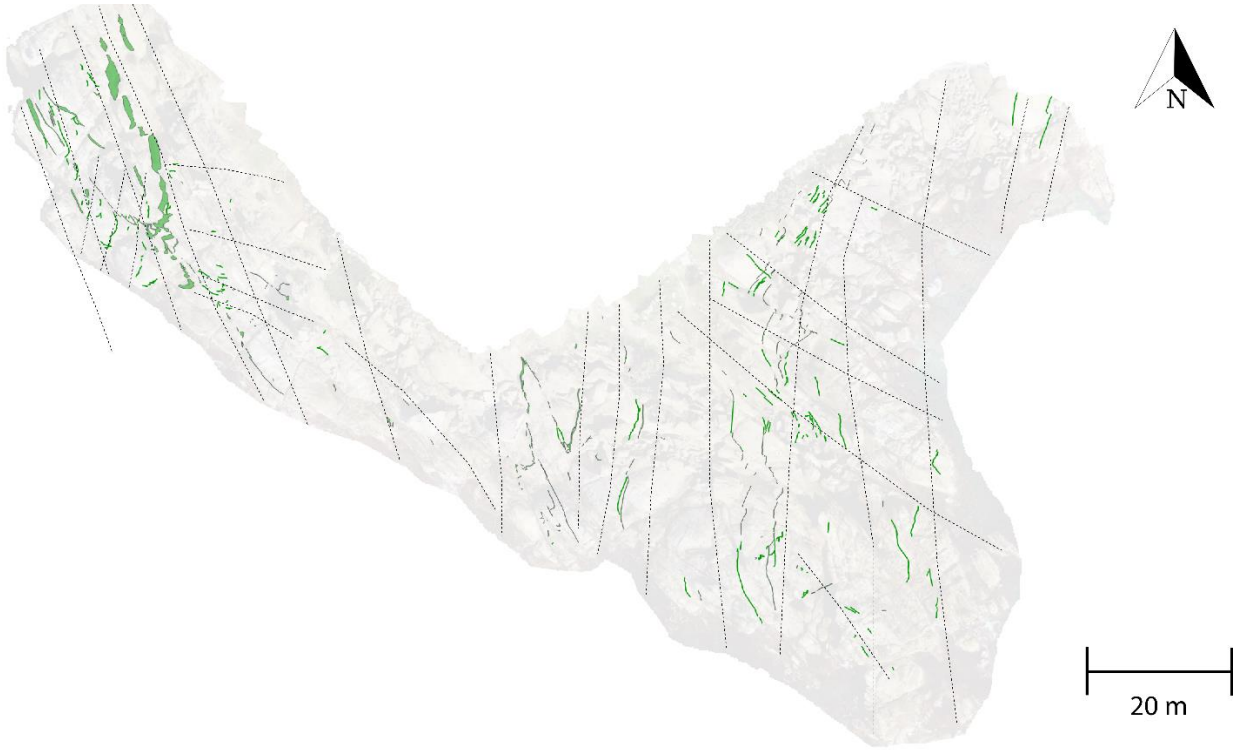

Figure 6.14 QGIS digital scan of aplite dykes (green lines) within the Roses granodiorite. The dashed line indicates the preferential strike of the instruded aplites. Although most dykes trend NW – SE, conjugate sets are locally present. Aplite dykes are displaced, deformed, and rotated by younger shear zones in both sinistral and dextral directions. The thickest intrusions are located on the western flank of the granodiorite.

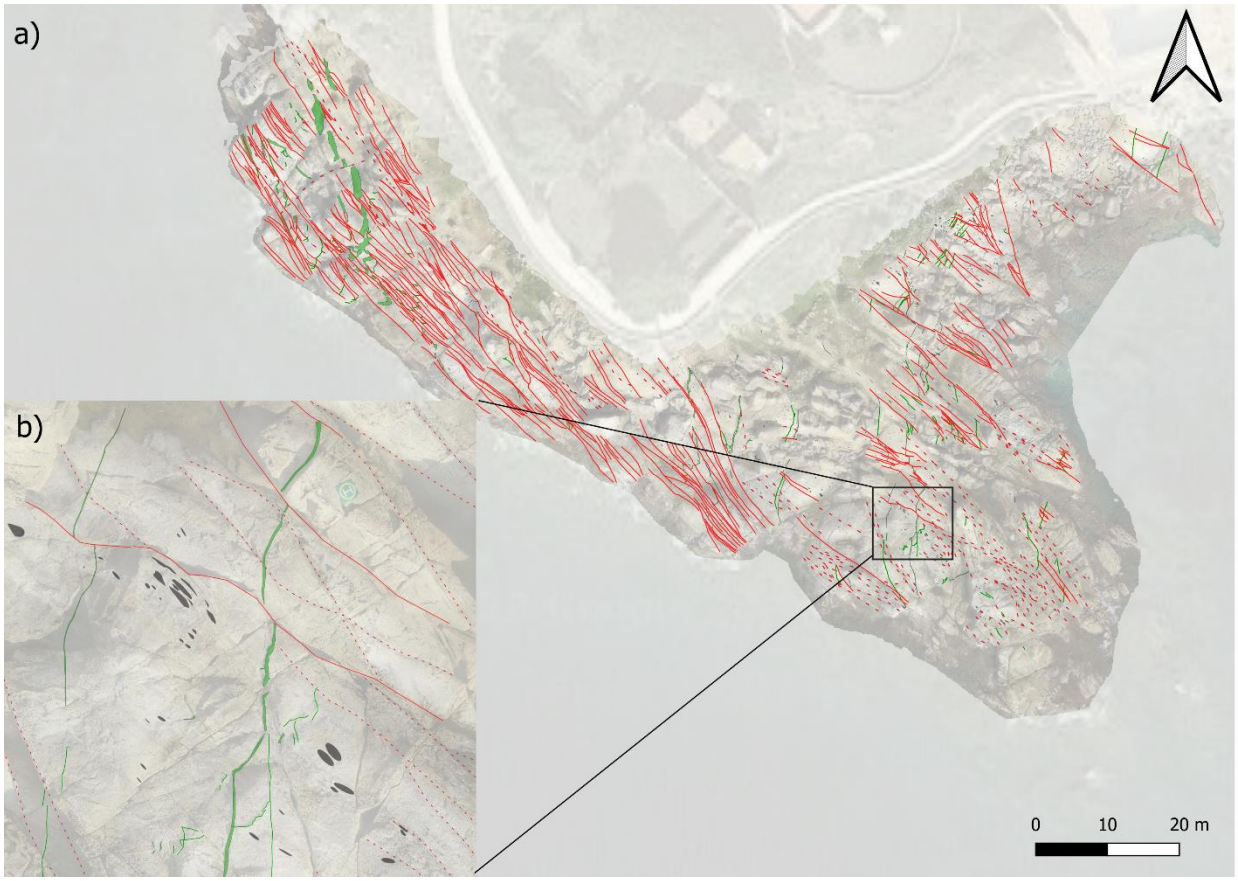

Figure 6.15 (a) Shear zone surface map compiled with QGIS. Younger anastomosing shear zones (red) displace and deflect aplite dykes (green). Shear zones maintain a consistent strike throughout the granodiorite body without displaying significant deflection or rotation. The orientation of intruded aplites changes between the Western and Eastern flanks by approximately 45 degrees. (b) close-up of the relation between shear zones, aplites dykes, and diorite enclaves.

Within shear zones, diorite enclaves can be elongated with axial ratios an order of magnitude larger than outside of shear zones (figure 6.4 bottom right). In contrast with the magmatic foliation, which is homogeneously distributed across the entire stock (Carreras, Jordi et al., 2004), the inhomogeneous characteristic of shear zones related to strain localization left large magmatic domains untouched by mylonitization (Simpson, C. and Sistach, 1982). The sense of shear of the conjugate sets of anastomosing shear zones was extracted by analyzing the following features: (i) the marginal deflection of Aplite dykes, (ii) marginal deflection of the shear zone foliation and (ii) the rotation of enclaves towards the shear zone. Within shear zones on a small scale, complex networks of centimeter-thick conjugate shear zones can be observed.

The consistent 'Step-like' displacement of aplites from the edge of the Eastern flank to the main shear zone indicates that shearing occurred progressively. The displacement of the aplites by shear zones increases towards the main central shear zone, figure 6.17, (a), indicating that surrounding shear zones are influenced by the large displacement (20.34 m) of the primary shear zone.

Figure 6.16 Outcrop section on the wester flank illustrating the predominant sinistral sense of shear. The aplites are predominately displaced in a bottom to the left direction. The aplites display a step-like displacement from East to West.

The bulk sense of shear across the granodiorite is predominately sinistral (figure 6.16), except for the primary 6 m wide dextral shear zone with the highest displacement cross-cutting the Roses granodiorite (figure 6.17). The primary dextral anastomosing shear zone in the center of the outcrop (figure 6.17-a-3) encompasses multiple individual discontinuities (purple planes plotted in 6.17-b) that displace the aplite to different degrees. The entire shear zone significantly displaces the large aplite dyke that enters the shear zone, figure 7.17-1 from the right-hand side that exits close to the same entry height on the left, figure 6.17-a-2. The strain varies across the different sub-shear zones, with the highest displacement occurring at the first shear zone on the right (12.5 m displacement). The aplite within the white square (1) in (a) & (b), when it exits at the bottom-left (2), is folded with the fold axis parallel to the shear zone. The large displacement of the primary shear zone in contrast to the remaining shear zones is remarkable and suggests that most strain displacement within the Roses granodiorite occurred along this primary shear zone. The geometry of the primary shear zone and displacement of the large aplite body indicates that the central section of the shear zone was pinched up towards the North while the remaining body remained relatively static. We can also observe that the main shear zone displays a concave outward trend towards the North. The enclaves in the mylonites are highly stretched out along the 6 m wide zone (3).

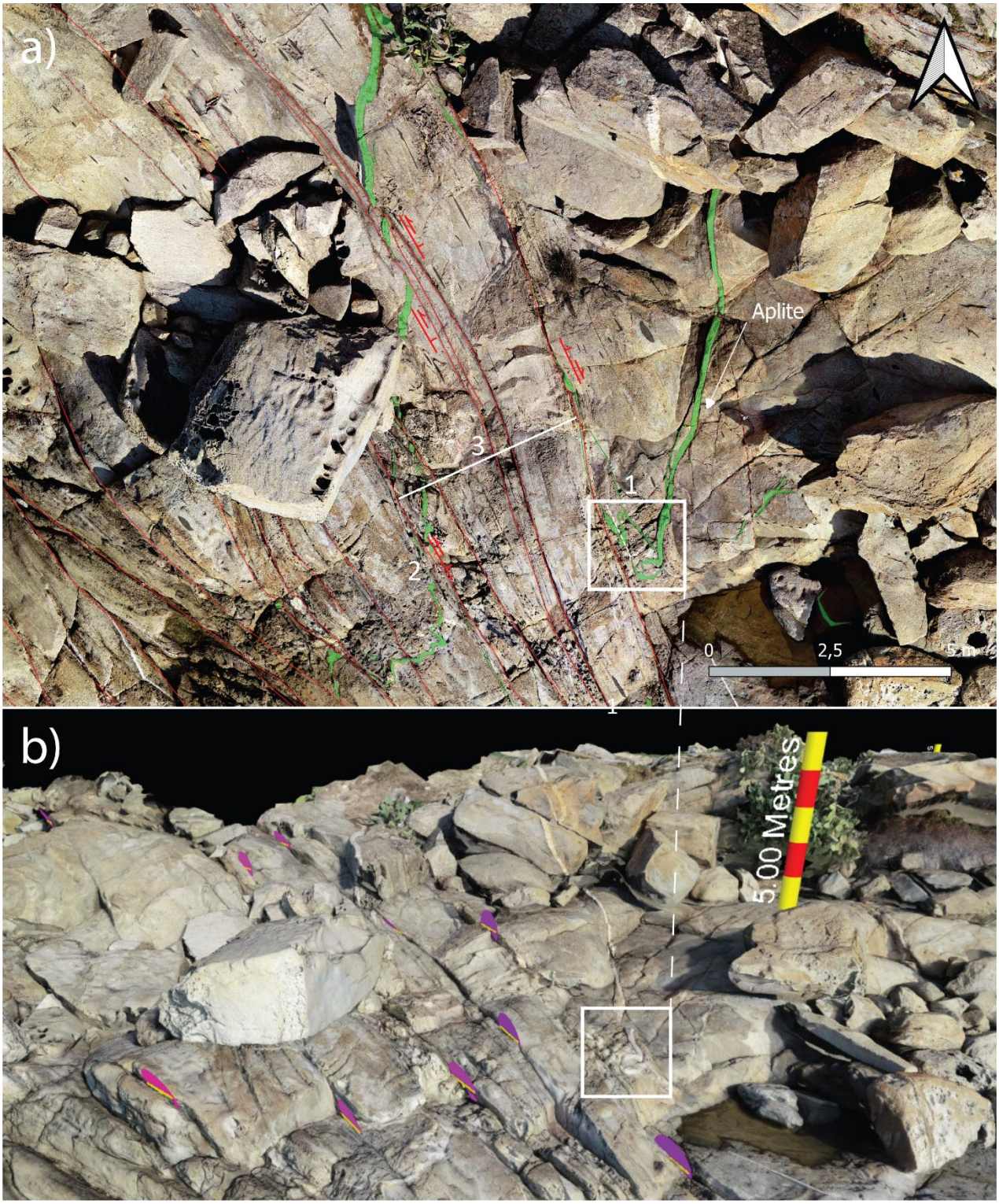

Figure 6.17 Orthophoto and 3D views of the central Roses granodiorite shear zone with the highest strain rate. a) Top-view orthophoto of a surface map constructed in QGIS, displaying an aplite dyke (right) displaced by multiple shear zones with different senses of shear before extruding at the left-hand side at a similar height. (1) represents the entry of the aplite dyke into the shear zone, (2) where it exits, and (3) the width of the high strain zone which is

approximately 6 m b) 3D side-view with top to north of the same shear zone in (a) with additional 3D strike-dip measurements (purple spheres) of the shear planes. Most planes dip towards the NE.

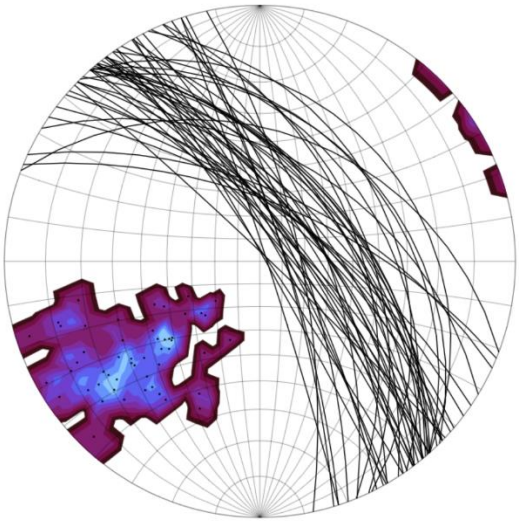

Figure 6.18 Shear-plane Stereonet plots compiled in VRGS of the Roses granodiorite. Measurements were sampled uniformly across the outcrop. Most shear zones across the outcrop consistently dip towards the NE.

Strike-dip orientations of the shear planes were measured using VRGS and plotted in a Stereonet (6.18). The 3D planes are predominantly dipping towards the NE, figure 6.19. The absolute conjunctive displacement of sinistral and dextral shear zones canceling out indicates that strain was significantly localized and the overall deformation environment cannot be attributed to homogeneous simple shear alone; instead, σ_1 is still predominately at a high angle to shear zone development. This is, moreover, supported by the high-angle fold axis developed at the shear zone flanks.

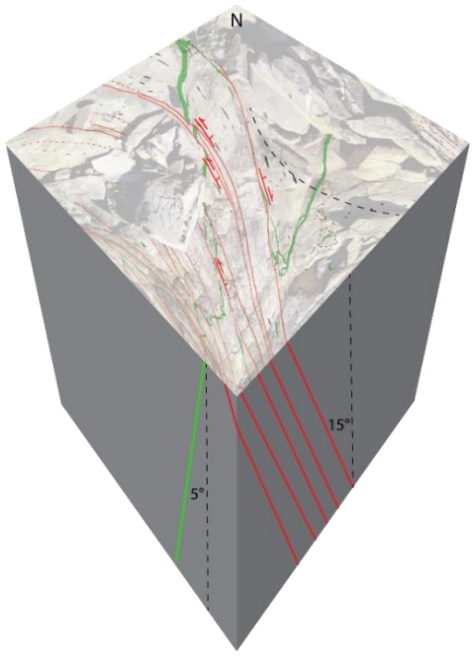

Figure 6.19 3D Schematic illustration of the variable orientations and relationships between shear zones and aplite dykes of the central Roses shear zone. Shear zones and Aplites dip in antithetic directions with a 20° angle difference—top to North.

Quantifying the cumulative Variscan shear of the Roses granodiorite is possible using the digitized maps within QGIS. The initial dioritic mafic enclave deformation using the Rf – Φ method is quantified at a RS=1.4 under close to three-dimensional homogeneous flattening (pure shear). The (Ramsay and Graham, 1970) method was used to determine cumulative shear for the subsequent deformation phase of the aplite dykes by n=120 shear zones. This technique is based on the combined use of a sigmoidal pattern of mylonitic foliation and changes in orientations and offsets of dykes by taking the bulk displacement – total width relationship of shear zones. Arguably, deformation occurred under a simpler shear model with inhomogeneous strain partitioning and localization without volume change (Carreras, Jordi et al., 2004). Orthophotos were combined with QGIS to trace dykes and measure their relative displacement associated with D_3 shear zones.

Table 6.2 below contains cumulative shear displacement values measured across three distinct domains: The central shear zone, the Eastern flank, and the Western flank. The bulk sense of shear across the granodiorite is predominately sinistral (figure 6.16), except for the primary shear zone with the highest displacement cross-cutting the Roses granodiorite (figure 6.17).

	Displacement by shear zones (m)	Total width (m)	Shear strain (RS)	Sense of shear
East of shear sone	19.70	57.20	1.3444	Sinistral
Central shear zone	20.34	11.94	2.703	Dextral
West of shear zone	19.18	46.60	1.4115	Sinistral

Table 6.2 Shear strain analysis across three sections affected by inhomogeneous post-dyke shearing.

In the central shear zone a large aplite dykes adjacent to shear zones displays folding with a fold-axis parallel to the shear zone and thus indicating a pure-shear component to the post-dyke deformation,

The length of the aplite was calculated at 1.353 m and the width of the folded aplite at 0.404 m, which would indicate a RS = 3.2.

Averaging the Roses post-dyke total displacement/total width relationships of the shear zones versus the total width of the unsheared rocks in the area, a cumulative shear ratio of 1.8 can be obtained. The average cumulative shear is lowest on the Eastern flank of the outcrop at 1.34. The Western flank has a slightly higher cumulative shear of 1.41. By far the largest cumulative shear can be observed along the central shear zone (figure 6.17). The obtained value is close to that of the observed in the folded dyke.

6.6.1 Late brittle fractures

Proceeding mylonitization follows a late cataclasis developed in narrow bands (Simpson, C. and Sistach, 1982). Brittle fracturing can be observed cutting across ductile shear zones and at shear zone tips, representing the latest structures formed in the granodiorite. These fractures commonly occur at an acute angle to the compressional field in the N – S direction, coherent with the orientation of the initial stress field during the emplacement of the stock (Carreras, Jordi et al., 2004). No significant displacement can be observed from late brittle fractures.

6.6.2 Uncertainty of Results

Due to the nature of digital data acquisition, there are always uncertainties in the obtained results. The primary uncertainty in this analysis is the GPS error (23.1013 cm) and to a lesser degree the reconstruction error (0.436 pix). Albeit the GPS error is low for the size of the batholith, not aligning the model properly along the XYZ axis will result in distortion during the orthophoto reconstruction, and consequently measurements done in QGIS will not be equal to the real-world dimensions. The GPS error compared to the size of the granodiorite (120m) yields a spatial error of 0.19%. With enough time to obtain a good RTK lock the GPS error can be further reduced.

6.7 Discussion

In the Roses granodiorite, a weak magmatic to solid-state foliation is defined by the preferred orientation of feldspar minerals along with the elongation of dioritic enclaves (Carreras, Jordi et al., 2004; Alvarado et al., 2013). The enclaves are predominately flattened and show a preferred orientation subparallel to the magmatic foliation which exhibits little to no deflection around the elongated enclaves, which promotes the assumption that the enclaves were slightly more competent during the development of the magmatic fabric (Paterson et al., 1998). The reason for this may be attributed to the increased viscosity due to the higher crystallization temperature of diorite than that of the granodiorite. The magmatic enclave foliation trends NW – SE (figure 6.8). The viscosity contrast assumption between the enclaves and the host rock is important to consider the enclaves as passive strain markers that record deformation instead of magmatic processes. Without this assumption the Rf/Φ technique can't be used. Therefore the Rf/Φ technique assumes the following: (1) enclave shapes and orientations were distributed randomly during the time of intrusion, (2) enclave shapes did not reflect other processes besides deformation during emplacement. The Rf/Φ technique measures the shape ratios and orientations of the enclaves to infer information about the total strain and place constraints on the deformation history (Carreras, Jordi et al., 2004). The deformation analysis predating the dyke intrusion performed using the Rf/Φ across 1017 enclaves. Two separate strategies were applied:

i) Pre-dyke enclave deformation (where dykes are undeformed)
ii) Bulk enclave deformation (pre-and-post-dyke)

The visual strain method was applied from (Karabinos and Warren, 2010) to determine the inverse strain ellipse by first rotating Φ to 0° followed by pure shear to orientate the points on the polar plots to create a radial distribution of points centered at the origin to simulate an initially random distribution of long axis orientations. The pre-dyke enclave deformation was measured where dykes display little to no deformation and away from areas of strain localization (shear zones) results in a finite strain ration of RS = 1.4 under pure shear conditions. The finite strain ratios for pre & post-dyke deformation are calculated at RS = 2.9 under pure-shear conditions. If we subtract initial pre-dyke strain ratios RS = 1.4 with the pre-and-post-dyke strain rations RS = 2.9 we can acquire and estimate of the post-dyke pure-shear component of a overall subsimple shear environment, RS = 1.5. Because the inverse deformation ellipse was obtained by pure shear, this would indicate a pre-dyke bulk shortening of about 40% and a post-dyke shortening of 50%. It is important to note that these values are approximations and as mentioned previously rely on a number of assumptions. Although there is dispersion in the data points of the bulk Rf/ Φ analysis, figures 6.9 and 6.10, the degree of dispersion is reasonable considering the significant variability in axial ratios across the enclave population. It is however clear that enclaves do indeed record finite strain to a degree as can be observed in the large increase in strain axial rations (RS) near and within high strain shear bands. The degree to which strain was recorded is dependent on: (i) presumed viscosity contrast and (ii) when the enclaves started to record strain vs when strain actually started. The analysis of such a large number of enclaves over a relatively short period of time and the resulting high-precision data is a testament to the potential of this digital technique for enclave strain analysis.

The shear deformation postdating dyke intrusion quantified using the Ramsay & Graham (1970) method has proven to be particularly effective and precise using QGIS due to the ability to trace a single dyke across multiple shear zones. This is much harder to do in the field due to the lack of proper overview across dykes that are several to tens of meters long. The cumulative shear was divided and calculated into 3 regions, East (γ = 1.3), West (γ = 1.5), and the main shear zone (γ = 2.7). This indicates that ductile shearing as a consequence of tectonic deformation was much more pronounced in the central shear zone. The average post-dyke cumulative finite shear was quantified at γ = 1.8 of which the main shear zone displays the same displacement as both the Wester and Eastern flanks in area 5x smaller (6 m wide). This clearly indicates the large degree of inhomogeneity of strain distribution. Considering the values for pre-dyke pure-shear shortening (40%) and post-dyke shortening (50%), the pre-dyke shortening is lower but of a similar order of magnitude to the shortening accommodated during mylonitization.

In comparison to the obtained results, Carreras et al. 2004 find a pre-dyke bulk horizontal shortening of 33% (-7%), the post-dyke shortening of 45% (-5%) and the cumulative shear of γ = 2.7 (identical). For most of the referenced values, they state that the values are most likely an underestimate of the total strain. The authors do not provide details as to the exact number of enclaves analyzed nor the data distribution, which makes comparing results for the pre-dyke intrusion difficult. That said it is unlikely that a similar number of enclaves (1017) were studied across the entire Granodiorite due to the large manual effort required. For the post-dyke deformation phase the authors state that displacement vs. total width relationships were obtained from different profiles. Having traced most aplites (figure 6.14) across the intrusive body I find the strategy used by the authors to use isolated profiles unsatisfactory to provide an average shear strain of the granodiorite due to the fact that shear zones display a wide spectrum in the degree of displacement. The analysis carried out in this manuscript to quantify the post-

dyke intrusion, traces a number of aplite dykes across the entire batholith, and measuring their shear zone displacement as the aplite traves through the magmatic body, produces much more representative results that are closer to the (real) bulk strain in comparison to the results from isolated profiles. This is yet another good reason to adopt digital workflows. Even with these discrepancies the obtained results in this study and that of Carreras et al. 2014 are of very similar magnitude.

The two deformation events, enclave deformation, and mylonitic shearing are clearly part of two separate yet progressive deformation phases separated in time by the aplite dyke intrusions that cross-cut metamorphic enclaves while both the aplites and enclaves are displaced, deformed, and rotated by younger tectonic deformation related shear zones. Although shear zones cut most aplites at a high angle, some aplites run parallel to the younger shear zones. The reason for this is uncertain; however, the following ideas are proposed; aplites (i) are rotated towards the shear plane, (ii) are a conjugate set of those in the eastern flank and naturally intruded at a different angle, (iii) are of different generations, more commonly associated with Cap de Creus pegmatite intrusions. What is clear, from the structures observed in the Roses Granodiorite, is that progressive deformation occurred under retrograde conditions/Syn-tectonic cooling with a predictable continuity of deformation from high-temperature enclave emplacement and deformation to low-temperature shearing (mylonites). As cooling of the Granodiorite occurs, strain partitioning increases from being accommodated across the whole batholith body to partitioning primarily towards localized ductile shear zones. This implies that although pre-dyke shortening is not clear at first sight due to it being accommodated across the entire batholith, it is Interesting of close to the same magnitude as the much more visible post-dyke deformation phase. The concentration of strain across the central shear zone might indicate the presence of either a rheological preference or a regional cooling gradient that prefers strain partitioning to the central shear zone. The transition to the final phase of the low-temperature brittle regime with discrete faults accommodates little to no displacement and is considered to be negligible relative to the bulk deformation. This trend from high temperature – high deformation to low temperature – low deformation is supported by obtained results.

6.7.1 Relationship between Shear zones

The different shear zones in the Roses granodiorite are interconnected and displacement of one shear zone influences an adjacent shear zone. This relation is clearly visible by the progressive ‘step’ like displacement of aplites that intrude in the East and get progressively dislocated to a higher degree towards the central shear zone in the center of the outcrop. This could indicate that there are two primary generations of shear zones in the Roses granodiorite. Moreover, the shear strain of the main shear zone and that of the entire Western flank are almost identical. As can be observed in figure 6.17, the central section of the main shear zone is pinched upwards while the aplite exists at the same height as it went into the shear zone. Moreover, the thickness of the shear zone increases towards the North indicating that there is a potential space availability problem during deformation.

6.7.2 Alpine overturning

The predominant sinistral sense of shear observed in the Roses granodiorite has been interpreted to be due to local Alpine overturning resulting in originally NE-dipping dextral shear zones appearing in the Roses area as sinistral (Carreras, 2001). This overturning occurs all along the southern border of the Pyrenean Axial Zone (Muñoz et al., 1986). Axial planes of Variscan folds in the southern shear belt

display this same anomalous southward tilting, causing original dextral shear zones to outcrop as sinistral.

6.7.3 Dating

Zircon dating performed by (Druguet, Elena et al., 2014) of the Roses granodiorite using $^{206}Pb/^{238}U$ isotopes constrains the intrusion age at 290 ± 2.9 Ma (Early Permian), younger than the 298±3.8 Ma (Late Carboniferous – Early Permian) of the Tudela Migmatite complex (quartz diorite). This is in line with a wide range of ages obtained for calc-alkaline volcanic and plutonic rocks in other localities along the central and Easter Pyrenees (Pereira et al., 2014). In a broader context, (Stampfli et al., 2013) suggest that the divergence in age between the older plutonic rocks in the west and younger rocks in the eastern Pyrenees can be attributed to a progressive Laurussia – Gondwana collision during the Late Carboniferous to Early Permian times.

In summary, the Roses case study illustrates that quantitative analysis of deformation using digital structural mapping is a highly efficient tool for tracing the tectonic history and accurately quantifying finite deformation.

7. Quantitative Analysis of the Cap de Creus Peninsula

The following chapters illustrate a case study of using qualitative and quantitative remote sensing techniques at the Cap de Creus peninsula to study pegmatite intrusions and their relation to shear zones. Cap de Creus is well known for its characteristic peraluminous pegmatites and anastomosing shear zones, ranging in size from a few centimeters to tens or even hundreds of meters. Depending on their fractionation evolution, Pegmatites of different types intrude the metamorphic schists above. Although comprehensive geochemical analysis (Van Lichtervelde et al., 2017) and field mapping of the Cap de Creus pegmatites (Corbella and Melgarejo, 1993; Van Lichtervelde et al., 2017)(Carreras and Vissers) have been carried out, mapping efforts have been mainly limited to in-field data or low-quality aerial surveys. Due to the large size of many structures, it is very difficult to get a proper understanding of the trend, significance, and relationship between them. The tendency for pegmatites to intrude as swarms are directly associated with the process and evolution of emplacement. Therefore, a digital mapping and statistical analysis approach was taken using Geographic Information Systems (GIS/QGIS) to better constrain pegmatite intrusions in the Cap de Creus Lighthouse area and their relation to shear zones. The statistical analysis carried out in this case study using the orthophoto aims to curb the spatial relationship between (i) individual pegmatites and clusters; (ii) pegmatites and the penetrative foliation; (iii) pegmatites and faults/shear zones.

7.1 Methodology

The aerial survey of the Cap de Creus region is subdivided into four grids, (i) the Easternmost Lighthouse Area (figure 7.2), (ii) the central NW – SE running shear zone, (iii) Westernmost Tudela and Culip area, and (iv) the westernmost shear zone, figure 7.1. A total of 50x RTK/VRS corrected GPS coordinates are collected with a controlled vertical and horizontal accuracy from GCPs distributed across the area and are used for georeferencing the Orthophotos and 3D models (figure 7.1). Due to the size of the model, no scalebar placement is required. A total of 20x flights are carried out, of which 15 are 3D flights (off-nadir) at 30 m altitude and 5x 2D (nadir) overview flights at 100m. Due to the sheer amount of data collected, this case study will only limit itself to a *very small* subset of the available data (Lighthouse

Area and Cala d' Agulle), the remaining data is available for further research, please contact Dr. Ernst Willingshofer.

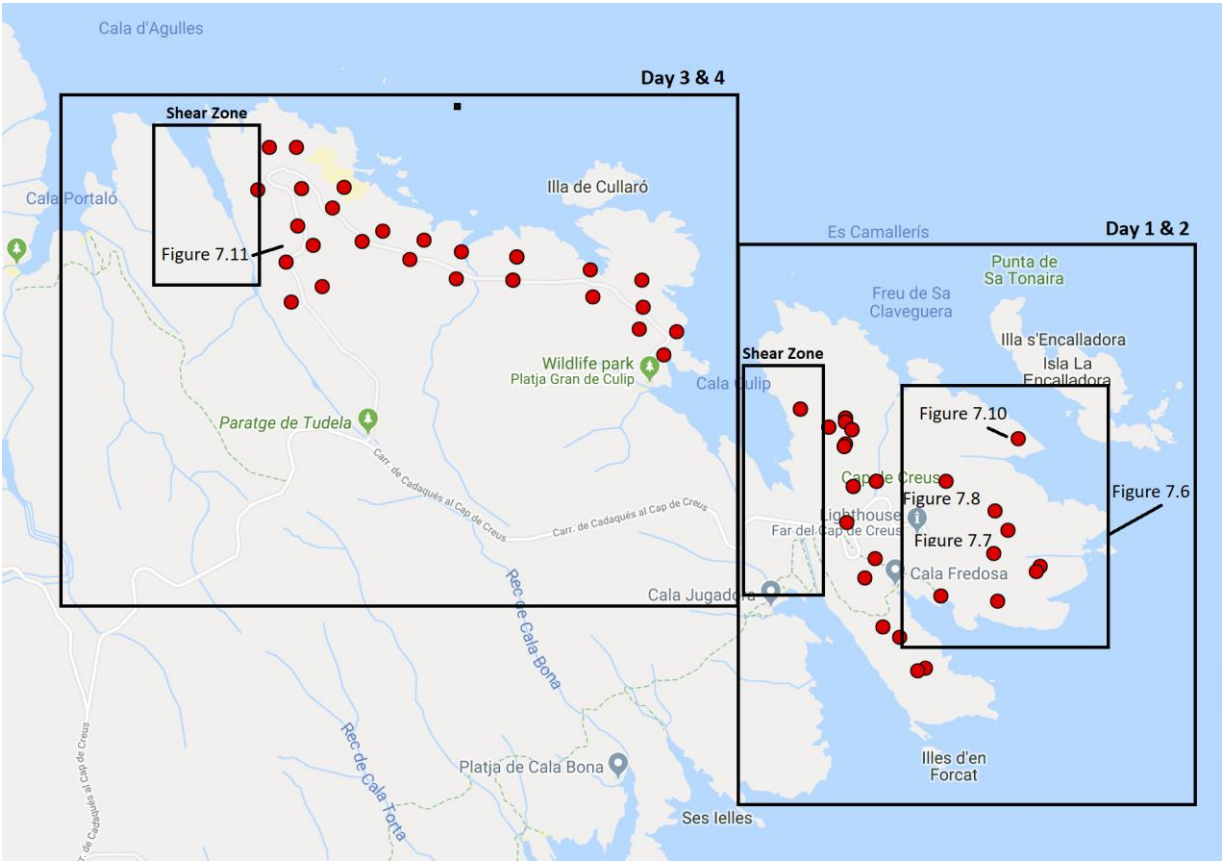

Figure 7.1 Cap de Creus survey area for 2D, 3D, and shear zone analysis. GCPs placed throughout the survey area are used for georeferencing. Two large shear zones in the West and East are mapped in greater detail for accurate quantitative analysis.

Agisoft Metashape® is used to produce a high-resolution orthophoto (3.31 mm/pix), DEM (8.34 mm/pix), and tiled 3D model (7 levels, 3.31 mm/pix), figure 7.3 & Table 7.1. The overview 2D flight is excluded from processing for orthophoto reconstruction to retain a uniform ground sampling distance. The geometrically corrected orthophoto and DEM are exported and processed in QGIS. The tiled 3D model is exported and processed in VRGS®.

Number of Aerial Images	1,597
Flight Altitude (3D)	12.7 m
Flight Altitude (2D)	20.0 m
Ground Sampling Distance (GSD)	3.31 mm/pix
Coverage Area	7.16e+03 m²
Tie Points	588,365
Projections	3,397,252
Reprojection Error	0.436 pix
Total GPS Error	23.1013 cm
Scalebar Error	7.48e-04 m

Table 7.1 Data processing parameters and errors.

Figure 7.2 Aerial Panorama of NE Cap de Creus (Lighthouse area). The site covers 0.256 Km2 and is bound by the Mediterranean Sea to the East.

Preceding aerial survey, 7 GCPs are placed uniformly across the southern, central, and northern terrains (figure 7.3). After placement of the control points, their GPS positions are recorded within reasonable horizontal and vertical error margins (Table 7.2). Due to the large scale of the outcrop and the relatively small absolute error of the obtained ground control GPS coordinates, the model was scaled to accurate world dimensions using solely the GPS coordinates of the GCPs. A total of 5 flights are executed in the lighthouse area, all 3D flights (off-nadir) at 50 m altitude above the ground surface. Due to the high topographic variance of the terrain, the actual altitude might vary between 50 – 100m.

Figure 7.3 Ground control points (GCPs) for the Lighthouse Area are used for accurate Georeferencing of the obtained photogrammetric model and orthophotos. GCPs are placed at different heights relative to the take-off point to reduce 3D distortion—the road for scale.

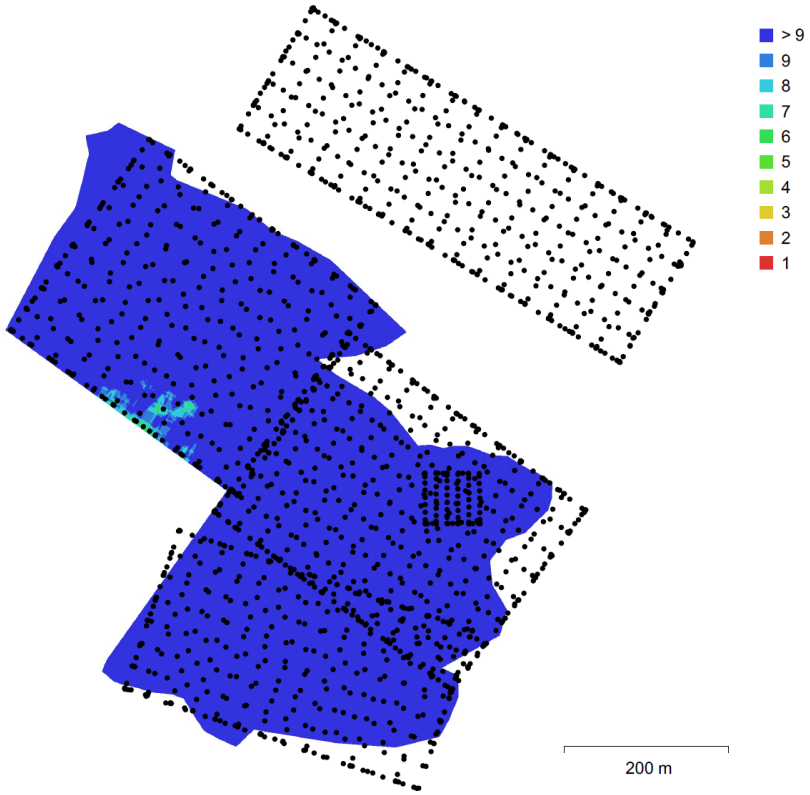

Figure 7.4 Cap de Creus camera locations and image overlap. Enough overlap between flights was maintained to produce a consistent coverage pattern. Only minor overlap reduction occurred at the northwestern boundary of the model.

Agisoft Metashape® was used to compile a high-resolution orthophoto (2.83 cm/pix), DEM (5.66 cm/pix), and tiled 3D model (7 levels, 2.83 mm/pix), Table 7.2. For orthophoto reconstruction, the higher altitude 2D flight was excluded from processing to retain a uniform ground sampling distance. The geometrically corrected orthophoto and DEM were exported and processed in QGIS for analyses. The tiled 3D model was exported and processed in VRGS®.

Number of Aerial Images	1,849
Flight Altitude (3D)	50 - 100 m
Ground Sampling Distance (Resolution)	2.830 cm/pix
Coverage Area	0.256 Km^2
Tie Points	297,893
Projections	2,020,117
Reprojection Error	0.418 pix
Total GPS Error	29.847 cm

Table 7.2 **Agisoft Metashape data processing parameters and errors.**

Digital georeferenced maps are used in QGIS to extract and analyze spatial statistical parameters of the pegmatite intrusions. First, each pegmatite body is manually mapped using polygons within QGIS to create a vector layer that can be statistically processed. After the relevant pegmatites are mapped the following parameters are computed using statistical functions within QGIS to quantify the spatial distribution of pegmatite occurrences, including grouping, scattering, and aligning features and their association with other structural units, including foliation and shear zones:

I. distance to the nearest neighbor
II. Ripley's L/K' function
III. Euclidean distance
IV. Spatial density distribution
V. Cluster analysis.

For each pegmatite polygon mapped a centroid point is generated with projected coordinate values and stored in a GIS database with information on class following the previously mentioned typology (Černý and Ercit, 2005).

To characterize and quantify the overall spatial distribution of pegmatite occurrences throughout the study area, the distance to the nearest neighbor (DNN) is used (Clark and Evans, 1954; Deveaud et al., 2013). The Euclidean distance is computed in a 2D map view between each centroid point, giving the DDN value.

$$R = \frac{\overline{r_0}}{\overline{r_E}} \tag{10}$$

r_0 is the observed average DDN value and r_E average value as expected for a purely random spatial distribution with:

$$\overline{r_E} = \frac{1}{2\sqrt{p}} \tag{11}$$

p being the point density across the study area expressed as a number of objects per unit area.

The R index value has a limited range from 0, corresponding to an extreme clustering where all data points are located at the same place, to a maximum of 2.1491 for points distributed in an even and hexagonal pattern (Deveaud et al., 2013).

The Ripley K/L function (Ripley, 1977) is another statistical tool used to complement the DNN analysis. This function allows for the description of clustering or scattering of elements at various scales.

$$K(r) = \frac{1}{n}\sum_{i=1}^{n} N_i(r)/p \quad (12)$$

With n the total number of points, $N_i(r)$the number of points within a neighboring distance (r) of the (i) points from the data set, and (p) the overall point density value.

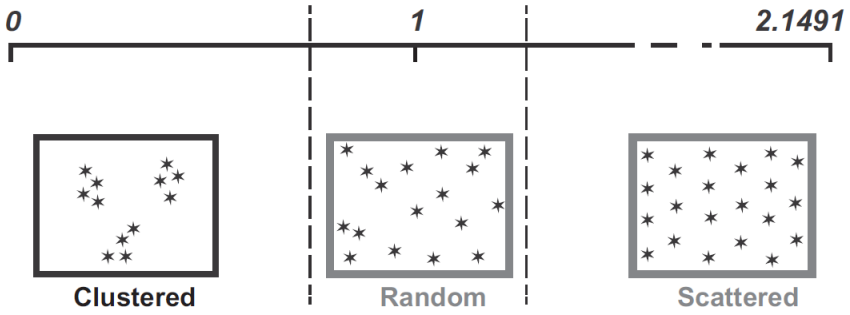

Figure 7.5 R index point distribution scale. R ration = observed average DNN/expected average DNN. An R-value of 0 illustrates a high level of clustering, 1 a random distribution and 2.14 scattering.

7.2 Results

Cap de Creus is well known for its characteristic peraluminous pegmatites and anastomosing shear zones, ranging in size from a few centimeters to tens or even hundreds of meters (Druguet, Elena et al., 2014). Depending on their fractionation evolution, Pegmatites of different types intrude the metamorphic schists above (figure 7.5). The volume of the intrusive pegmatites and distribution across the Cap de Creus peninsula is highly variable. Pegmatites form elongated dyke swarms and are easy to recognize by their light color ranging from light yellow to light brown. Most pegmatites have a sigmoidal or porphyroblast shape which stretches the pegmatite laterally sometimes forming even boudinage-like structures. Most pegmatites cross-cut the S_1 foliation and not all cut S_2.

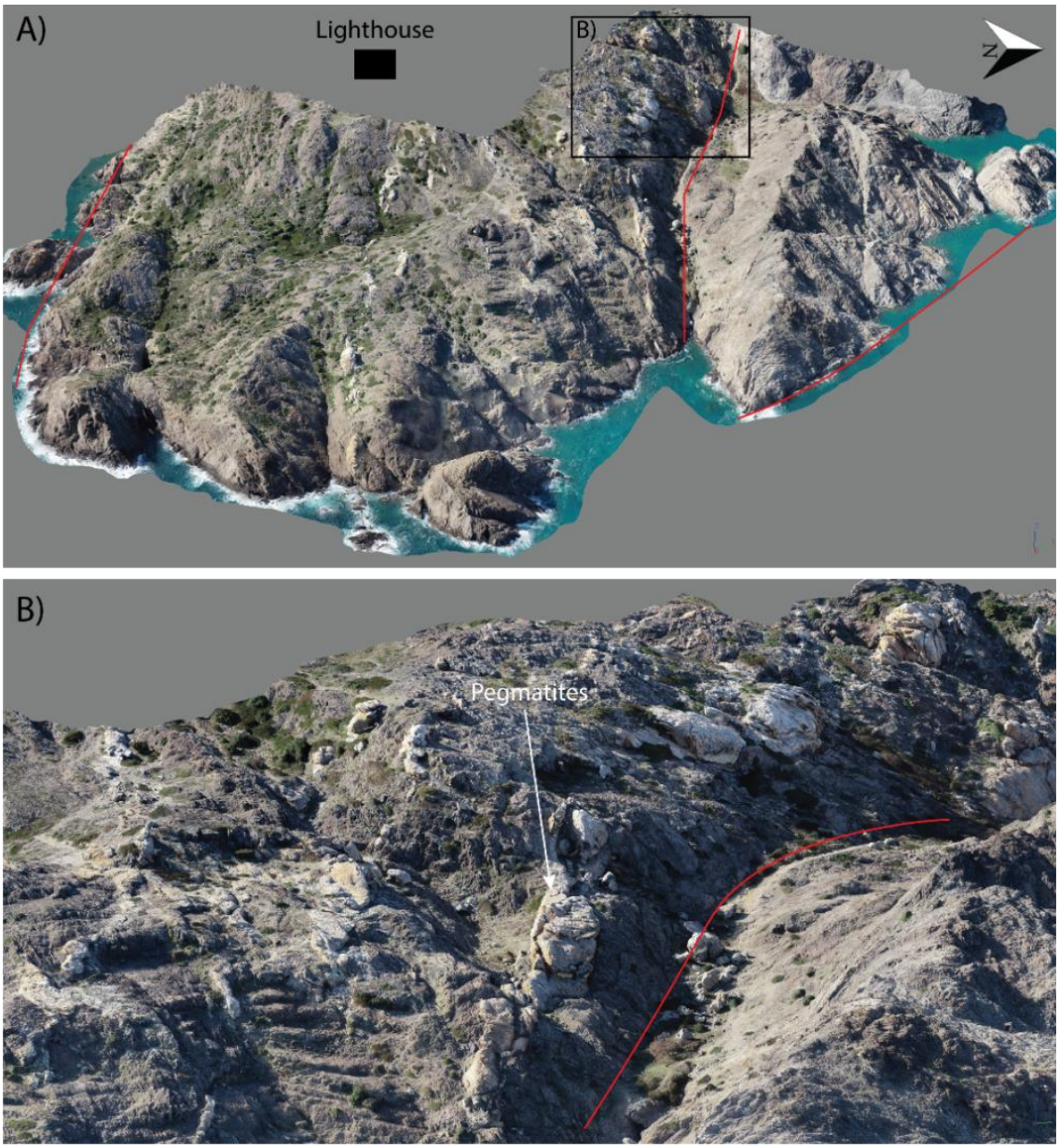

Figure 7.6 Overview of the Cap de Creus lighthouse Study area. The lighthouse area is located at the most easterly tip of Cap de Creus and is in a high metamorphic gradient zone with type I pegmatites. Wide shear zones indicated by the red lines border the lighthouse area. The pegmatites are the light-coloured elongated intrusions in (b).

Figure 7.6 illustrates a compiled digital map of the lighthouse area with the various structural features that can be observed including the pegmatites, S1/S2, and anastomosing shear zones (S3 mylonitic foliation). Two large shear zones run approximately WNW – ESE in the valley in the north and bordering the ocean in the south (figure 7.6). Both the northern and the southern large shear zones have a number of smaller antithetic shear zones. The primary foliation S_1 runs in a general NE – SW direction but is frequently cut by pegmatites and shear zones. The larger shear zones in the north significantly bend the S_1 foliation on a large scale beyond the direct shear–zone–foliation contact. The S_2 foliation is not well

defined in the Lighthouse area and due to the relatively high flight altitude (± 100m) the resolution of the imagery is insufficient to observe the S_2 foliation in detail. That said, there are some locations where S_2 can be observed with an NW – SE strike, close to parallel with the main shear zones. Where S_2 is present, a number of folded pegmatites display an axial plane cleavage that is parallel to the axial plane of S_2 (figure 7.7).

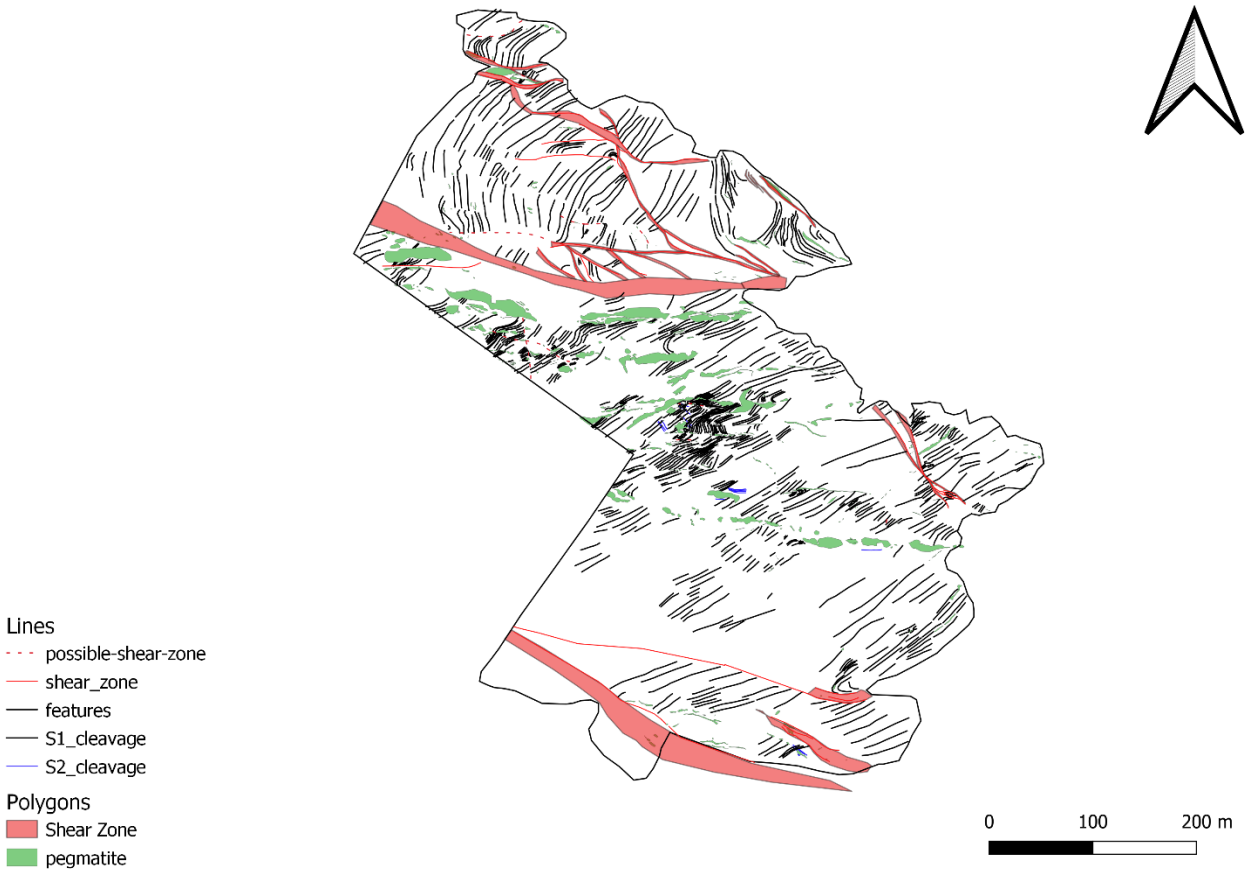

Figure 7.7 QGIS digital map illustrating the various structural features of the eastern Cap de Creus massif. Most pegmatites are highly deformed and bend towards shear zones. Most pegmatite bodies run in an E-W direction following a consistent strike. S_1 Runs consistently NE-SW throughout the Lighthouse area. S_2 is not very well visible from the drone imagery however in a few locations it has an E-W strike. Anastomosing shear zones are large in size and primarily concentrated along the outer edge of the area.

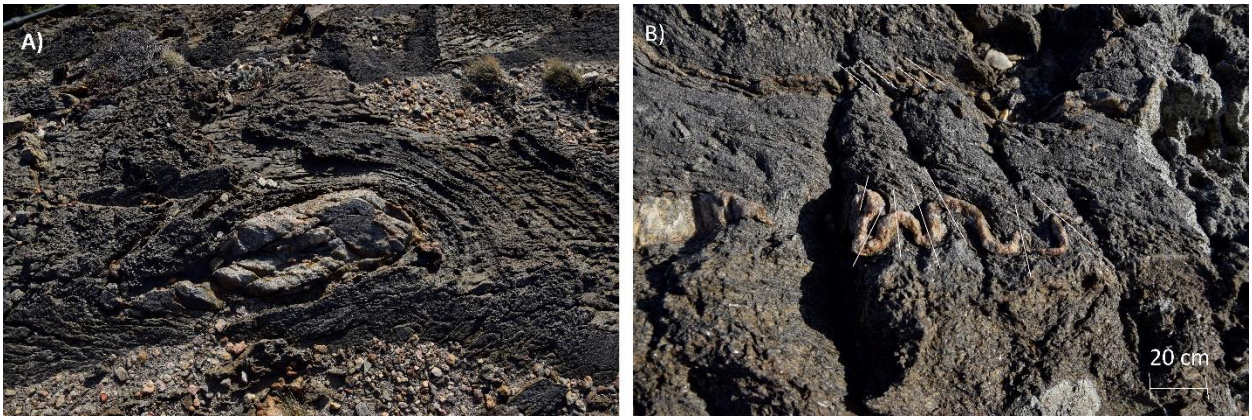

Figure 7.8 (A) Outcrop displaying a pegmatite intrusion surrounded by the host foliation S_2. Note the significant bending of the foliation around the pegmatite. Walking stick in the upper left corner for scale. (B) Small-scale isoclinal folding of the pegmatite body that runs semi-parallel to the S_1 foliation.

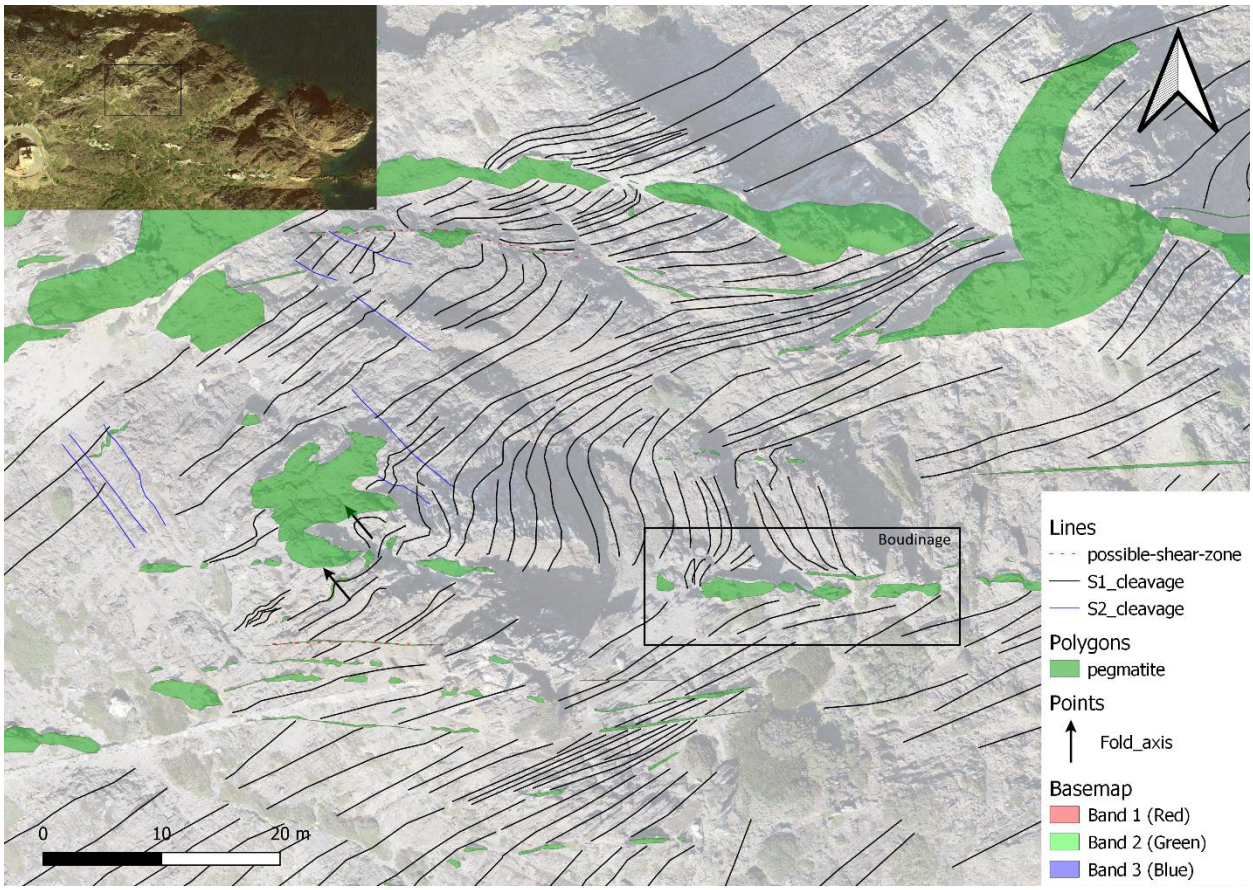

Figure 7.9 Section of the Cap de Creus Lighthouse area displaying the relationship between S_1, S_2, and the intruded pegmatite bodies. The observed pegmatites in this section cross-cut the S_1 foliation. For some pegmatites, the S_1 foliation displays a bending/deflection pattern around the intruded pegmatite. The generation of S_2 foliation is associated with folding in S_1 with the fold axis parallel to S_2.

From figure 7.6, we can see that most pegmatites of significant size intrude to the north close to the large shear zone. Pegmatites cross-cut most of the S_1 foliation and can display an apparent boudinage structure (figure 7.8). There appears to be an interaction between the S_1 foliation and the intruded pegmatites that deflect and rotate the foliation. In figure 7.9 the S_1 foliation deflects outward around the pegmatite body.

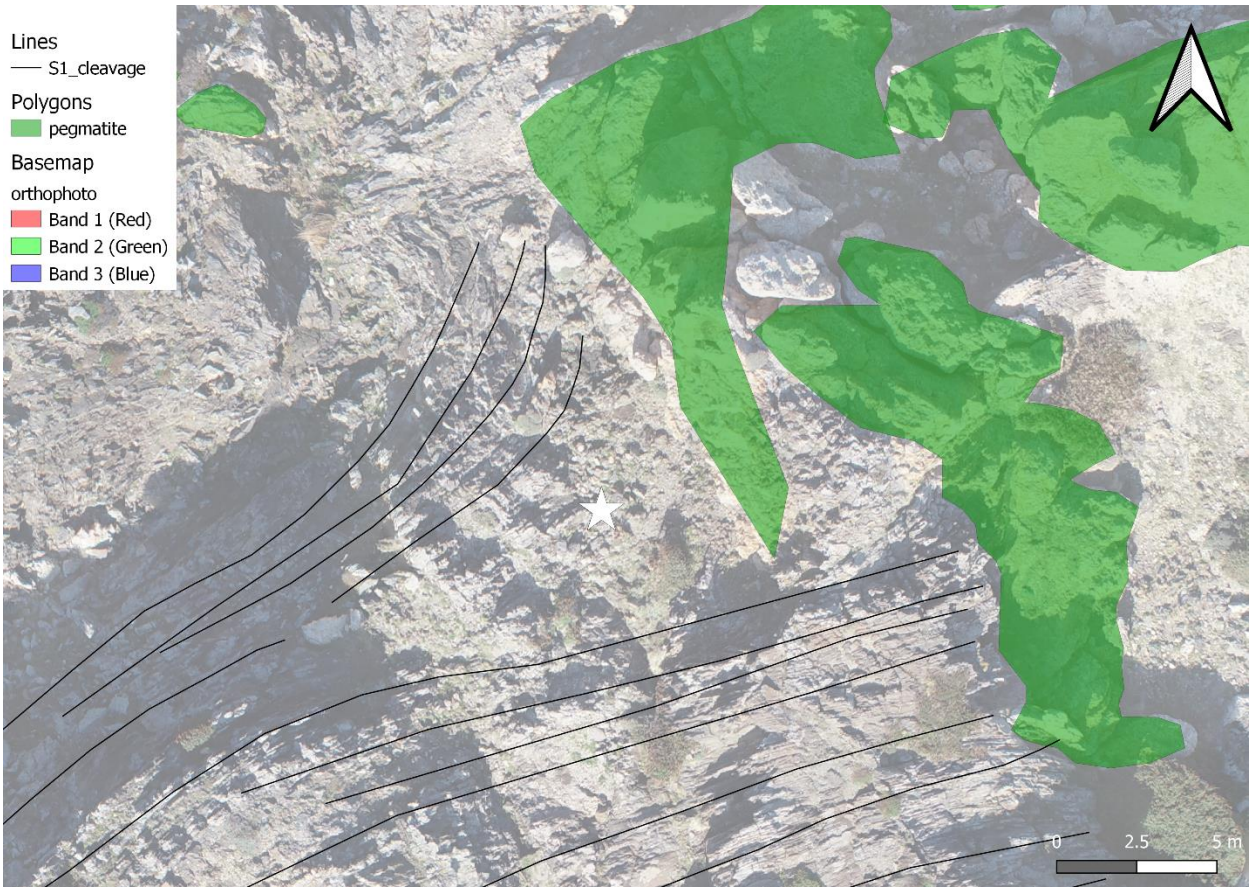

Figure 7.10. In the illustrated outcrop the S_1 foliation diverges outwards around the pegmatite body. At the interface between the S_1 foliation and the pegmatite body S_1 is cut by the intrusion.

Figure 7.10 illustrates a potential dome and basin interference pattern that is sliced on the XY axis to produce a radial S_1 foliation around the core of the dome (white arrow). This structure is only apparent using drone imagery and clearly shows the foliation bending around the structure while the foliation within the core has an irregular strike that is hard to define, the colour is also different and darker than the surrounding foliation. The dome-shaped structure is surrounded by two large shear zones, one in the valley to the south and one to the north near the ocean. The continuity of the shear zone near the ocean is difficult to define. A number of synthetic shear zones branch out of the large shear zone in the valley to the south upwards. Their continuity is also not certain from the obtained imagery.

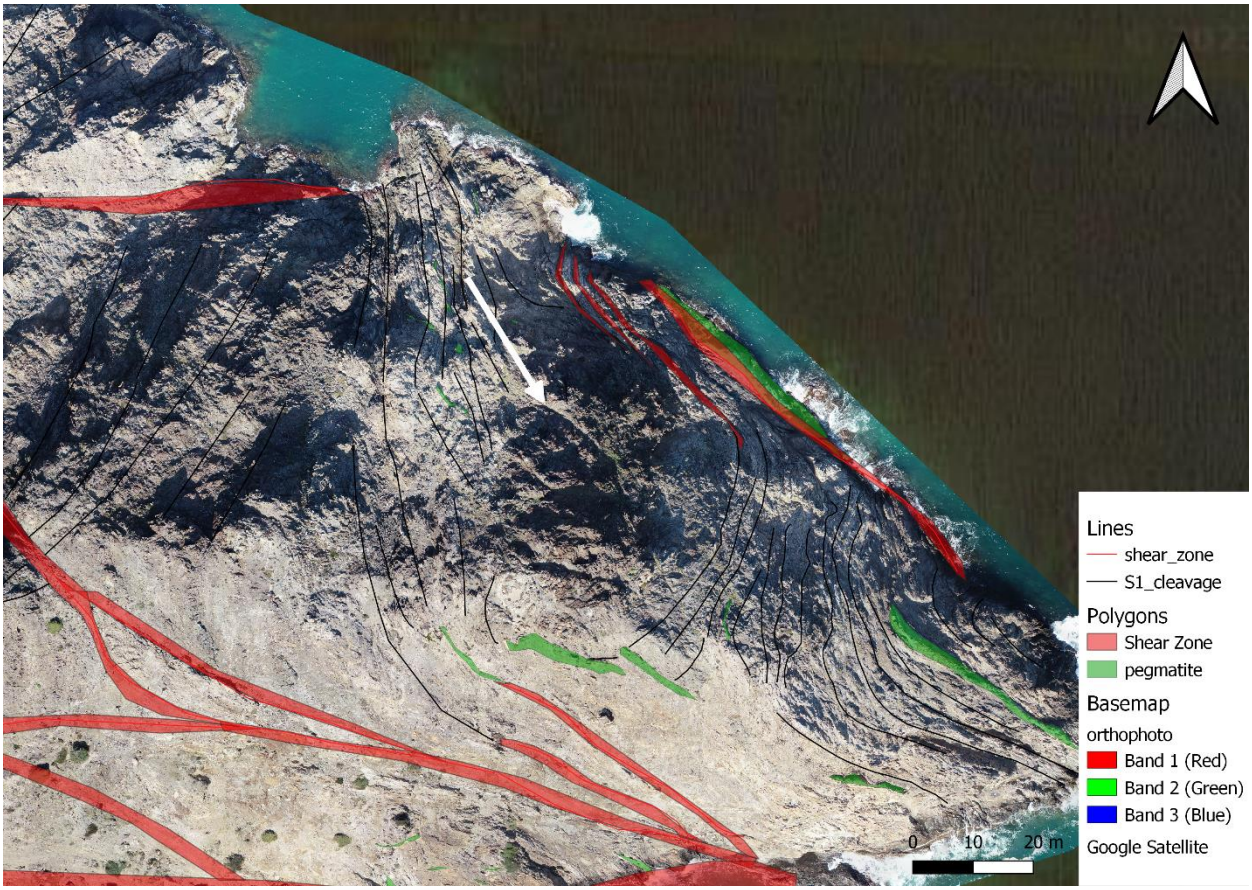

Figure 7.11 A potential dome and basin structure observed from the drone imagery displays the S_1 foliation bending around the core of the dome. The strike of the foliation within the core is not easily definable and is much less linear than that of the surrounding S_1.

Towards the NW of the Cap de Creus peninsula, the S_2 foliation becomes more pronounced, and medium-grade schists give way to schist-migmatite complexes and high-grade highly deformed schists, figure 7.11, Cala d' Agulles. The S_2 foliation rotates from mostly E – W in the lighthouse area (figure 7.6) to NE – SW in Cala d' Agulles where the S_1 foliation ceases to be clearly visible (figure 7.11). To the NW the pegmatite intrusions are significantly larger than in the Cap de Creus region. Three different large shear zones were identified, a large zone running through the Cala d' Agulles valley and two large shear zones near Club Med. A number of smaller anastomosing shear zones run between the three large shear zones and deform the pegmatites and the S_2 foliation. The edge of the large pegmatite to the north is deformed significantly with parts of the pegmatite being displaced tens of meters to the south by the shear zone.

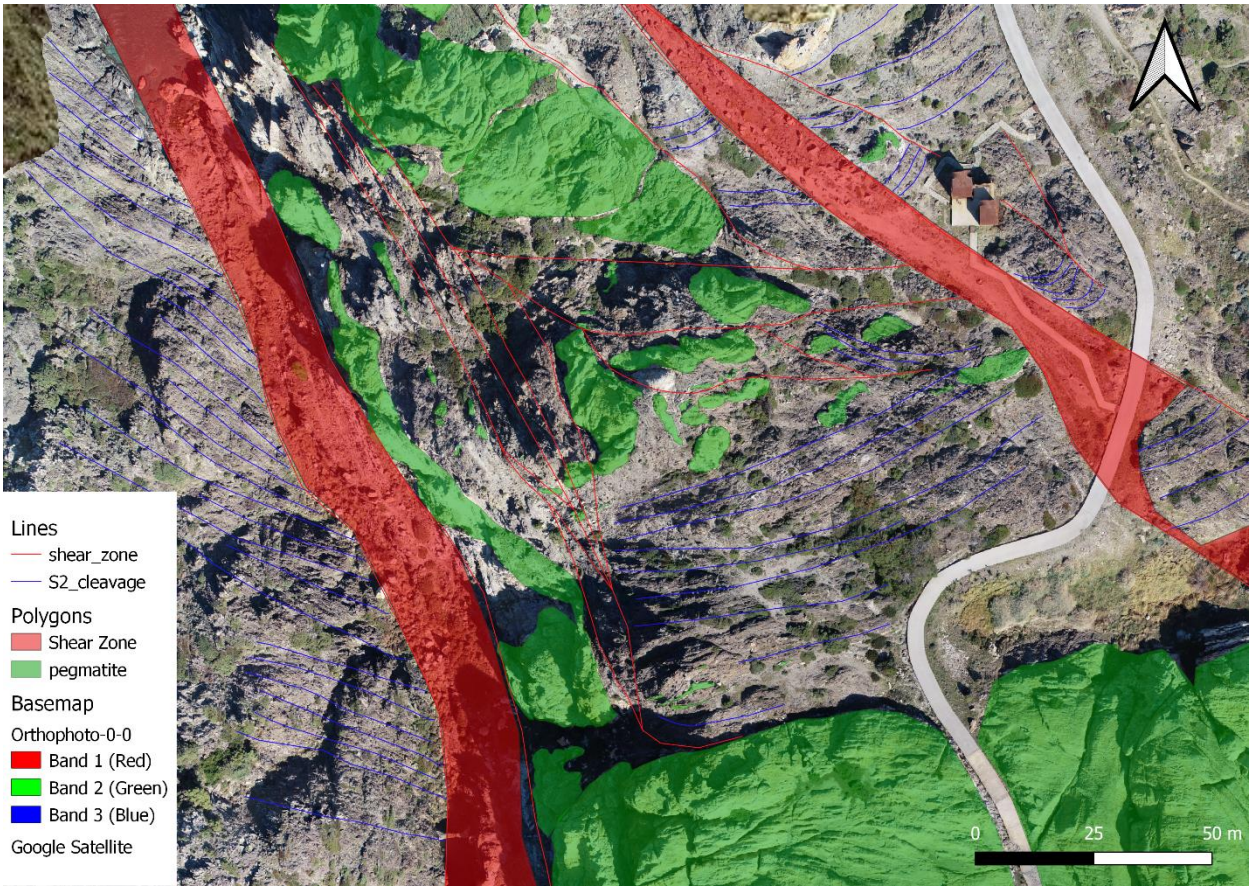

Figure 7.12 Digital map of the Cala d' Agulles main shear zones and surrounding pegmatites. Three distinct shear zones have been identified in the Cala d' Agulles region, a large shear zone in the central valley and two at Club Med. Smaller Anastomosing shear zones interconnect with the valley shear zones. The S2 foliation is pronounced and changes significantly between the Wester and Easter margins of the central valley. The S1 foliation is not clearly visible from the drone imagery.

7.2 Introduction to Spatial Analysis of the Eastern Cap de Creus Lighthouse Pegmatite Field

Most structural, metamorphic, and magmatic features observed in Cap de Creus do not occur randomly. There is a consistent structural trend of S_1 and S_2 throughout the area, reflecting the structural forces during the time of deformation. The metamorphic gradients are furthermore continuous across the Cap de Creus peninsula as can be predicted by available knowledge. For the pegmatites, however, the nature and characteristic of their distribution is unknown. Why do pegmatites intrude in the observed locations and not elsewhere and what is the controlling factor that determines pegmatite intrusion? Digital vector maps compiled from mapping the pegmatite population using QGIS enable spatial statistical analysis to (possibly) constrain the nature of pegmatite intrusion. Albeit the results below are a first experiment in this direction, there is much room left for further research.

7.2.1 Results

In this study, 478 occurrences of pegmatites have been mapped using QGIS at the Cap de Creus Lighthouse pegmatite field to quantify their spatial distribution. The following parameters are calculated and presented in the table below: (i) distance to the nearest neighbor, (ii) Ripley's L/K' function, (iii) Euclidean distance, (iv) spatial density distribution, and (v) cluster analysis. Figure 7.12 & Table 7.3.

Observed mean distance (m)	5.246
Expected mean distance (m)	12.954
Nearest Neighbor Index (R)	0.405
Standard Distance (m)	183.230
Mean Distance (m)	98.99

Table 7.3 Statistical analysis results of pegmatite population between the northern and southern Cap de Creus shear zones. N=478.

The distance to the nearest neighbor (DNN) or observed mean distance is calculated at 5.246 m (Clark and Evans, 1954; Deveaud et al., 2013), table 7.3. This represents the mean distance between two individual pegmatites. The expected mean distance is the expected distance between two pegmatite bodies if the distribution is random. The Euclidean distance is computed in a 2D map view between each centroid point, giving the DDN value (figure 7.12, c).

Using Ripley's L/K' function, the R-value, also known as the degree of clustering was measured at 0.405. From figure 7.13 we can observe that a R-value of 0.405 is associated with a significant degree of pegmatite clustering in 5 distinct clusters (figure 7.12). The different computed clusters can be observed in figure 7.12.C where each color represents a specific cluster group. Here clusters are formed in relationship to the distance of the shear zones. Because the random distribution of points represents R = 1, R = 0.405 represents *2.5x more clustering than expected* (i.e., points are about two and a half times closer to each other than expected for a randomly distributed set with the same number of points (Deveaud et al., 2013)), figure 7.13.

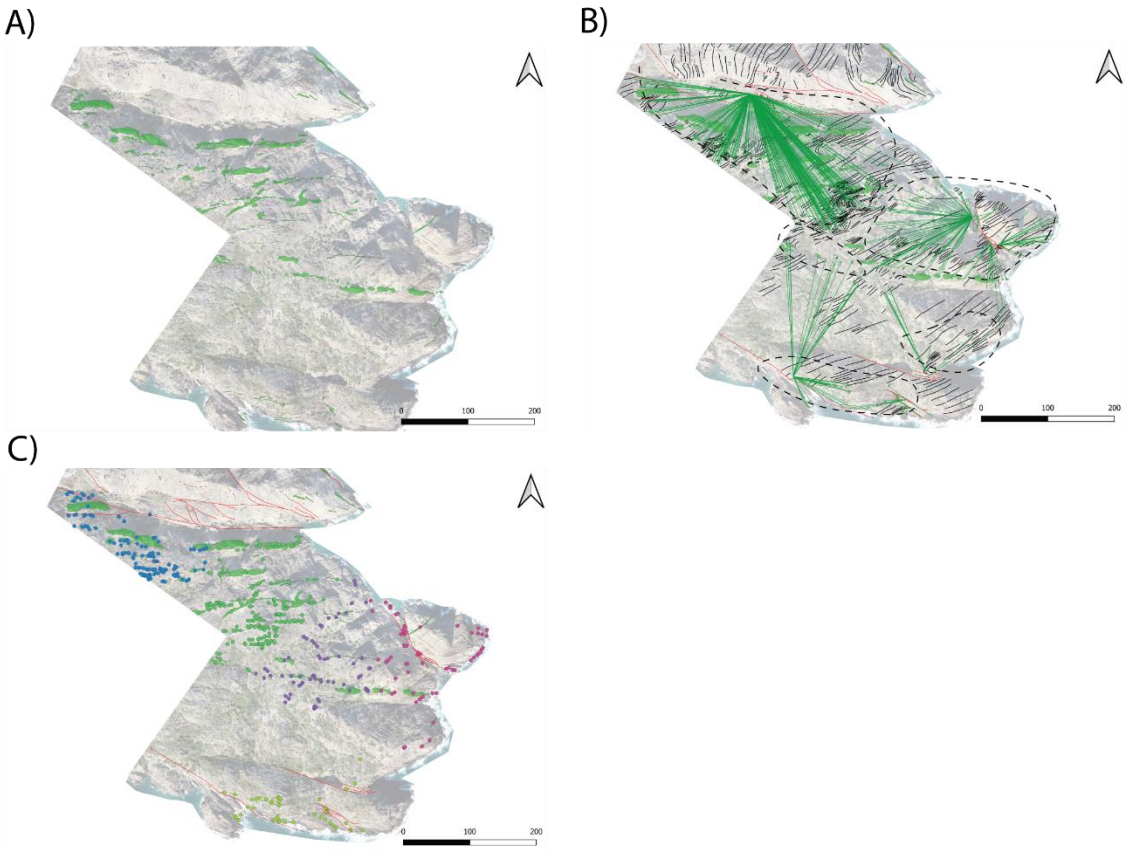

Figure 7.13 (A) Overview digital map illustrating the various pegmatite bodies of the Eastern Cap de Creus Massif. Pegmatites are oriented roughly E – W. (B) Distance to the nearest hub from shear zones to pegmatite centroids. (C) Ripley's K function cluster analysis (4 classes).

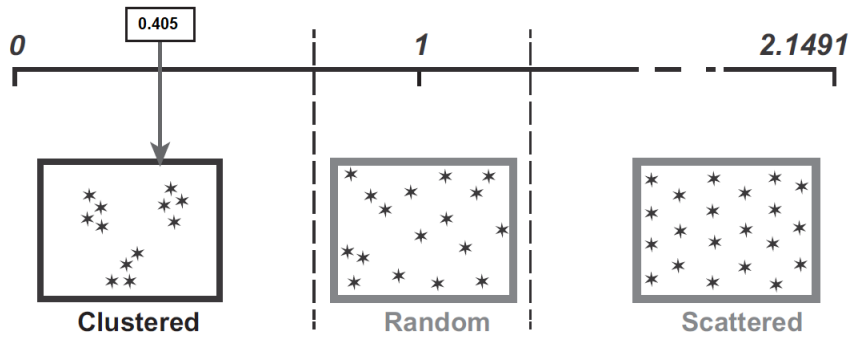

Figure 7.14 R index point distribution scale. R ration = observed average DNN/expected average DNN. An R-value of 0.405 illustrates a high level of clustering of the pegmatites.

Figure 7.14 below illustrates the calculated standard distance and mean center for the Lighthouse pegmatite population. These parameters illustrate where the highest concentration of pegmatites is located within a circle polygon dispersed around a central point feature (mean center). The radius is equal to the standard distance of the features (figure 7.14).

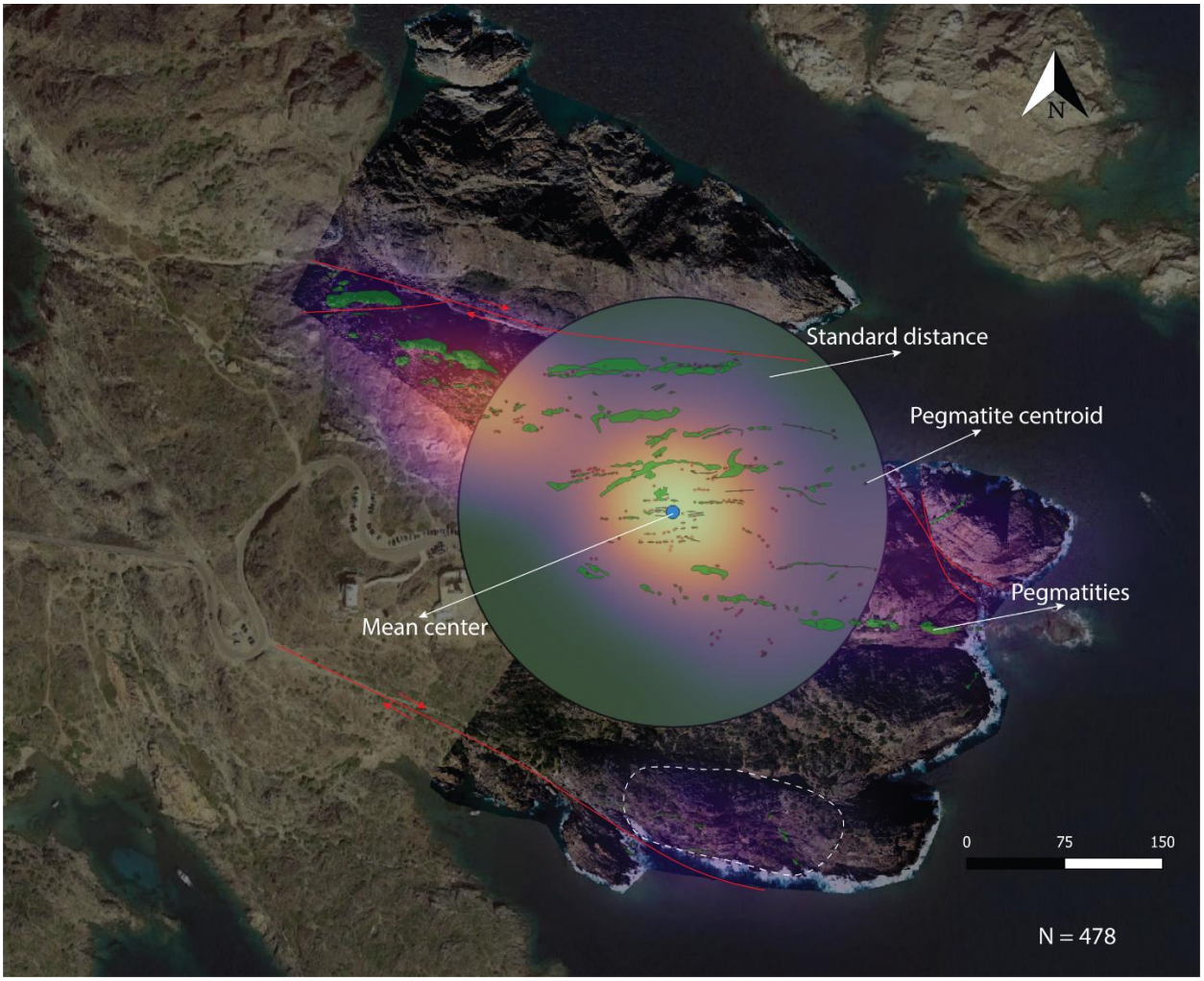

Figure 7.15 Map of the Cap de Creus Lighthouse area including localization of the recognized pegmatites. Red dotted lines illustrate the pegmatite centroids which are used for the various statistical analysis. The map pegmatites are bound by two large cross-cutting shear zones in the South and North. Mean Center and Standard Distance analysis of the pegmatite population is overlain on the map together with wither respective concentration heat map.

The standard distance circle and mean center are located close to the shear zone extending from the north to the east of the Lighthouse area. A secondary small cluster is located near the southern shear zone. The heat map of pegmatite distribution compiled in QGIS clearly aligns with the mean center maximum.

7.3 Discussion

The exact timing of pegmatite emplacement can be inferred by the relation between the metamorphic foliation and the pegmatite dykes. Most of the pegmatites cross-cut S_1 but not the S_2 foliation, indicating an emplacement timing Post S_1, coeval with Syn to late D_2 but pre-D_3 (Van Lichtervelde et al., 2017). Pegmatites appear to play a significant rheological role in the deformation of the S_1 foliation and act as active strain markers that deflect and rotate the foliation around them significantly (figure 7.9). Some pegmatites that do cross-cut S_2 can be considered late to post-D_2 intrusions. Early D_2 pegmatite intrusions are bordered by an S_2 foliation with a stronger footprint than those intruded later and have thus undergone more D_2-related deformation (figure 7.7, A). The folding relationship between pegmatites and the country rock can also be used to further constrain the relationship between intrusion and deformation (figure 7.7 – B). Most folds of the dykes are coaxial with those in the country rock but are more open, indicating that some D_2 deformation had occurred before pegmatite emplacement and that deformation continued after emplacement and thus the pegmatites are syn-tectonic (Carreras, J. and Druguet, 1994).

The Rose diagrams in figure 7.15 compiled using VRGS from the rendered 3D model of the lighthouse area display the strike of S_1, S_2, S_3 (Shear zone mylonitic foliation) and the pegmatites bodies. From the diagrams, it can be observed that the orientation of S_2, S_3, and the pegmatites are closely related in a general E-W trend (Carreras, J. and Druguet, 1994). Digital mapping techniques comparing the S_1, and S_2 cleavage trends and the intruded pegmatites suggest that the dykes have a significant decoupling and partitioning effect on strain development (figure 7.8). A number of observations support this including: (i) offset and bending of the metamorphic foliation around the intruded pegmatites; (ii) sigmoidal shape of most pegmatites with considerable limb rotation and extension parallel to the maximum instantaneous stretching axis (ISS); (iii) differential rotation and deformation of the metamorphic cleavage (S_1 and S_2) above and below the pegmatite center line including the formation of folds. The observed impact of pegmatite emplacement on foliation development may indicate a broader controlling factor on proceeding structure development as a result of the rheological contrast through time between the emplaced pegmatites and the surrounding metamorphic lithologies and cleavages.

The digital analysis shows that pegmatites are statistically grouped in clusters along large discontinuities like shear zones within a radius of 0 - 200 m (figure 7.12, B). In the Cap de Creus Lighthouse area, two large D_3-related mylonitic shear zones are present along the northern valley and the southern margin near the sea. A minimum of three to four clusters of pegmatite bodies can be identified using spatial analysis algorithms near the northern shear zone. Moreover, one isolated cluster can also be identified near the southern shear zone. It is currently unknown if the clusters near the northern shear zone are part of a single large intrusion or multiple small blobs.

The high clustering rate near large shear zones in the Cap de Creus Lighthouse area suggests that there is a strong 'preference' for pegmatite emplacement. The mean center and standard distance analysis carried out in QGIS indicate that the hotspot of peak pegmatite development by the number and volume of intrusions is located near the northern main shear zone. This quantitative result indicates that there is a correlation between the intrusion of large volumes of pegmatites and the development of large shear zones, figure 7.14. While analyzing the Cap de Creus pegmatite intrusions it becomes clear however that this is not the only possible control on pegmatite intrusions. In the south where the metamorphic grade is lower, very few pegmatites intrude, while in the schist – migmatite complexes in the north the volume of intrusion is significantly higher. This points to a correlation between the metamorphic grade and the pegmatite intrusions. One possible explanation for this could be that higher

metamorphic grade zones have a lower rheological competence which facilitates the intrusion of pegmatites along D_2 discontinuities which promotes the development of anastomosing shear zones along these discontinuities and pegmatite bodies. The strike alignment of S_2, syn-to-late D_2 pegmatites, and D_3-S_3 related shear zones most likely indicates a progressive transpressive deformation phase that aligns the structural features with the principal stress axis as deformation progresses including the boudinage of pegmatite bodies.

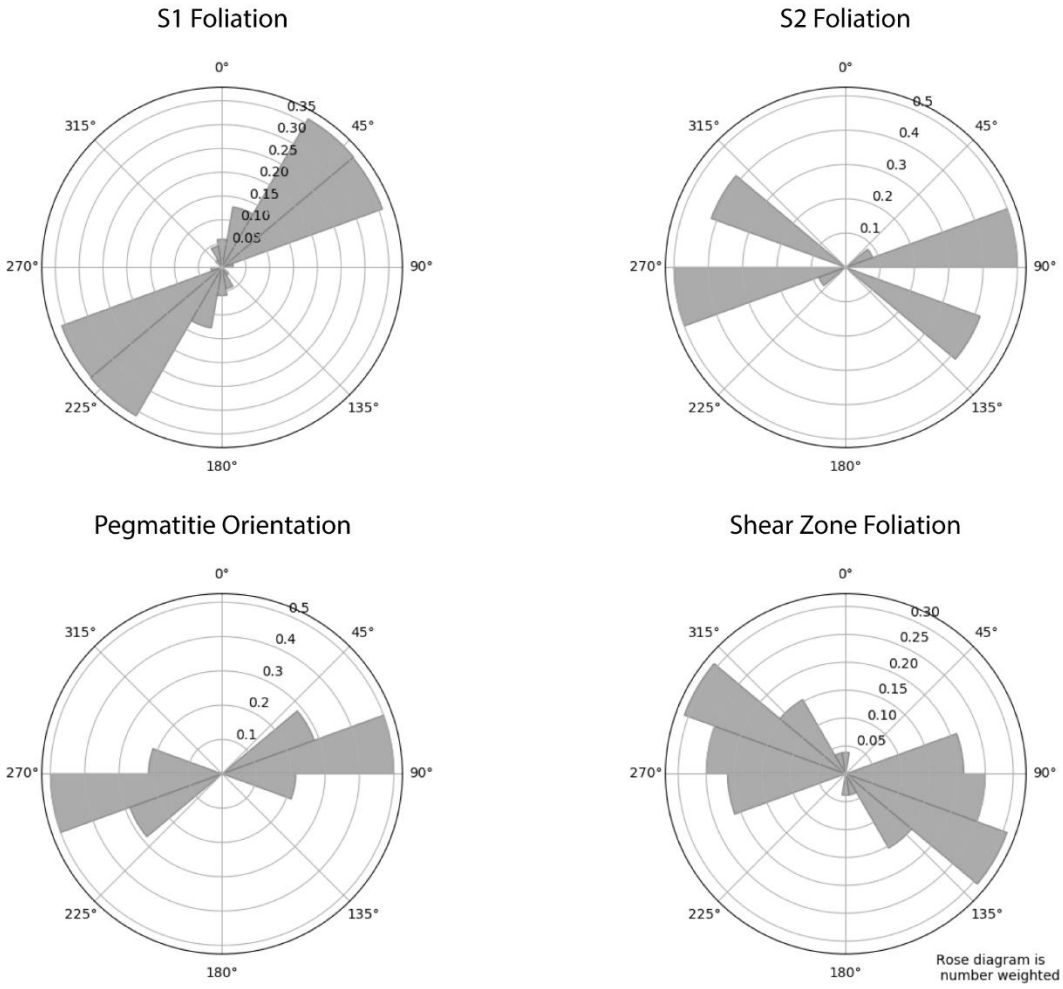

Figure 7.16 Rose diagrams compiled using VRGS illustrating the strike of the Cap de Creus Lighthouse area metamorphic foliations S_1, S_2, D_2 related pegmatites and D3 shear zones (n=85). A clockwise rotation of the foliation can be inferred ranging from the S1¬ foliation to the D3 shear zones. The total rotation magnitude near 120°. Slight fluctuation occurs in the strike of the foliation depending on the distance to shear zone discontinuities.

The relationship between the cross-cutting of S_1 foliation and deflection of S_2 foliation constrains the intrusion to Syn to late D_2. It is possible that the low competence Lighthouse pegmatites intruded along D_2-related discontinuities which are subsequently explored by D_3-related shear zones. The impact of pegmatites on the rheology of the area would explain the local high degree of S_1/S_2 foliation deflection

in comparison to the consistent strike in the south where pegmatites are absent. If pegmatites intruded along D_2-related discontinuities which are subsequently explored by D_3 shear zones, it would imply direct progressive deformation and structural link between D_2 and D_3 instead of being two separate deformation phases. At least visually, from the drone imagery, the consistent orientation of structures at the northern Cap de Creus Lighthouse area indicates a strong link between D_2 and D_3. It could very well be possible that D_2 discontinuities are one of the first strike-slip manifestations of the onset of transpression. The source of pegmatite intrusion is however more difficult to constrain with digital mapping alone, especially when there is a lack of a clear parental source and as such requires further chemical and isotopic analysis. That said, due to the fact that there are several generations of pegmatite bodies across Cap de Creus associated with different phases of deformation, we can assume that there is a consistent parental magma source from which partial melting occurs. Two main sources of emplacement have been proposed for the origin of pegmatite bodies including, (i) the anatectic melting of the country rock and (ii) the extreme fractionation of a granitic melt. Anatectic in-situ melting of the country rock will result in similar unfractionated melts across different pegmatite clusters (Corbella and Melgarejo, 1993; London and Evensen, 2002; Van Lichtervelde et al., 2017).

7.4 Limitations

Although the remote sensing approach for quantifying shear zone strain works particularly well for the Roses granodiorite due to the clear displacement of the aplites relative to the shear zones, it has proven to be difficult to execute this same strategy for the Cap de Creus Lighthouse area. The main reason for this is the lack of visual indicators that can be used to quantify strain. Further research should be done if there are any potential solutions to this problem using 2D or 3D models. The presence of vegetation also hinders the compilation of a good surface map to which there are no direct solutions beyond taking analog measurements and photographs where possible. For future work, we suggest doing a 3D spatial analysis using VRGS of the lighthouse area and attempting to build a 3D model of the subsurface of the lighthouse area with the surface measurements to expand on the relationship between the various structural features of Cap de Creus.

8. Conclusions

1. This work has demonstrated the potential of an integrated Digital Mapping approach to deliver reliable quantitative results that are consistent with traditional geologic methods. The produced Dense clouds, Depth Maps, Tilled Models, and orthomosaic's are valuable assets in evaluating the relationship between shear zones, foliation, pegmatites, and phases of deformation.

2. The raw exports from digital mapping can be archived for long-term storage and provide a real-world snapshot of the study area that can be consulted at any time. The generated models can be loaded into structural Geology software packages for data extraction and analysis.

3. Correct workflows for data acquisition are critical to obtaining reliable datasets for quantitative analysis. The margin of error in GPS measurements and the quality of imagery will directly influence how reliable the acquired datasets are. In contrast to analog measurements, this risk of error is smaller. However, it does come at the cost of being much more time-consuming and limited based on topographic availability.

4. The Roses granodiorite case study is presented as a reference example of an outcrop that can be studied using accurate high-resolution quantitative digital mapping to (i) measure strain ratios in mafic enclaves to determine the deformation matrix; (ii) measure aplite dyke and shear zone displacement; (iii) acquire structural strike and dip measurements and other 3D relationships between existing and intruded bodies; (iv) determine timing relationships between enclaves, aplite dykes and shear zones.

5. In this study, new constraints on the Roses Granodiorite bulk Variscan deformation are provided: By sampling a total of 1017 enclaves, the pre-dyke bulk deformation was quantified at 40% shortening under a close to three-dimensional homogeneous flattening/pure shear. The post-dyke shortening using the enclaves was quantified at 50%. The post-dyke cumulative shear, obtained by measuring strain from aplite dykes displaced yields a shear strain displacement of $\gamma = 1.8$.

6. Statistical analysis of 478 occurrences of pegmatites at the Cap de Creus Lighthouse pegmatite field using the Distance to Nearest Neighbor (DNN) yields an *R-value of 0.405,* suggesting a high clustering degree of the pegmatite occurrences near shear zones throughout the Cap de Creus Lighthouse area.

7. Surface and structural features including different generations of foliations, shear zones, and pegmatites can be used to determine different deformation phases and gain insight into the overall evolution of the area. In Cap de Creus a progressive transpressive regime can be inferred.

8. The Cap de Creus area represents a window into the Variscan mountain-building cycle where sedimentary rocks in a soon-to-be orogen are buried, progressively deformed under pressure (S_1

and S_2 cleavages), undergone metamorphism due to the increasing pressure and temperature, intruded by magma due to thickening of the crust and melting (potentially delamination) of the mountain root system followed ductile shearing (D_3) and the formation of mylonites during exhumation. This cycle is also clearly visible in the studied Roses granodiorite that intruded the low-grade metasediments above, undergoing high-temperature magmatic assimilation of the dioritic enclaves and homogenous deformation followed by continuous cooling that induces inhomogeneous train patterns, the formation of tension fractures filled by aplite dykes and finally medium-low temperature ductile shearing and mylonitization (Carreras, J., 2001; Carreras, Jordi et al., 2004). Roses is a pristine example of a analogue "Hard drive" that records a snapshot of the mountain building cycle by a cooling batholith that "freezes" orogenic-related deformation in its fabric as it cools.

9. This manuscript demonstrates that emerging technologies in the fields of remote sensing, photogrammetry, and GIS can be combined to aid Geologists in their mission to better understand our solid earth and carry out quantitative analysis effectively on digitized outcrops. Although the term 'Virtual fieldwork' has been used extensively over the last years as a way for Geologists and educators to provide some form of field experience, it is critical to understand that digital mapping is a tool to improve a Geologist's fieldwork, it is not a replacement thereof. It is critical to anchor digital to analog measurements and observations in order to validate the digital workflow.

9. A Glimpse into the future

The applications covered in this manuscript are only an introduction to the many ways in which these datasets can be used and attempt to stage some ideas of what could make its way into a Geologist's toolset in the future. The efforts made in this manuscript are not random, they build on top of the technologies deployed during my BSc thesis that covered the fields of Dynamic Photogrammetry 3D reconstruction, Virtual Reality (VR), and 3D printing. These technologies have since seen significant development, Tesla uses Photogrammetry for their self-driving cars, Facebook has made Virtual Reality cheaper and accessible to everyone and 3D printers are now affordable enough that they can be installed in small departments. As these technologies mature, Geologists are looking into deploying them into their respective fields to assist in research and teaching.

The goal of this MSc thesis was to push a step further and build the next link in this chain of available tools. In recent years drones or UAVs have become much more accessible and today anyone can have a digital mapping device in their pocket, literally: The DJI Mini has 30 min of flight time and a 4k camera that fits into your pocket. Just 5 years ago this would have been impossible. Drone imagery offers some very interesting and compelling opportunities for Geologists both in research and in teaching. Thanks to Moore's law, not only can we now acquire large and complex drone datasets, but we also have the computing capabilities to process the imagery to produce high-quality and accurate 2D/3D reconstructions with ever-increasing resolution. Where a few years ago it would take days to reconstruct a model, it now takes only hours. Software developers with a focus on Geology have since emerged and are developing the tools for geologists to ingest and process these datasets into valuable digital resources (i.e. VRGS).

A Geologist can now go into the field while taking a lunch break in the mountains launch a drone and collect hundreds to thousands of images with the click of a button, bring the data home, process the images into high-resolution 2D/3D models, use software packages for quantitative and qualitative data analysis, project the outcrops at real-world scale into their VR headsets to revisit the outcrops remotely, share the virtual outcrops with colleagues and students, compile virtual walkthroughs, etc. The possibilities are stunning.

The challenging aspect of all the above is knowing what to do with the data (use cases), how to turn raw data into processed models, maps, and datasets (methods), and finally knowing the limits of the obtained data (limitations). Although it is slowly changing, the reality is that many Geologists and Geology students are unaware of the positive implications and use cases many of these technologies can have for them. It is therefore essential to have efforts like this MSc thesis and the broader research and teaching community to continue to promote the exploration of these technologies in Geology.

A number of optimizations can be made to the approach discussed in this thesis:

1. First of all, knowing what drone imagery can and can't do will save a lot of time. If the goal is to map small-scale structures, mapping over a large area or flying at high altitudes is not viable, and instead flying over a small area and capturing data in detail is preferred (i.e. Roses outcrop). One will be surprised by the effectiveness of drones even when mapping a small area.
2. There are currently drones with built-in RTK that will save hours that are normally required to collect ground control points over rough terrain to georeferenced models.
3. The GNSS receivers of Modern UAs are generally good enough that they do not require RTK/PPK when doing quantitative analysis of large structures.
4. Have enough analog data anchor points. Developing a good mapping workflow takes time, effort, and skill and will not be good right at the start so having in-field data to compare with is invaluable.

The future for Geologists is and will increasingly be a blend between analog and digital. The single most important point to take away is that the true power of all these technologies lies in the way they can be combined. A 3D model is just a dataset, without software packages and a skilled student or researcher to analyze them their usefulness is limited. As such, I envision the big challenge in the years to come will be to:

1. Keeping up with technological developments.
2. Document all the potential applications and limitations of these technologies.
3. Building out workflows and pipelines to go from raw data to useful datasets.
4. Appropriate training of researchers and students to work with these technologies and apply them to their respective fields.
5. Build collaborative tools and web environments where data can be easily shared and used by peers.
6. Build Digital learning and support environments for teaching purposes where students can put their acquired knowledge to the test in preparation for fieldwork and assist them during fieldwork (i.e. Feedbackappapp by Dr. João Trabucho; GeoTour3D by VRGS).

Most value will come from (i) building digital web-based environments where students and researchers can add, share, edit, and visualize new datasets (a crowdsourced map if you will). Most data in Geology

to this day is siloed which is a great waste of intellectual effort. (ii) Digital learning environments built by educators and tailored to taking advantage of high-quality datasets while offering an immersive learning experience through virtual guides, quizzes, exercises, and even analysis of analog rock samples, etc. It enables students to get to know their fieldwork area, prepare for physical fieldwork, and assist them throughout their fieldwork. Linking digital with physical and finding the right balance is the future challenge of teaching in Geology.

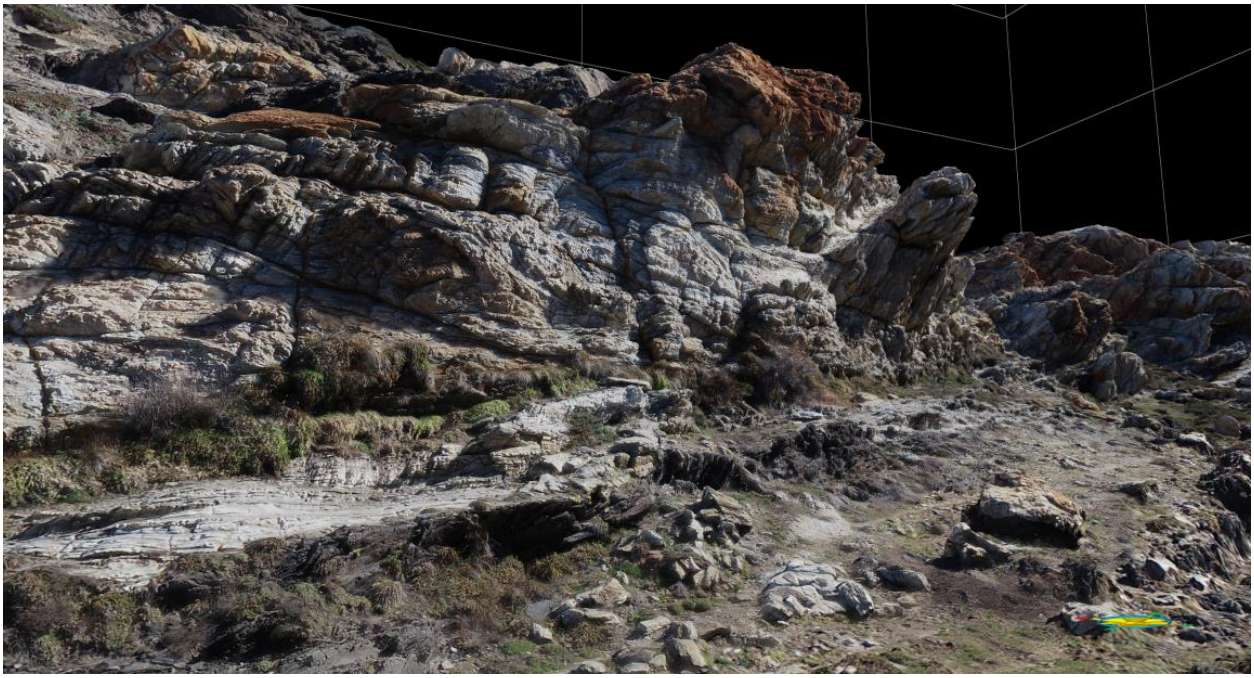

Figure 9.1 If the sky in this picture was blue, would you have guessed that this was a 3D model? Cala d'Agulles shear zone, Cap de Creus.

Bibliography

Agüera-Vega F., Carvajal-Ramírez F., Martínez-Carricondo P., López J.S., Mesas-Carrascosa F.J., García-Ferrer A., Pérez-Porras F.J., 2018. Reconstruction of extreme topography from UAV structure from motion photogrammetry. Measurement 121, 127-138.

Alvarado J.D., Fernández C., Castro A., Moreno-Ventas I., 2013. SHRIMP U–Pb zircon geochronology and thermal modeling of multilayer granitoid intrusions: Implications for the building and thermal evolution of the Central System batholith, Iberian Massif, Spain. Lithos 175, 104-123.

Bay H., Tuytelaars T., Van Gool L., 2006. Surf: Speeded Up Robust Features. In: Anonymous European Conference on Computer Vision (Springer), 404-417.

Bons P.D., Druguet E., Hamann I., Carreras J., Passchier C.W., 2004. Apparent boudinage in dykes. Journal of Structural Geology 26, 625-636.

Carcia Celma M.D., 1983. C-axis and shape fabrics in quartz mylonites of Cap de Creus (Spain); their properties and development. Ph.D. thesis .

Carreras J., 2001. Zooming on Northern Cap de Creus shear zones. Journal of Structural Geology 23, 1457-1486.

Carreras J., 1997. Shear Zones in Foliated Rocks: Geometry and Kinematics. In: Anonymous Evolution of Geological Structures in Micro-to Macro-Scales. Springer, 185-201.

Carreras J., Casas J.M., 1987. On folding and shear zone-development: a mesoscale structural study on the transition between two different tectonic styles. Tectonophysics 135, 87-98.

Carreras J., Druguet E., 1994. Structural zonation as a result of inhomogeneous non-coaxial deformation and its control on syntectonic intrusions: an example from the Cap de Creus area, eastern-Pyrenees. Journal of Structural Geology 16, 1525-1534.

Carreras J., Cosgrove J.W., Druguet E., 2013. Strain partitioning in banded and/or anisotropic rocks: Implications for inferring tectonic regimes. Journal of Structural Geology 50, 7-21.

Carreras J., Druguet E., 2014. Framing the tectonic regime of the NE Iberian Variscan segment. Geological Society, London, Special Publications 405, 249-264.

Carreras J., Druguet E., Griera A., Soldevila J., 2004. Strain and deformation history in a syntectonic pluton. The case of the Roses granodiorite (Cap de Creus, Eastern Pyrenees). Geological Society, London, Special Publications 224, 307-319.

Carreras J., Losantos M., 1982. Geological setting of the Roses granodiorite (E-Pyrenees, Spain). Acta geológica hispánica 17, 211-217.

Casas J.M., Álvaro J.J., Clausen S., Padel M., Puddu C., Sanz-López J., Sánchez-García T., Navidad M., Castiñeiras P., Liesa M., 2019. Palaeozoic Basement of the Pyrenees. In: Anonymous The Geology of Iberia: A Geodynamic Approach. Springer, 229-259.

Castiñeiras P., Navidad M., Liesa M., Carreras J., Casas J.M., 2008. U–Pb zircon ages (SHRIMP) for Cadomian and Early Ordovician magmatism in the Eastern Pyrenees: new insights into the pre-Variscan evolution of the northern Gondwana margin. Tectonophysics 461, 228-239.

Catalán J.R.M., Pascual F.J.R., Montes A.D., Fernández R.D., Barreiro J.G., Da Silva ÍD., Clavijo E.G., Ayarza P., Alcock J.E., 2014. The late Variscan HT/LP metamorphic event in NW and Central Iberia: relationships to crustal thickening, extension, orocline development and crustal evolution. Geological Society, London, Special Publications 405, 225-247.

Celma A.G., 1982. Domainal and fabric heterogeneities in the Cap de Creus quartz mylonites. Journal of Structural Geology 4, 443-455.

Černý P., Ercit T.S., 2005. The classification of granitic pegmatites revisited. The Canadian Mineralogist 43, 2005-2026.

Choukroune P., Roure F., Pinet B., Team E.P., 1990. Main results of the ECORS Pyrenees profile. Tectonophysics 173, 411-423.

Clark P.J., Evans F.C., 1954. Distance to nearest neighbor as a measure of spatial relationships in populations. Ecology 35, 445-453.

Corbella M., Melgarejo J.C., 1993. Rare-Element Pegmatites of the Cap De Creus Peninsula, Northeast Spain: A New Field of the Beryl–phosphate Subtype. In: Anonymous Proc. 8th IAGOD Symp. Schweizerbart'sche Verlagsbuchhandlung, Stuttgart, Germany (295-302).

Corsini M., Vauchez A., Caby R., 1996. Ductile duplexing at a bend of a continental-scale strike-slip shear zone: example from NE Brazil. Journal of Structural Geology 18, 385-394.

de Creus C., 2013. Measuring the effects of rheology and regional tectonics on the syntectonic rocks of a migmatitic complex from Cap de Creus. Geogaceta 54, 91-94.

De Reu J., De Smedt P., Herremans D., Van Meirvenne M., Laloo P., De Clercq W., 2014. On introducing an image-based 3D reconstruction method in archaeological excavation practice. Journal of Archaeological Science 41, 251-262.

Deveaud S., Gumiaux C., Gloaguen E., Branquet Y., 2013. Spatial statistical analysis applied to rare-element LCT-type pegmatite fields: an original approach to constrain faults-pegmatites-granites relationships.

Druguet Tantiña E., Carreras J., 2008. The Structure of the NE Cap De Creus Peninsula Relationships with Metamorphism and Magmatism. Universitat Autònoma de Barcelona,.

Druguet E., 2001. Development of high thermal gradients by coeval transpression and magmatism during the Variscan orogeny: insights from the Cap de Creus (Eastern Pyrenees). Tectonophysics 332, 275-293.

Druguet E., Hutton D., 1998. Syntectonic anatexis and magmatism in a mid-crustal transpressional shear zone: an example from the Hercynian rocks of the eastern Pyrenees. Journal of Structural Geology 20, 905-916.

Druguet E., Passchier C.W., Carreras J., Victor P., Den Brok S., 1997. Analysis of a complex high-strain zone at Cap de Creus, Spain. Tectonophysics 280, 31-45.

Druguet E., Alsop G.I., Carreras J., 2009. Coeval brittle and ductile structures associated with extreme deformation partitioning in a multilayer sequence. Journal of Structural Geology 31, 498-511.

Druguet E., Carreras J., 2006. Analogue modelling of syntectonic leucosomes in migmatitic schists. Journal of Structural Geology 28, 1734-1747.

Druguet E., Castro A., Chichorro M., Pereira M.F., Fernandez C., 2014. Zircon geochronology of intrusive rocks from Cap de Creus, Eastern Pyrenees. Geological Magazine 151, 1095-1114.

Eisenbeiß H., 2009. UAV photogrammetry. , Inst. für Geodäsie und Photogrammetrie.

Esteban J.J., Cuevas J., Tubía J.M., Sergeev S., Larionov A., 2011. A revised Aquitanian age for the emplacement of the Ronda peridotites (Betic Cordilleras, southern Spain). Geological Magazine 148, 183-187.

Fernández-Suárez J., Arenas R., Abati J., Catalán J.M., Whitehouse M.J., Jeffries T.E., 2007. U-Pb chronometry of polymetamorphic high-pressure granulites: An example from the allochthonous terranes of the NW Iberian Variscan belt. MEMOIRS-GEOLOGICAL SOCIETY OF AMERICA 200, 469.

Fischler M.A., Bolles R.C., 1987. Random Sample Consensus: A Paradigm for Model Fitting with Applications to Image Analysis and Automated Cartography. In: Anonymous Readings in Computer Vision. Elsevier, 726-740.

Fonseca H.A., Canals i Sabaté À, Cires J., Casas Tuset J.M., 2015. The Roses giant quartz vein (Cap de Creus, Eastern Pyrenees): Geology and fluid inclusion data. MACLA.Revista de la Sociedad Española de Mineralogía, 2015, vol.20, p.49-50 .

Galland O., Bertelsen H.S., Guldstrand F., Girod L., Johannessen R.F., Bjugger F., Burchardt S., Mair K., 2016. Application of open-source photogrammetric software MicMac for monitoring surface deformation in laboratory models. Journal of Geophysical Research: Solid Earth 121, 2852-2872.

Gardner R.L., Piazolo S., Daczko N.R., 2015. Pinch and swell structures: evidence for strain localisation by brittle-viscous behaviour in the middle crust.

Gleizes G., Leblanc D., Bouchez J.L., 1997. Variscan granites of the Pyrenees revisited: their role as syntectonic markers of the orogen. Terra Nova 9, 38-41.

Gleizes G., Leblanc D., Santana V., Olivier P., Bouchez J.L., 1998. Sigmoidal structures featuring dextral shear during emplacement of the Hercynian granite complex of Cauteretsâ€“Panticosa (Pyrenees). Journal of Structural Geology 20, 1229-1245.

Gwinner K., Jaumann R., Hauber E., Hoffmann H., Heipke C., Oberst J., Neukum G., Ansan V., Bostelmann J., Dumke A., 2016. The High Resolution Stereo Camera (HRSC) of Mars Express and its approach to science analysis and mapping for Mars and its satellites. Planetary and Space Science 126, 93-138.

Haruyama S., 2012. Advances in Visible Light Communication Technologies. In: Anonymous European Conference and Exhibition on Optical Communication (Optical Society of America), We. 3. B. 5.

Helmke M.F., Coughlin M.F., Potter N., Sevon W.D., 2007. Hickory Run Boulder Field (2): Collecting High-Resolution, Low-Altitude Aerial Photographs by UAV. In: Anonymous Geological Society of America Abstracts with Programs, 39, 43.

Hippertt J., 1999. Are Sâ€“C structures, duplexes and conjugate shear zones different manifestations of the same scale-invariant phenomenon? Journal of Structural Geology 21, 975-984.

Hudleston P.J., Treagus S.H., Lan L., 1996. Flexural flow folding: Does it occur in nature? Geology 24, 203-206.

Ibarguchi G., 1999. Deformation, highâ€pressure metamorphism and exhumation of ultramafic rocks in a deep subduction/collision setting (Cabo Ortegal, NW Spain). Journal of Metamorphic Geology 17, 747-764.

Javernick L., Brasington J., Caruso B., 2014. Modeling the topography of shallow braided rivers using Structure-from-Motion photogrammetry. Geomorphology 213, 166-182.

Jordan B.R., 2015. A bird's-eye view of geology: The use of micro drones/UAVs in geologic fieldwork and education. GSA Today 25, 50-52.

Karabinos P., Warren C., 2010. Visualizing strain and the Rf–Φ method with an interactive computer program. Journal of Structural Geology 32, 86-92.

Koenderink J.J., Van Doorn A.J., 1991. Affine structure from motion. JOSA A 8, 377-385.

Lejot J., Delacourt C., Piégay H., Fournier T., Trémélo M., Allemand P., 2007. Very high spatial resolution imagery for channel bathymetry and topography from an unmanned mapping controlled platform. Earth Surface Processes and Landforms: The Journal of the British Geomorphological Research Group 32, 1705-1725.

Lisle R.J., 1985. Geological Strain Analysis: A Manual for the Rf/0 Technique. Pergamon Press.

London D., Evensen J.M., 2002. Beryllium in silicic magmas and the origin of beryl-bearing pegmatites. Reviews in Mineralogy and Geochemistry 50, 445-486.

Lowe D.G., 2004. Distinctive image features from scale-invariant keypoints. International journal of computer vision 60, 91-110.

Lowe D.G., 1999. Object Recognition from Local Scale-Invariant Features. In: Anonymous Computer Vision, 1999. the Proceedings of the Seventh IEEE International Conference On, 2 (Ieee), 1150-1157.

Mallison H., Wings O., 2014. Photogrammetry in paleontology–a practical guide. Journal of Paleontological Techniques .

Mayer C., Pereira L.G., Kersten T.P., 2018. A Comprehensive Workflow to Process UAV Images for the Efficient Production of Accurate Geo-Information. In: Anonymous IX National Conference on Cartography and Geodesy.

Mikolajczyk K., Tuytelaars T., Schmid C., Zisserman A., Matas J., Schaffalitzky F., Kadir T., Van Gool L., 2005. A comparison of affine region detectors. International journal of computer vision 65, 43-72.

Muñoz J.A., Martinez A., Verges J., 1986. Thrust sequences in the eastern Spanish Pyrenees. Journal of Structural Geology 8, 399-405.

Muñoz J.A., 1992. Evolution of a Continental Collision Belt: ECORS-Pyrenees Crustal Balanced Cross-Section. In: Anonymous Thrust Tectonics. Springer, 235-246.

Munoz M., Courjault-Radé P., Tollon F., 1992. The massive stibnite veins of the French Palaeozoic basement: a metallogenic marker of Late Variscan brittle extension. Terra Nova 4, 171-177.

Myers J.S., 1978. Formation of banded gneisses by deformation of igneous rocks. Precambrian Research 6, 43-64.

Passchier C.W., Williams P.R., 1996. Conflicting shear sense indicators in shear zones; the problem of non-ideal sections. Journal of Structural Geology 18, 1281-1284.

Paterson S.R., Fowler Jr T.K., Schmidt K.L., Yoshinobu A.S., Yuan E.S., Miller R.B., 1998. Interpreting magmatic fabric patterns in plutons. Lithos 44, 53-82.

Paterson S.R., Pignotta G.S., Vernon R.H., 2004. The significance of microgranitoid enclave shapes and orientations. Journal of Structural Geology 26, 1465-1481.

Pereira M.F., Castro A., Chichorro M., Fernández C., Diaz-Alvarado J., Martí J., Rodríguez C., 2014. Chronological link between deep-seated processes in magma chambers and eruptions: Permo-Carboniferous magmatism in the core of Pangaea (Southern Pyrenees). Gondwana Research 25, 290-308.

Planells J.C., Druguet E., 2013. Illustrated Field Guide to the Geology of Cap De Creus. Universitat Autònoma de Barcelona, Servei de Publicacions.

Platt J.P., Vissers R., 1980. Extensional structures in anisotropic rocks. Journal of Structural Geology 2, 397-410.

Quesada C., Oliveira J.T., 2019. The Geology of Iberia: A Geodynamic Approach. Springer International Publishing, Switzerland.

Ramsay J.G., 1980. Shear zone geometry: a review. Journal of Structural Geology 2, 83-99.

Ramsay J.G., Graham R.H., 1970. Strain variation in shear belts. Canadian Journal of Earth Sciences 7, 786-813.

Reche J., MartÃnez F.J., Arboleya M.L., Dietsch C., Briggs W.D., 1998. Evolution of a kyanite-bearing belt within a HT-LP orogen: the case of NW Variscan Iberia. Journal of Metamorphic Geology 16, 379-394.

Ribeiro M.L., Reche J., López-Carmona A., Aguilar C., Bento dos Santos T., Chichorro M., Dias da Silva Í, Díez-Montes A., González-Clavijo E., Gutiérrez-Alonso G., 2019. Variscan metamorphism. The Geology of Iberia: A Geodynamic Approach: Volume 2: The Variscan Cycle , 431-495.

Ripley B.D., 1977. Modelling spatial patterns. Journal of the Royal Statistical Society: Series B (Methodological) 39, 172-192.

Rosu A., Assenbaum M., De la Torre Y., Pierrot-Deseilligny M., 2015. Coastal digital surface model on low contrast images. The International Archives of Photogrammetry, Remote Sensing and Spatial Information Sciences 40, 307.

Roure F., Choukroune P., Berastegui X., Munoz J.A., Villien A., Matheron P., Bareyt M., Seguret M., Camara P., Deramond J., 1989. ECORS deep seismic data and balanced cross sections: Geometric constraints on the evolution of the Pyrenees. Tectonics 8, 41-50.

Simpson C., Sistach M.L., 1982. Inhomogeneous deformation in Roses granodiorite, NE Spain. Acta geológica hispánica 17, 219-226.

Simpson C., 1983. Displacement and strain patterns from naturally occurring shear zone terminations. Journal of Structural Geology 5, 497-506.

Simpson C., Schmid S.M., 1983. An evaluation of criteria to deduce the sense of movement in sheared rocks. Geological Society of America Bulletin 94, 1281-1288.

Skjernaa L., 1980. Rotation and deformation of randomly oriented planar and linear structures in progressive simple shear. Journal of Structural Geology 2, 101-109.

Snavely N., Seitz S.M., Szeliski R., 2008. Modeling the world from internet photo collections. International journal of computer vision 80, 189-210.

Snavely N., Seitz S.M., Szeliski R., 2006. Photo Tourism: Exploring Photo Collections in 3D. In: Anonymous ACM Transactions on Graphics (TOG), 25 (ACM), 835-846.

Stampfli G.M., Hochard C., Vérard C., Wilhem C., 2013. The formation of Pangea. Tectonophysics 593, 1-19.

Stout M.Z., Crawford M.L., Ghent E.D., 1986. Pressure-temperature and evolution of fluid compositions of Al2SiO5-bearing rocks, Mica Creek, B.C., in light of fluid inclusion data and mineral equilibria. Contributions to Mineralogy and Petrology 92, 236-247.

Van Lichtervelde M., Grand'Homme A., de Saint-Blanquat M., Olivier P., Gerdes A., Paquette J., Melgarejo J.C., Druguet E., Alfonso P., 2017. U-Pb geochronology on zircon and columbite-group minerals of the Cap de Creus pegmatites, NE Spain. Mineralogy and petrology 111, 1-21.

Vergés J., Fernàndez M., Martínez A., 2002. The Pyrenean orogen: pre-, syn-, and post-collisional evolution. Journal of the Virtual Explorer 8, 55-74.

Vissers R.L., Ganerød M., Pennock G.M., van Hinsbergen D.J., 2020. Eocene seismogenic reactivation of a Jurassic ductile shear zone at Cap de Creus, Pyrenees, NE Spain. Journal of Structural Geology 134, 103994.

Vissers R.L., Van Hinsbergen D.J., Wilkinson C.M., Ganerød M., 2017. Middle Jurassic shear zones at Cap de Creus (eastern Pyrenees, Spain): a record of pre-drift extension of the Piemonte–Ligurian Ocean? Journal of the Geological Society 174, 289-300.

Vissers R., Meijer P.T., 2012. Mesozoic rotation of Iberia: subduction in the Pyrenees? Earth-Science Reviews 110, 93-110.

Vitek J.D., Giardino J.R., Fitzgerald J.W., 1996. Mapping geomorphology: A journey from paper maps, through computer mapping to GIS and Virtual Reality. Geomorphology 16, 233-249.

Vollgger S.A., Cruden A.R., 2016. Mapping folds and fractures in basement and cover rocks using UAV photogrammetry, Cape Liptrap and Cape Paterson, Victoria, Australia. Journal of Structural Geology 85, 168-187.

Wheeler J., 1986. Strain analysis in rocks with pretectonic fabrics. Journal of Structural Geology 8, 887-896.

White S.H., Burrows S.E., Carreras J., Shaw N.D., Humphreys F.J., 1980. On mylonites in ductile shear zones. Journal of Structural Geology 2, 175-187.

Yilmaz H.M., Yakar M., Yildiz F., 2008. Documentation of historical caravansaries by digital close range photogrammetry. Automation in Construction 17, 489-498.

Zwart H.J., 1986. The variscan geology of the Pyrenees. Tectonophysics 129, 9-27.